Title
A STUDY OF ELECTRON CURRENT INTENSITIES EMITTED FROM THE SUPERLATTICE PLANES OF AN ORDERED ALLOY

Author
Lira-Olivares, Joaquin.

Publication Date
1974-05-01

LBL-2265
c.1

A STUDY OF ELECTRON CURRENT INTENSITIES EMITTED FROM THE SUPERLATTICE PLANES OF AN ORDERED ALLOY

Joaquin Lira-Olivares
(Ph. D. thesis)

May, 1974

Prepared for the U. S. Atomic Energy Commission
under Contract W-7405-ENG-48

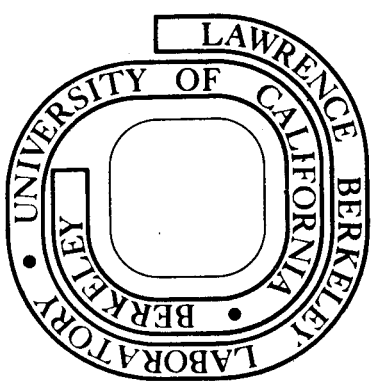

LBL-2265
c.1

DISCLAIMER

To

Maria, Sara
Pedro, Juan and
Joaquin

whose patience and love
made this thesis possible

TABLE OF CONTENTS

A STUDY OF ELECTRON CURRENT INTENSITIES EMITTED FROM THE SUPERLATTICE PLANES OF AN ORDERED ALLOY

Joaquin Lira-Olivares

Inorganic Materials Research Division, Lawrence Berkeley Laboratory and Department of Materials Science and Engineering, College of Engineering; University of California, Berkeley, California

ABSTRACT

The electron emission from cold, Ni_4W specimens was studied using a field ion-field emission microscope and a Jarrell-Ash recording microphotometer.

Small current variations were observed on azimuthal intensity measurements on the α phase. These were interpreted as produced by different densities of solute (W) at the surface of the emitter. The electron current emitted from the layered superlattice planes of the β phase, showed cyclical changes in intensity produced by the removal of atomic monolayers using field evaporation. Such a variation was interpreted by comparing the field evaporation process of the layered superlattice planes with the adsorption of epitaxial layers on a metal substrate. The Topping dipolar model was applied for numerical interpretation of the data and was found inconsistent with the experimental results.

A simple model was suggested for the interpretation of the current variation observed. The model might have applicability to the understanding of some adsorption phenomena.

The observation of the elusive γ phase of Ni_4W using field ion-field emission microscopy is also reported in this work, as well as

a variation of the standard field ion microscopy method for the observation of surface defects.

I. INTRODUCTION

Most investigators agree that monolayers of metallic adsorbates change the energy per unit charge required to remove an electron from a metal surface (work function). The changes in work function so produced have been interpreted by considering the adsorbate layer as a dipolar monolayer which produces a change $\Delta\phi$ in the work function proportional to the dipolar moment and the density of dipoles.

Duke and Alferieff[1] have proposed that some of the electron current changes produced by adsorption may be due to a resonance effect in the emission probability with enhancements of 10^2 to 10^4 in the emission current.

Two questions arise from the foregoing discussion.

1. Is the change of electron emission current produced by an adsorbed monolayer of metal atoms a consequence of a work function change or is it a resonance effect, or both?
2. If there is a work function change, could it be produced by the interaction between dipoles?

The first of these questions has been partially answered by Clark[2] in his experiments with adsorption of single strontium atoms on a W surface. He found that the measured current changes were produced by resonance, as predicted by Alferieff, and not by a work function change. However, this question has not been answered for adsorbed monolayers.

The second question has not been answered at all. The basic problem in investigating this question experimentally is the difficulty of adsorbing a true atomic monolayer.

The purpose of this thesis is to ascertain whether changes of only dipolar moments at the surface would produce changes in the electron emission current. Toward this end, the classical method of evaporating atoms on a substrate was attempted and considered unsuccessful. Hence, a novel method, using the layered structure of an ordered alloy (Ni_4W), was utilized.

The techniques employed in these experiments were those of (1) field ionization, to ascertain the crystallographic characteristics of the specimens; (2) field emission microscopy, to obtain the electron currents from the emitting surface; and (3) a scintillation-photometric technique, to measure the current changes. The layers of different chemical composition (Ni and W) were brought to the surface by field evaporation.

The following chapters give a brief resume of the theory involved and a review of the pertinent literature, followed by the main body of the thesis in which the experimental techniques are considered and the results are presented and discussed.

Finally, a summary of the major results is included with some conclusions and recommendations for future research. Besides the major topic of the thesis, some additional results are briefly reported and discussed in Chapter X and some technical matters are included in the Appendix.

II. THEORY

A. The Work Function of Metals

Classically the energy of the electrons in a metal can best be represented by the Fermi-Dirac distribution for an ideal electron gas at thermal equilibrium.

$$f(\varepsilon_i) = \frac{1}{1 + e^{(\varepsilon_i - \bar{\mu})/kT}} \qquad \text{(IIA.1)}$$

where ε_i represents an energy state, taking zero energy as the state occupied by an electron at rest at infinite separation from the metal. Also, k is the Boltzmann constant and T the temperature in K. Taking the local mean electrostatic potential energy of an electron as the zero reference for ε_i, the electrochemical potential $\bar{\mu}$ can be replaced by the chemical potential μ.

The two potentials, μ and $\bar{\mu}$ are related by the equation

$$\bar{\mu} = \mu - eU_{inner} \qquad \text{(IIA.2)}$$

where U_{inner} is the electrical potential of the metal (inner potential) and e is the electron charge 1.602×10^{-19} coulombs. The inner potential is affected by fields outside the conductor. These fields can be produced, for example, by adsorbed atoms or molecules that form surface dipoles. Thus, it can be said that μ is a bulk property while $\bar{\mu}$ is a function of both the bulk and external donditions, even though the two quantities refer to the same energy level and only differ on the zero reference points. The energy level μ (or $\bar{\mu}$) has

a probability of occupancy $f(\varepsilon_i)$ equal to 1/2 (from Eq. IIA.1).

The energy $\bar{\mu}$ can be used to describe the process by which a metal loses or gains an electron. This is possible because $\bar{\mu}$ is actually the change of free energy of a metal due to the incorporation or solution of electrons as described by the relation

$$\bar{\mu} = \left(\frac{\partial F}{\partial n}\right)_{T,V} \qquad \text{(IIA.3)}$$

where F is the Helmholts free energy and n is the number of dissolved electrons. The work function ϕ is the energy per unit charge required to remove an electron from a metal and to place it at a distance x_m from that metal. The distance x_m, theoretically described as infinity, has been considered as short as 10^{-4} cm (Gundry and Tompkins,[3]) whem the classical image potential is taken into account ($-e^2/4x$ for metals). However, in field emission experiments the external field of ~ .3 eV/cm distorts the surface potential so that the electron-surface interaction is negligible at much shorter x_m.

The above definition of the work function ϕ can be expressed by the simple relationship

$$\phi = -U_{outer} - \frac{\bar{\mu}}{e} \qquad \text{(IIA.4)}$$

where U_{outer} is the energy of the electron at x_m.

From Eqs. (IIA.2 and IIA.4).

$$\phi = - U_{out} - (\frac{\mu}{e} - U_{in}) \qquad \text{(IIA.5)}$$

Rearranging

$$\phi = - (U_{out} - U_{in}) - \frac{\mu}{e} \qquad \text{(IIA.6)}$$

$$\phi = - \chi - \frac{\mu}{e} \ , \qquad \text{(IIA.7)}$$

where χ is the potential difference between the inside and outside of the conductor. The work function can then be represented by the negative sum of the chemical potential (a function of the bulk) and the surface potential χ which depends on the arrangement of surface atoms as well as the internal structure of the metal.

$$\phi = - (\chi + \frac{\mu}{e}) \qquad \text{(IIA.8)}$$

Thus adhesion of atoms on the surface will affect the χ portion of ϕ.

At 0 K, the work function ϕ is the energy difference between the Fermi energy and the vacuum level of energies, as the Fermi level is, by definition, the highest energy level filled at 0 K.

Smoluchowski[4] proposes a simple model to account for the surface contributions to the work function. He considers the electrons as forming a classical Fermi gas at the bulk and the surface composed of a layer of stripped positively charged ions whose conduction electrons form an evanescent vapor extending out past the layer of ions. The spreading of electrons forms a net negative charge in the outer surface

creating an outwardly phasing field or a dipolar layer on the surface.

If the atoms (or ions) can be considered separated at the surface, the electrons of the protruding atoms will tend to fill the interatomic-surface spaces, tending to smooth the surface and creating an inwardly oriented electric field. Then, the "spill over" effect and the "smoothing" effect will oppose each other.

The "spill over" effect acts as a repelling negative charge for an outgoing electron, increasing the energy necessary to take out an electron from the surface; and the "smoothing" effect tends to help electrons escape. Thus, a rough surface will allow more electrons (of equal initial energy) to escape than a closely packed surface. This has been shown experimentally: closely packed (low index) crystallographic planes have higher work function than loosely packed (high index) crystallographic planes. The lower the Miller index, the higher the work function.[5] There are some exceptions to this rule, but they will not be discussed here.[6]

Smoluchowski calculated the surface potentials for some of the crystallographic faces of tungsten and showed that the "spill over" effect is almost independent of orientation, while the smoothing effect is strongly dependent on orientation as could be expected.

B. Work Function Changes Due to Adsorption

The work function is dependent on the difference in potential between the interior of the metal sample and the potential just outside the metal surface.

As the free atom approaches the metal surface, there is a perturbation of the discrete energies of the outer electrons. In the subsequent adsorption process, there are three distinguishable cases of electronic interactions:

1. Physical Adsorption

An atom is considered physically absorbed when there is no exchange of electrons between the adatom and the metal substrate (for example a noble gas atom), but a slight polarization of the adatom might occur. In this case, no change in the work function of the substrate is expected.

2. Weak Chemisorption.

Exchange forces may cause a weak chemisorptive bond of the covalent type between the adsorbed atom and the substrate (for example H_2 on Ni). There is a definite change of work function in this case.

3. Strong Chemisorption

There is a transfer of an electron from the adatom to the metal surface or viceversa, depending on whether the work function of the metal is larger or smaller in comparison with the ionization energy of the adsorbed atom. If the adatoms have a lower (higher) ionization energy than the local work function of the metal, the adsorbed layer will be positively (negatively) charged.

The increase or decrease in ϕ with increasing coverage of the pure substrate by adsorbed atoms can then be attributed to formation of adatom-substrate dipoles in which the adatom is either negatively charged (increase of ϕ) or positively charged (decrease of ϕ) with respect to the substrate atoms' neighbors. This effect may be evaluated

in terms of the change in electrical potential caused by the redistribution of charge at the surface. Considering the uppermost layer as a sheet of uniformly charged particles, each with charge q such that the density of charged species is equal to n, a negative test charge q' experiences a force $|F| = 2\pi nqq'$ if the test charge can be considered to be homogeneous. The force is attractive if the sheet is positively charged, repulsive if the sheet is negatively charged. If we now consider two oppositely charged sheets--one formed by the surface charges and the other by their images--separated by a distance $2d_o$, with opposite but equal charge charge densities (qn), the test charge q' experiences a force only when it is near the two charged sheets. The repulsive and attractive interactions are additive between the plates; therefore the force experienced is $F'=4\pi nqq'$. As in a classical capacitor, moving the test charge from one plate to the other changes the energy by $\Delta E=8\pi nqq'd_o$. This means that between the two sheets and in general between all points on opposite sides of the charged sheets, there is a change in potential $\Delta V=\pm 8\pi nqd_o$. If we consider the arrangement of two planes to be a single dipolar plane which contains n dipoles per square centimeter with axes perpendicular to the plane each with a moment $\mu_o=2qd_o$, then the change in potential is $\Delta V=\pm 4\pi n\mu_o$. Therefore, if a dipolar layer is adsorbed parallel to the surface of a metal the change of work function $\Delta\phi$ which is produced by surface dipoles of dipole moment μ is given by

$$\Delta\phi = 2\pi\mu n \qquad \text{(IIB.1)}$$

where n is the density of surface dipoles.

4. Depolarization Effect

The dipoles formed by adatoms at the surface of a metal can be expected to interact with each other, and their dipole moment μ is itself a function of the dipole density.

Consider again that the adatoms have been either polarized or ionized on the surface and that each adatom has a net charge q and produces an image charge -q at a distance $2d_o$ from it. That is, the effective metal surface is at a distance d_o from the adsorbed charge, and the dipole moment is given by $\mu_o = 2d_o q$ for each dipole.

The dielectric constant of the metal is not infinite; thus, the adsorbate charge produces a volume distribution of charge. However, based on the Fermi-Thomas[7] model, the screening effect for a metal does not allow field penetration to more than ~ 0.5Å, while the distance between adsorbate and surface atoms is ~ 2Å.

The potential resulting from the dipole layer, however, can be expected to have a final value at larger distances than d_o. Schmidt and Gomer[8] expressed the field produced by the dipole layer at d_o as

$$F = \frac{f(n)\mu}{d_o^3} \qquad \text{(IIB.2)}$$

The net dipole moment μ is related to $\mu_o = 2qd_o$ by

$$\mu = \mu_o - \alpha F = \mu_o - \frac{\alpha f(n)\mu}{d_o^3} \qquad \text{(IIB.3)}$$

where α is the polarizability of the adatom-surface complex. The dipole moment is

$$\mu = \frac{\mu_o}{1 + \alpha \frac{f(n)}{d_o^3}} \qquad \text{(IIB.4)}$$

The work function change produced by the dipole layer is given by

$$\Delta\phi = \phi - \phi_o = \frac{2\pi \mu_o n}{[1 + \alpha \frac{f(n)}{d_o^3}]} \qquad \text{(IIB.5)}$$

Assuming the adsorbate layer to be formed by point dipoles with axis perpendicular to the substrate's surface, then the depolarization term f(n) can be derived from Topping's approximation for the mutual potential energy per unit area.[9] Topping used a hexagonal and a square array of point dipoles in his model. Both arrays gave a constant ~ 9 to a first approximation for the potential energy expression:

$$f(n) = 9 d_o^3 n^{3/2} \quad . \qquad \text{(IIB.6)}$$

hence

$$\Delta\phi = \frac{2\pi \mu_o n}{[1 + 9\alpha n^{3/2}]} \qquad \text{(IIB.7)}$$

Experimentally it has been observed by Jones[10] that ϕ at θ_{max}

$$\frac{\partial\phi}{\partial n} = \frac{\partial(\Delta\phi)}{\partial n} = 0 \qquad \text{(IIB.8)}$$

Differentiating Eq. (IIB.7) and applying this criterion, α can obtained

$$\alpha = 0.221\, n_{max}^{-3/2} \tag{IIB.9}$$

where n_{max} is the measured adatom density at $\phi = \phi_{max}$. Knowing n_{max} experimentally α can be calculated and then, having ascertained $\Delta\phi$, μ_o can be attained from Eq. (IIB.7). For comparison with experimental data Schmidt and Gomer[11] have modified the equation above to

$$\frac{\theta}{\Delta\phi} = \left(\frac{1}{C_1}\right) + \left(\frac{C_2}{C_1}\right)\theta^{3/2} \tag{IIB.10}$$

where

$$C_1 = \left(\frac{d\Delta\phi}{d\theta}\right)_{\theta=0} = 4\pi M_o n_\phi \tag{IIB.11}$$

$C_2 = 9\alpha n_o^{3/2}$, $\theta = n/n_o$, and $n_o = 3.9\times10^{14}$ atoms/cm^2. The validity of the Topping model is then easily determined by plotting $\theta/\Delta\phi$ against $\theta^{3/2}$. The linear behavior of this characteristic determines whether the model is applicable or not. Schmidt and Gomer[8] applied the model to potassium adsorption on several tungsten surfaces.

Kaplit, Schrenk, and Zelby[12] have discussed some of the models for electron emission from metals with adsorbed monolayers, and have stressed the importance of progressing beyond models portraying the adsorbate as a neutral or ionic species to the consideration of partially ionic and partially covalent bonding.

The application of Gomer's model for work function change to the systems studied is difficult because there are several factors which are unknown experimentally. The primary difficulties lie in determination of the density of adsorbed species and the separation of the metal surface and the adsorbed layer. Another difficulty is determining whether there is one layer of atoms or three dimensional arrays of atoms. This is specially crucial at the early stages of deposition of adatoms on the substrate in close-packed planes, for there is a tendency for the adatoms to pack around the previously adsorbed atoms, forming a 3-D array that strongly disturbs the electric field and thus electron emission.

It is apparent that in order to apply the preceding model, there must be a way to insure the existence of a two-dimensional array of dipoles on the surface of the substrate, but this has not actually been achieved using evaporation techniques or deposition. (See Chap. XIII)

In Chapter VII we shall propose an alternate method for ascertaining work function changes due to differences of charge concentrations on the surface. This alternate method provides a better control of dipole densities, surface irregularities and position of the dipolar layer.

C. The Fowler-Nordheim Equation

The present discussion follows closely the presentation made by H. W. Gowdy[7] of the F-N equation. The model formulated by R. H. Fowler and L. W. Nordheim[13] is the one used in most cases to interpret low temperature emission experiments.

Fowler and Nordheim used the Sommerfeld free-electron theory as their model to describe the electrons in the metal. These electrons are thus taken to be an ideal electron gas in thermal equilibrium as stated in Chap. II Sec. A. Thus the energy states obey the Fermi-Dirac distribution function.

$$f(\varepsilon_i) = \frac{1}{e^{(\varepsilon_i-\bar{\mu})/kT} + 1} \qquad \text{(IIC.1)}$$

where $f(\varepsilon_i)$ is the probability that a state at energy ε_i will be occupied, T is the temperature, k is Boltzmann's constant and $\bar{\mu}$ is the electrochemical potentail. For free electron Fermi gases, μ is essentially equal to the Fermi energy ε_F for low temperatures, i.e. for $kT/\varepsilon_F \leq 0.5$. In common metals $kT/\varepsilon_F \approx 0.01$ at room temperature.[14] Thus, since these results are strictly applicable only at 0°K, this substitution is legitimate.

It follows then that

$$n_i = \frac{g_i}{e^{(\varepsilon_i-\bar{\mu})/kT} + 1} \qquad \text{(IIC.2)}$$

In each volume h^3 in phase space there are two states for a free particle of spin 1/2. Thus the number of states in the momentum range $dp_x dp_y dp_z$ for a free electron solid of volume V is $2V/h^3 \; dp_x dp_y dp_z$. Therefore

$$dn = \frac{2V}{h^3} \frac{dp_x dp_y dp_z}{e^{(\varepsilon-\bar{\mu})/kT} + 1} \qquad \text{(IIC.3)}$$

The field emission problem itself is considered to be one dimensional. There are three parts to the potential experienced by the electrons in this model.

1. Within the metal the potential energy has a constant value at $-W_a$, relative to zero potential energy when the metal and electron are separated by an infinite distance.

2. An electric field is applied to draw the electrons out of the metal. It is assumed that the free charges cause this field to be neutralized within the metal. Furthermore it is assumed that the external field is constant as far as the surface effects are concerned. The origin is at the metal surface. Taking the positive x axis to be perpendicular to the metal surface and to extend out from the surface, the contribution of the field to the total potential is given by -eEx. Here E is the constant electric field and e the charge of an electron. (See Fig. 1a).

3. An electron outside the metal is attracted to it by the image charge it induces in the metal. The potential energy due to the Coulomb attraction is given by $-e^2/4x$.

Inherent in these assumptions is the assumption that the surface is smooth and an infinite plane. However, this is not always an acceptable assumption in field emission as will be shown later.

The potential is thus given by

$$\begin{aligned} V(x) &= -W_a \quad \text{for} \quad x < 0 \\ &= -eEx - \frac{e^2}{4x} \quad \text{for} \quad x > 0 \end{aligned} \tag{IIC.4}$$

these potentials are shown approximately in Fig. 1a. The maximum value of the potential occurs at the point

$$x_o = \frac{1}{2}\sqrt{e/E} \tag{IIC.5}$$

and the value of the potential at x_o is

$$V_{max} = -\sqrt{e^3 E} \tag{IIC.6}$$

In computing the flux of electrons it is assumed that the flux is only a small perturbation on the electrons in the metal; and thus, the equilibrium distribution of electrons is not disturbed. Therefore the electron current is found by integrating over all possible electron energies, the equilibrium flux of electrons incident on the surface times the tunneling probability of the electrons. This integral can be conveniently written in terms of the x component W of the total energy ε defined by

$$\begin{aligned} W &= \varepsilon - \frac{p_y^2}{2m} - \frac{p_z^2}{2m} \\ &= \frac{p_x^2}{2m} + V(x) \end{aligned} \tag{IIC.7}$$

Then, if N(W)dW is the number of electrons incident on the surface per unit time per unit area whose x component of energy is within the range W to W+dW, and D(W) is the tunneling probability (or transmission coefficient) for the energy W, their product P(W)dW equals the electron flux per unit area for this energy range

$$P(W)dW = D(W)N(W)dW \tag{IIC.8}$$

and the total current density J is

$$J = e \cdot \int_{-W_a}^{\infty} P(W)dW \tag{IIC.9}$$

The number of electrons inside the metal per unit area per unit time moving in the x direction with x momentum between p_x and p_x+dp_x equals

$$\int_{p_y=-\infty}^{\infty} \int_{p_z=-\infty}^{\infty} \frac{p_x}{m} \frac{2}{h^3} \frac{dp_x dp_y dp_z}{e^{(\varepsilon-\bar{\mu})/kT} + 1} \tag{IIC.10}$$

According to Eq. (IIC.7),

$$p_x dp_x = mdW \tag{IIC.11}$$

Using this in Eq. (IIC.10) gives N(W)dW, the number of electrons with x energy between W and W+dW incident on the surface per unit area per unit time:

$$N(W)dW = \frac{2}{h^3} dW \int_{\infty}^{\infty} \int_{\infty}^{\infty} \frac{dp_y dp_z}{\exp\left(\frac{W-\bar{\mu}}{kT} + \frac{p_y^2+p_z^2}{2mkT}\right) + 1} \tag{IIC.12}$$

Using polar coordinates this equation can easily be integrated to obtain the value for the supply function N(W):

$$N(W) = \frac{4\pi mkT}{h^3} \ln[1 + e^{-(W-\bar{\mu})/kT}] \qquad \text{(IIC.13)}$$

The transmission coefficient D(W) is calculated using the WKB approximation

$$D(W) = \exp\left[-\int_{x_1}^{x_2} \sqrt{\frac{8m}{\hbar^2}\,[V(x)-W]}\; dx\right] \qquad \text{(IIC.14)}$$

where x_1 and x_2 are the locations of the walls of the potential barrier at energy W, chosen so that $x_1 < x_2$. This result is valid only when $W \ll V_{max}$ (which is the case in field emission at 0 K).[15] Inserting Eq. (IIC.4) into Eq. (IIC.14) and introducing the parameter

$$y = \frac{\sqrt{e^3 E}}{|W|} \qquad \text{(IIC.15)}$$

leads to the reduction of the integral to a standard form for an elliptic integral. The transmission coefficient is then given by

$$D(W) = e^{-\frac{4\sqrt{2m|W|^3}}{3\hbar eE}\, v(y)} \qquad \text{(IIC.16)}$$

where v(y) is a function of elliptic integrals and has been extensively tabulated.[16]

Inserting Eqs. (IIC.13) and (IIC.16) into Eq. (IIC.B) gives

$$P(W)dW = \frac{4\pi mkT}{h^3} e^{-\frac{4\sqrt{2m|W|^3}}{3\hbar eE} v(y)} \left(\ell n\ 1+e^{-\frac{(W-\bar{\mu})}{kT}} \right) dW \qquad \text{(IIC.17)}$$

At low enough temperatures the electrons penetrating the barrier have energies in the neighborhood of the Fermi level. Thus the exponent can be expanded in a power series about $W = \bar{\mu} = -\phi$. Using only the first two terms of the expansion gives

$$-\frac{4\sqrt{2m|W|^3}}{3\hbar eE} v(y) \approx -c + \frac{W-\bar{\mu}}{d} \qquad \text{(IIC.18)}$$

where

$$c = \frac{4\sqrt{2m\phi^3}}{3\hbar eE} v \frac{\sqrt{e^3E}}{\phi} \qquad \text{(IIC.19)}$$

$$d = \frac{\hbar eE}{2\sqrt{2m\phi} \cdot t(\sqrt{e^3E}/\phi)} \qquad \text{(IIC.20)}$$

and

$$t(y) = v(y) - \frac{2}{3} y \frac{dv(y)}{dy} \qquad \text{(IIC.21)}$$

For low enough temperatures

$$kT\ell n\ (1 + e^{-\frac{W-\bar{\mu}}{kT}}) = 0 \quad \text{when} \quad W > \bar{\mu}$$

$$= \bar{\mu}-W \quad \text{when} \quad W < \bar{\mu} \qquad \text{(IIC.22)}$$

Substituting Eqs. (IIC.18) and (IIC.27) into Eq. (IIC.17) gives

$$P(W) = 0 \quad \text{when} \quad W > \bar{\mu}$$

$$= \frac{4\pi m}{h^3} e^{-c+(W-\bar{\mu})/d} (\bar{\mu}-W) \quad \text{when} \quad W < \bar{\mu} \qquad \text{(IIC.23)}$$

Integrating P(W)dW over all energies then gives the total current density. The lower limit of integration is taken as $-\infty$ since $-W_a$ is normally far below $\bar{\mu}$, and $\bar{\mu}$ is used as the upper limit. The result is

$$J = \frac{e^3E^2}{8\pi h\phi t^2 \sqrt{\frac{e^3E}{\phi}}} e^{-\frac{4\sqrt{2m}\,\phi^{3/2}}{3\hbar eE} v \frac{\sqrt{e^3E}}{\phi}} \qquad \text{(IIC.24)}$$

Using recent values for m, e, and $\hbar$,[17] and expressing ϕ in electron volts and E in volts/cm, this becomes

$$j = \frac{1.541\times10^{-6}E^2}{\phi t^2(y)} \exp\left[-6.831\times10^7 \frac{\phi^{3/2}}{E} v(y)\right] \text{amp/cm}^2 \qquad \text{(IIC.25)}$$

where

$$y = 3.79\times10^{-4} \sqrt{E/\phi} \qquad \text{(IIC.26)}$$

It is seen that y is the ratio of the decrease in the potential maximum due to the image force to the work function. Many investigators have derived low temperature field emission equations for several different potentials. The influence of the discreteness of the surface atoms would be expected to increase for higher applied electric fields

since the width of the tunneling barrier decreases as this field increases. The image force model must also be modified whenever the surface is covered by adsorbed atoms. The validity of the F-N equation has been studied by several authors.

Calculations by Harrison on the influence of the density of states of the electrons predict that the band structure should have little effect[16] in total current measurements. Thus the Summerfeld model can be used. Itskovich has investigated the phenomenon of field emission for an arbitrary electron dispersion law using the image potential model for the tunneling barrier.[18]

According to his calculations, the pre-exponential part of the F-N equation is changed, but the exponential part is not. The electrons occupying the small region in $\bar{k}$ space where the energy E_x of motion along the x axis is near its maximum at T=0°K represent the principal contribution to field emission. This maximum thus represents the effective work function in the exponential of the field emission equation. Due to the conservation of the reduced tangential quasimomentum of the electrons during field emission, this maximum coincides with the work function only if the surface normal of the crystallographic plane being studied intersects the Fermi surface.

Otherwise, this effective work function is larger than the work function and the electrons that will be emitted are not necessarily at the Fermi level, but can be found much below it (even outside the conduction band in some cases), since E_x can reach its maximum independently of the total energy. Thus, in these cases, information

on the Fermi surface can be obtained from the difference between the effective and true work function.

According to Stratton's calculations,[19] total energy distribution (TED) measurements are reasonably insensitive to deviations from the Sommerfeld model except when the Fermi surface is small or a band gap occurs near the Fermi level. According to Swanson,[19] TED measurements have confirmed the validity of the Sommerfeld model for all the major crystal directions of tungsten and molybdenum except the important ⟨100⟩ direction.

Van Oostrom in his Ph.D. thesis, extensively reviewed the validity of the F-N equation and the various assumptions involved. For the case of clean tungsten, he found no band structure effects.[16]

The accuracy of representing a clean surface by the image potential model has also been extensively investigated.

Sachs and Dexter[20] treated the interaction of a charged macroscopic body with a metal surface, quantum mechanically, by means of the variation method. The result for the interaction energy is the image force plus three correction terms caused by the change in kinetic energy associated with the concentration of the electrons on the surface of the metal, the reduction in the electron-electron interaction energy in the metal resulting from the antisymmetrization of the wave function, and the effect of the finite thickness of the surface charge. It was found that the three correction terms are negligible except when the distances between the charged body and metal surface were small. In this case the surface structure effects became important.

Following Sachs and Dexter, Cutler and Gibbons[16] suggested a potential energy of the form

$$V(x) = -\frac{e^2}{4x}\left[1 - \frac{\eta}{x}\right] \qquad \text{(IIC.27)}$$

Here, η is the quantum correction that is supposed to depend on the electronic properties of the metal. Several values for η have been used. Recently, Dubey proposed a precise criterion for assigning a value to η.[21] For the value of η they used, Nagy and Cutler found that deviations from the linear F-N plot begin at about 0.5 V/Å.[22]

Recently, Gadzuk and Plummer[23] have performed total energy distribution measurements for field emission from tungsten emitters heated up to 1570°K using a Kuyatt-Simpson-type spherical deflection energy analyzer.[7] They found good agreement with the theoretical models mentioned in Section IIB. Their results seem to show that the classical image force model for the surface potential is valid for distances x_o approaching 3 to 4 Å, where x_o is the distance from the metal surface at which the potential maximum occurs. This is the order of electron-metal separation distances which Sachs and Dexter[16] suggested may result in the breakdown of the image potential due to quantum mechanical effects.

Van Oostrom[16] concluded that the F-N equation satisfactorily described his results for clean tungsten. He noted, though, that the corrected image force potential Eq. (IIC.27) gave better agreement

between the experimentally determined and theoretical values for the half-widths of the total energy distribution at low temperature.

The simple image-force law does not appear to be generally applicable to field emission through an adsorbed layer on the surface. For example, in the adsorption of nitrogen on tungsten, the total current decreases even though the work function calculated from the F-N plot decreases. A decrease in the emitting area does not appear to explain this.

Hansen and Gardner[24] have used Eq. (IIC.14) to evaluate D for electron energy equal to the Fermi energy for several external potentials (the image force potential was always neglected). The potentials used were:

1. The applied field.
2. Adsorption of dipole layer plus the applied field.
3. Adsorption of a dielectric layer plus the applied field.
4. Adsorption of a polarizable surface species plus the applied field.
5. Adsorption of a deeply attractive potential well plus the applied field.

For each of the first four cases, the field dependent part of D was (within the approximations used),

$$\exp\left(-\frac{2}{3}(8m/\hbar^2)^{1/2}\,\phi^{3/2}/eE\right) \qquad \text{(IIC.28)}$$

which is the field dependent exponential of the F-N equation neglecting the image force term. The pre-exponential term was different in each case.

For the fifth case, a different dependence on ϕ and E was found, and consequently an F-N plot would show appreciable curvature at high electric fields.

The case of a polarizable adsorbed species is particularly important since the actual work function with the field applied is different from the zero field value, and the latter is the one usually desired. It appears that the zero field value is obtained unless the electric field is too high.[16]

The above results show that the slope of the F-N plot is not very sensitive to the shape of the potential barrier outside the metal surface. This is fortuitous since it means that work function changes can be determined from F-N plot slope changes for a broader range of potentials than those for which the F-N equation itself is valid.

Duke and Alferieff have formulated a one-dimensional pseudo-potential model in which the adsorbed atom is treated as an additional potential outside the metal surface.[1] The results are only qualitative, but show that adsorption can lead to other interesting effects. One experimental case interpreted is the above-mentioned simultaneous reduction in the work function and emission current by the adsorption of nitrogen on the (100) and (411) faces of tungsten. Other experiments using this model will be discussed in Chap. IV.

Gadzuk[25] has extended the work of Duke and Alferieff to treat possible resonance transmission effects over adsorbed atoms in thermionic, Auger, and photoelectric emission. These calculations predict resonances in the transmission for suitable choices of model potential

parameters which may reasonably approximate alkali atoms adsorbed on metal surfaces.

Recently, Connor[26] has brought out certain interesting features of resonance tunneling. He also has presented a two-peak transmission coefficient valid for electron energies greater and less than the barrier maxima. Thus, this expression could be used for a unified theory of thermionic and field emission for a two-peak potential model. This article contains extensive references on previous work on tunnel resonance.

In reality, field emission is not solely a one dimensional problem, The emitter itself is pseudospherical, and the patch field effect, and the presence of the tip shank cause electric fields parallel to the emitter surface.

A recent paper by Politzer and Feuchtwang[27] represents an early step in considering some of these aspects. Here, field emission from a spherical tip is formulated in terms of scattering theory. The usual transmission coefficient is replaced by a differential scattering probability.

D. Determination of the Work Function Using the Fowler-Nordheim Equation

The current I and the voltage V are the experimentally measured quantities. Thus, using

$$I = AJ \tag{IID.1}$$

and

$$E = \beta V \tag{IID.2}$$

the Fowler-Nordheim equation becomes

$$I = \frac{1.54\times10^{-6}\beta^2V^2A}{\phi t^2(y)} \exp[-6.83\times10^7 \frac{\phi^{3/2}}{\beta V} v(y)]\text{amp} \qquad \text{(IID.3)}$$

This can be written in the form

$$\log\left(\frac{I}{V^2}\right) = \log\left[\frac{1.541\times10^{-6}\beta^2A}{\phi t^2(y)}\right] - 2.967\times10^7 \frac{\phi^{3/2}}{\beta V} v(y) \qquad \text{(IID.4)}$$

β varies over the emitter surface (although, as seen below, this variation is often neglected) but is assumed to be independent of the tip voltage. As seen in Section II-C t(y) is almost constant. Taking A, β, and ϕ to be independent of V, and t(y) constant, the slope of $\log (I/V^2)$ vs 1/V takes the simple form:

$$m = \frac{d \log(I/V^2)}{d(1/V)} = -2.967\times10^7 \frac{\phi^{3/2}}{\beta} s(y) \qquad \text{(IID.5)}$$

where

$$s(y) = v(y) - \frac{1}{2} y \frac{dv(y)}{dy} \qquad \text{(IID.6)}$$

According to this model, this plot, called the Fowler-Nordheim (F-N) plot, results in a straight line, except at higher currents where the image force term s(y) varies noticeably. If the F-N model were simplified by neglecting the image force, s(y) would be unity and the F-N plot a straight line. Experimentally, space charge effects at higher current also cause deviations from the linearity.

The slope of the F-N plot yields $(\phi^{3/2}/\beta)\ s(y)$. Thus another relation between ϕ and β or the independent determination of β is needed to obtain ϕ.

The intercept q of the F-N plot is given by the following relation

$$q = \log\left[\frac{1.541\times10^{-6}\beta^2 A}{\phi t^2(y)}\right] \qquad \text{(IID.7)}$$

This therefore supplies another relation between ϕ and β. In the simplified model without the image force, the F-N plot results in a straight line and the actual intersection of this line with the y-axis would equal the pre-exponential factor of the simplified equation. However, in the model with the image force, the extrapolation of the linear part of the curve would not result in q, but in a larger number. Thus q must be obtained from Eq. (IID.4) using values of I and V within the experimental data. However, the emitting area A is unknown, and thus Eq. (IID.4) cannot be used with Eq. (IID.5) to obtain β and ϕ.

By using the proper etching technique, the general shape of an emitter can often be approximated by one of the family of equipotential surfaces resulting from various geometrical shapes. If the experimental anode surface is also represented by one of the equipotential surfaces, the electric field can be calculated at each point and the value of β everywhere on the emitter determined.[5] With this method, the emitter shape is determined by electron microscopy. A typical core structure used is the sphere-on-orthogonal cone. This model reveals that the field is highest at the emitter apex and decreases slowly as the angle from the apex increases.[28]

The calculated decrease in field is less for emitters with a constriction in the shank just behind a "bulbous" end form. Dyke and Dolan[28] have graphed β/β_0 vs θ (apex angle) for the two shapes often encountered. Here β_0 is the value of β at $\theta = 0$. For one, showing a slight constriction, $\beta/\beta_0 \cong 0.90$ at $\theta \cong 57°$. For another, with no constriction, $\beta/\beta_0 \cong 0.90$ at $\theta \cong 50°$. Gomer[5] has shown that the resulting decrease in emission current according to the F-N equation is much steeper, resulting, for the first case, in $J/J_o \cong 0.35$ at $\theta \cong 57°$, and for the second, in $J/J_o = 0.1$ at $\theta = 50°$. Consequently, the calculated variation in the field over the visible portion of one of these simplified emitters is quite small.

Ovchinnikov and Tsarev have used the above approach in their probe FEM study of cesium adsorption on the crystallographic faces of tungsten.[29] They determined the size parameter in their equation for β/β_o by measuring the current-voltage characteristics for the $(\bar{1}21)$ and $(\bar{2}11)$ planes, which are at different distances from the tip apex, and assuming their work functions were the same.

It is desirable to use tips that have a neck behind a spherical end (called "wide angle" tips) because the often used assumption that β is constant over the imaged area is then closer to the actual situation. If planes appear at the periphery of the FEM pattern which are 180° apart, such as the $(1\bar{1}0)$ and $(\bar{1}10)$ planes in a (110)-oriented tungsten tip, then such a structure is present.[30] This shape can be easily obtained by heat flashing (See Sec. IIIE.2).

By comparing the F-N slopes of pairs of identical planes at different angular distances from the tip apex, Mueller found a drop of 0.15% per degree for these "wide angle" tips.[30] This value agrees with the equipotential surface results of Dyke and Trolan.[31]

Swanson and Crouser[32] used Mueller's technique. Their values of β/β_0 agree well with those obtained by Dyke et al.[33] using equipotential surfaces to represent emitters having slight and pronounced constrictions.

The previous discussion has neglected the fact that due to the crystallographic planes present on the emitter surface, the emitter is not the smoothly curving structure assumed to this point. The value of β is less over a flat region than over a curved region of the emitter, and thus this effect is superimposed on the macroscopic effects discussed above.

Mueller has determined that the reduction in field at the center of a plane can amount to several percent for larger planes. For (011)-oriented tungsten emitters he used field reductions of 3% for the (011) plane with a 5.5° half angle, and of 0.5% for the (112) plane with a 2.5° half angle.[30] For field evaporated specimens, there are differences of local radii of curvature produced by the shaping proeess (see Sec. IIIE).

Because the above quantities are hard to obtain precisely, other methods are being increasingly used at present. The temperature variation of field emission and the energy distribution of the field-emitted electrons each provide another relation between ϕ and β and are thus used. These will be discussed in subsequent sections.

Gomer and co-workers (see, for example, references 5, 8 and 11) have often determined the voltage-field factor for tungsten emitters by assuming the average work function of a tungsten emitter is equal to 4.50 eV. They used the F-N equation in the simplified form,

$$\ell n(I/V^2) = \ell n\ A - b\phi^{3/2}/V \qquad \text{(IID.8)}$$

where $\ell n\ A$ is the pre-exponential factor, and b is a constant given by

$$b = 0.68/c \qquad \text{(IID.9)}$$

where

$$cV = E \qquad \text{(IID.10)}$$

E is the field in volts per angstrom. b was determined from the slope of the F-N plot for the total emitted current and the value of ϕ_{ave} noted above. The current from several planes was measured by moving the emitter. b was calculated for each position, and then used in single plane work function ($\phi_{hk\ell}$) measurements.

This method has obvious simplifications and definite uncertainties. For it to be used at all, ϕ_{ave} must have been calculated from a field emitter rather than a macroscopic polycrystalline sample, since the planes emphasized in each are different, and the ϕ_{ave} of a field emitter is a complicated average of the single plane work functions in which the low work function planes predominate.[24]

Another frequently used relation, which can be derived from the expression for the slope of the F-N plot, [Eq. (IID.3)] is

$$\frac{\phi_i}{\phi_j} = \left(\frac{m_i}{m_j}\right)^{2/3} \left(\frac{\beta_i}{\beta_j}\right)^{2/3} \qquad \text{(IID.11)}$$

where i refers to a single plane, and j can refer to another single plane or to the whole emitter. In deriving Eq. (IID.11), it was assumed that s(y) is the same for both i and j.

Sidorski, Pelly, and Gomer[34] have presented still another approximate relation between $\phi_{hk\ell}$ and ϕ_{ave}, which they used in the high work function regions of a tungsten emitter. In this equation,

$$\phi_{hk\ell} \cong \phi_{ave} \left(\frac{\log i_2/i_1}{\log I_2/I_1}\right)^{2/3} \qquad \text{(IID.12)}$$

Here i_1 and i_2 refer to the emission currents from the probed region at any two voltages, V_1 and V_2, for which the total emission currents are, respectively, I_1 and I_2. According to the authors, this relation can be derived from the F-N equation. If $i_1/i_2 = 10$, this equation reduced to

$$\phi_{hk\ell} \cong \phi_{ave} [\log(i_2/i_1)]^{2/3} \qquad \text{(IID.13)}$$

which enables $\phi_{hk\ell}$ to be rapidly determined.

Unless temperature variation or energy distribution measurements are used to obtain other relations between β and ϕ, then the only experimental quantities available are the total current I, the applied voltage V, and the slope m of the F-N plot. Both the work function ϕ and the electric field strength E at the surface are unknown, and

E and ϕ appear both explicitly and implicitly through the variable y. Because of this, an iterative method must be used to obtain absolute values of ϕ from the full F-N equation. In view of this, it is instructive to think about the emitting area from which the electrons passing through the probe hole originate.

The electron trajectories near the outside of the pattern are bent towards the center of the pattern because of the effect of the shank on the potential lines. Thus, on the basis of the general tip shape, one would expect the magnification to decrease as the apex angle increases, This means that the emitting area from which the probe electrons originate would increase as the apex angle increases.

However, van Oostrom[16] (and others) have found that this effect is opposed by a magnification reduction over large flat planes. In his studies of (110)-oriented tungsten, van Oostrom found that the magnification of the large (110) plane was smaller than that of any other plane, making the probe emitting area for that plane much larger. In fact the emitting area measured for the (110) plane was about 80 times larger than that measured for the (211) plane.

If the local magnification is independent of the tip voltage, then the emitting area for a clean surface is also constant, and no calculational problems are introduced in this regard.

According to Gowdy[7] another uncertainty in the emitting area is introduced in probe measurements by the focusing effect of the probe hole assembly and the presence of the suppressor grid through which the electrons must pass. These effects are not independent of the

tip voltage, but, because the magnitude of their effect is uncertain, it is assumed that they do not change appreciably over the voltage measurements.

III. RESEARCH TECHNIQUES

The present chapter briefly describes some of the pertinent techniques commonly utilized for the study of work functions with an emphasis on field emission and the associated technique of field ionization. The classical methods of thermal emission and photoelectric emission are briefly summarized.

A. Thermal Emission Method

One of the most common methods used for the determination of work functions is thermal emission of electrons from a heated metal surface. Some measurements using single crystal wires have been made using Smith's method.[35] With this method the electrons emitted from the hot cathode are collimated and accelerated into a Faraday's cage serving as anode. The sample can be rotated to determine the dependence of ϕ in crystal orientation. If the anode voltage chosen is large enough so that the electron current has attained its saturation value (i.e. is not space charge limited); then the electron current density j depends on the temperature T, and the work function ϕ can be obtained in accordance with Richardson equation

$$jo = AT^2 \exp[-e\phi/KT] \qquad \text{(IIIA.1)}$$

where

$$A = \frac{2\pi M_e}{h^3} = 120 \text{ amp sec/cm}^2 \text{ degree}, \qquad \text{(IIIA.2)}$$

in which M_e is the electron mass, K the Boltzmann constant and e the charge of the electron. Plotting ln (jo/T^2) against 1/T gives the

Richardson line, and from its slope the work function can be determined.

B. Photoelectric Method

This method has also been successfully applied to the determination of work functions of clean and gas covered surfaces. The maximum kinetic energy (E_{max}) that our electron can attain at 0 K after absorption of a photon and overcoming the potential barrier has been shown by Einstein to be

$$E_{max} = h\nu - (e\phi)_{T=0} \quad . \tag{IIIB.1}$$

Then, there is no possible photoelectric emission for $h\nu < e\phi$, and $\nu_o = e\phi/h$ gives the lowest frequency at which the effect can occur. One can then write

$$E_{max} = h(\nu-\nu_o) \tag{IIIB.2}$$

This relation is used to determine the work function.

If the voltage V applied between the photocathode and the anode is just sufficient to prevent the emission of electrons from the photocathode, it can be written that

$$eV = h(\nu-\nu_o) = h\nu - e\phi \tag{IIIB.3}$$

If the frequency ν is known, the work function $e\phi$ can be determined from the above equation. However, since the actual measurement must be made at $T > 0$ K the kinetic energies of the electrons may be greater than E_{max}, and this method will yield imprecise work functions. More

exact methods have been devised which take into account the photoelectron current density, the irradiation frequency and the temperature. They are well discussed by Kaminsky[36] and will not be included in this thesis.

C. Field Emission

The emission of electrons from the surface of a condensed phase into another phase, [(usually vacuum) under the action of a high electrostatic field (0.3 to 0.6 volts/Å)] is called field emission.

Emission of electrons from a metal surface can be attained by supplying the electron with the energy necessary to overcome the potential barrier; that is the work function ϕ. When this energy is supplied by bombarding the metal with electrons, we have secondary electron emission. When the energy is supplied by photons we have photoelectric emission, and when it is supplied by phonons we have thermionic emission. In field emission, however, instead of overcoming the work function, the surface potential barrier is deformed by the field in such a way as to give electrons a higher probability of tunneling through.

For a triangular barrier of height ϕ and width ϕ/Fe (Fig. 1a), the tunneling probability has been found to be proportional to

$$\exp\left[-\left(\frac{2m}{h^2}\right)^{1/2} \frac{\phi^{3/2}}{Fe}\right] \qquad \text{(IIIC.1)}$$

for electrons at the Fermi level.

If the image potential or Schotky effect is included, the triangular barrier is rounded up as in Fig. 1a and reduced by an amount $(e^3F)^{1/2}$.

Fowler and Nordheim,[13] using this type of barrier, calculated the current density of electrons produced by field emission, which yielded the well-known Fowler-Nordheim equation

$$J = 6.2\times10^{-6} \frac{(\mu/\phi)^{1/2}}{Ff+\phi} F^2 \exp\left(\frac{-6.8\times10^7 \phi^{3/2} a}{F}\right) \qquad \text{(IIIC.2)}$$

where μ is the Fermi energy measured with respect to the bottom of the conduction band and is expressed as ϕ in electron volts when F is expressed as electron volts/cm and J is amps/cm^2.

D. Field Emission Microscopy (FEM)

A tip or sharply pointed cathode placed in a high vacuum pointing toward a zinc sulfide screen produces an enlarged image of the emitting surface, once a high potential between the cathode and the screen is established. The field at the surface of the cathode is related to the voltage V by using the expression

$$F = \frac{V}{kr} \qquad \text{(IIID.1)}$$

where r is the mean radius of curvature of the emitter surface and k is a quasi constant that depends on the geometry of the electrodes ($k\simeq5$).

As the image on the screen is a radial magnification of the emitter's surface, we can write the magnification attained as $R/\beta r$ where R is the emitter to screen distance, r is the emitter radius and β is a constant depending on the microscope's geometry ($\beta \simeq 1.5$).

The resolution δ of the field emission microscope in terms of distance on the emitter surface can be written as

$$\delta = 2.62\times10^{-4}\beta\, R^{1/2}\left(\frac{1.16}{\beta V^{1/2}} + \frac{1}{K\alpha\phi^{1/2}}\right)^{1/2} \qquad \text{(IIID.2)}$$

where δ and R are in centimeters and V in volts[37] and α is a constant. The first term is the contribution of the transversal momenta and the second is the diffraction effect. For a crystal of 10^{-6} cm of radius, ϕ = 4.5 eV and $F = 5\times10^{7}$ volts/cm the predicted resolution is of the order of 20 Å.

The origin of the brightness contrast in the field emission image may be seen from the Fowler-Nordheim equation (Eq. IIIC.2). As the emitted electron current depends exponentially on $\phi^{3/2}/F$ then slight variations of work function and local field will be displayed in the image.

Variations of F reflect changes on the effective local radius of curvature (Eq. III.D.1) and consist of relatively large-scale variations caused by the overall shape of the emitter and shorter range variations due to the topography of the surface. However, the dominant variable determining the contrast in the field emission image is the work function which changes with crystallographic orientation, composition and adsorbed impurities.

Summing up, the technique of field-emission microscopy permits the observation of small variations in the work function and local curvature of the specimens with magnifications of ~ 10^5 and resolution of ~ 20 Å.

This technique has been applied in adsorption phenomena, work function measurements and diffusion phenomena.

1. Techniques Using the Field Emission Approach

Three of the techniques commonly used to measure work functions using FEM are:

a. Scintillation Technique

b. Energy-Analyzer Technique

c. Probe Hole Technique

a. Scintillation technique. Wilkinson[41] and later Dyke, Trolan, Dolun and Grundhauser[33] tried to measure electron current densities by directly measuring the direct light output.

Nottingham[38] had shown that the light output from a phosphor per unit current striking it, varies with the potential of the phosphor according to the relationship

$$\frac{L}{I} = kV^n \qquad \text{(IIID.3)}$$

where L is the light output from the phosphor, I is the electron current striking the phosphor, V is the potential of the phosphor and K and n are constants. The value of n varies with the type of phosphor and it may vary to a small degree for different samples of the same phosphor. With Z_nS:Cr screen excited by electrons

quantum yields of 0.30 to 0.065 photons/eV. When excited by ions of limited penetration power, the screen brightness increases somewhat more than linearly with ion energy following a function about $V^{1.1}$ to $V^{1.5}$. Data obtained by Wilkinson from ZnS:Ag screen show a value of n for electrons of 2.5 using a willemite screen he obtained n=2.0.

The light output can be measured with a microphotometer from the photographic film, for a given voltage a light output L is linearly related to the electron current.

$$L = K(V)^n I = CI \qquad \text{(IIID.4)}$$

C depends on the film sensitivity, the power of the light beam, the sensitivity of the microphotometer, and the voltage. From the current derived from the light output, ϕ can be derived using the F-N equation.

Muller[40] points out that the light output from an area might not be a simple function of the electron density of the beam originally emitted this may be due to internal reflection of the walls of the tube and the inside of the phosphor and also to excitation of the dark screen areas by soft x-rays within the tube.

All these factors will tend to diminish the contrast between the dark and light areas of the image. If there are, in fact, image contrasts, then we can assume that the electron density emitted is different even if the difference is larger than that ascertained by intensity measurements. The work of Wilkinson[41] show that the work function obtained from the slope of the Fowler-Nordheim plots which have been measured scintillation exceed the expected work functions

for the same planes of W as measured by Nichols and Mendenshall. Wilkinson's slopes however keep a linear relationship with the latter results. Then, the scintillation method can be properly used to attain work function differences but not measurements of absolute work functions.

b. Energy-analyzer technique (Swanson and Crouser).[42] This technique is based on the total energy distribution expression

$$J(E) = \frac{J_o \, e^{\varepsilon/d}}{d(1+e^{\varepsilon/pd})} \qquad \text{(IIID.5)}$$

where

$$P = \frac{KT}{d}, \quad E = E - E_f \text{ (Fermi energy)}$$

$$\varepsilon = \frac{9.76\ 10^{-9} F}{\phi^{1/2} t(y)} \qquad \text{(IIID.6)}$$

F = applied field

$t(y)$ = image correction

ϕ = work function

Utilizing a retarding potential analyzer, the electrons emitted by the tungsten tip can be collected at a metal surface of work function ϕ_o, when their energy E exceeds $\phi_c + Ef - Ve$

$$E > \phi_c + Ef - Ve,$$

Vt is the emitter to collector bias potential. Increasing Vt allows all

electrons emitted down to a certain energy level $\varepsilon = \phi_c - Ve$ to be collected.

At T = 0°K the condition $Ve = \phi_c$ represents the current cutoff since the electronic states above E_f are not occupied. The total collected current Ip at a specified value of ε is given by

$$Ip = \frac{Io}{d} \int_o^{-\varepsilon} e^{\varepsilon/d}\, de = J_o(t - e^{-\varepsilon/d}) \qquad \text{(IIID.7)}$$

where J_o is the maximum field current.

Rewriting this equation in a workfng form we obtain

$$\log_{10} \frac{(Io-Ip)}{J_o} = \frac{-\phi_c}{2.3d} + Vt/2.3d \qquad \text{(IIID.8)}$$

Then, values of d and ϕ_c can be obtained from the slope m_c and the intercepts of a plot of the curve $\log_{10}$ (Io-Ip)/Io versus Vt.

Basically, this procedure requres an energy analyzer and a collector, as measurements of the electron currents have to be made simultaneously with current measurements.

c. Probe hole technique. A somewhat simpler technique used by Müller[43] has been the probe-hole technique.

A probe hole made in the screen, would allow electrons to pass through and their current measured under vacuum conditions. The size of the hole is made to match the image of the plane under study, and the current measuring device consists simply of a collector and a Faraday cage.

The work function is ascertained by direct application of the Fowler-Nordheim equation (Eq. IIC.2). Using the slope of the plot of log J/F^2 vs $1/F$, ϕ can be calculated.

E. Field Ionization

Field ionization is the ionization of a free atom by tunneling the electron through the deformed potential barrier (due to a strong external electric field). The field utilized in field ionization is much higher than that of field emission (2 to 5 volts/Å).

A higher applied field deforms the potential surface of a positively charged anode in such a way that it permits the ionization of a free gas atom. This will occur if the electron tunnels from its ground state in the mother atom into the metal surface (Fig. 2). When the atom is near the surface, the former becomes polarized and the effect of the proximity of its charge on the surface potential barrier further reduces the width by image forces.

The barrier penetration probability for the tunneling electron may be found by the W.K.B. approximation, yielding

$$D = \exp\left[-\left(\frac{8m}{h^2}\right)^{1/2} \int_{X_2}^{X_1} (V-E)^{1/2}\, dx\right] \qquad \text{(IIIE.1)}$$

where X_2-X_1 is the width of the potential barrier, m is the electron mass and E is the total energy.[39]

The frequency of ionization is given by

$$f = \nu D \qquad \text{(IIIE.2)}$$

where ν is the frequency with which the electron hits the potential barrier as estimated from Bohr's atomic model.

Because the radius of curvature affects the local field, as we saw in the expression $F = V/Kr$, the areas of larger radius of curvature will appear darker in the field ionization picture than those of smaller radius of curvature.

In general, the ion current produced by the imaging gas as it is ionized near the surface of the specimen depends on the amount of gas atoms available at the tip and the number of atoms being either ionized or diffused away from the tip's area.

Considering that all the atoms that arrive at the tip are ionized, the ionic current is given by

$$i = \alpha S q \qquad \text{(IIIE.3)}$$

where α is a semiconstant depending on the number of the diffused ions, q is the ionic charge, and S is the supply function given explicitly by

$$S = \sigma_{eff} P(2\pi KT)^{-1/2} \qquad \text{(IIIE.4)}$$

where $P(\text{dynes/cm}^2)$ is the gas pressure, and σ_{eff} is the effective cross section of the tip. The effective cross section differs from the geometric cross section σ_g by the factor $(1 - 2V(F)/3KT)$ where

V(F) is the potential energy of a particle in the field F.

Thus the ion current can be written as

$$i = \alpha \left[1 - \frac{2V(F)}{3KT}\right] \sigma_g P(2\pi KT)^{-1/2} \qquad \text{(IIIE.5)}$$

If we take into account that some of the atoms bounce on the tip and then, instead of being ionized, diffuse down the shank of the specimen, the ion current must be expressed as

$$i = 2\pi r_t^2 x_c q C_t \frac{KiKd}{Ki+Kd}$$

$$x_c = \frac{I-\phi}{cF} \qquad \text{(IIIE.6)}$$

where x_c is the critical approach at which an atom can be ionized. I is the ionization potential, ϕ is the work function and F is the applied field.

$$Ki = \left(\frac{KT}{2\alpha_p}\right)^{1/2} \frac{r}{T(I-\phi)} \exp \frac{(-2(I-\phi)\alpha_p F_o)}{\gamma \epsilon KT} \qquad \text{(IIIE.7)}$$

$$Kd = \frac{(2KT)^{3/2}}{m^{1/2}\alpha_p F^2 r} \qquad \text{(IIIE.8)}$$

and α_p = ionization probability, T = period spent by the atom, within ionization range, m = mass of the gas atom, r = radius of curvature.[39]

F. Field Ion Microscopy (FIM)

In the field ion microscope the specimen is positively charged and gas is allowed at low pressure into the instrument's chamber. The image is formed on the fluorescent screen by the positive gas ions produced near the specimen's surface, when electrons from the gas atoms tunnel into the specimen. The magnification of the field ionization microscope is radial as is that of the field emission microscope. Because of the larger de Broglie wavelength of gas ions, compared to that for electrons, the field ionization microscope has a resolution of the order of an atomic diameter.

The minimum resolvable distance in the field ion microscope is given by:

$$\delta = \sqrt{4r\beta(KT/Ve)^2 + \left(\frac{4\beta^2 r\hbar^2}{2KMF}\right)^2} \qquad \text{(IIIF.1)}$$

where r is the tip radius, $\beta \approx 1.5$ (depends on geometry), V is the voltage (V=KrF) and T is the absolute temperature,[39] M is the atomic mass of the imaging gas and F the external field.

For helium at - 20 K the resolution attained is 3 Å for emitters of 1000 Å in diameter and $V = 10^4$ volts.

G. Specimen Preparation

Specimens for FEM or FIM are prepared from thin polycrystalline wires electrically polished to form a conical needle. The tip of the needle must be invisible with a 250x microscope. The last stage in

the preparation of the FIM - FEM specimen requires attaining an almost perfectly hemispherical emitting surface, free of impurities and protruding atoms. Such a surface can be accomplished either by field evaporation or by heat flashing.

1. Field Evaporation

This technique is based on lowering the activation energy[39] required to evaporate an ion from the surface of a metal, by applying a high electrid field.

a. Field evaporation of pure metals. The field required to evaporate surface atoms from kink sites on the metal surface depends on the sublimation energy λ, the ionization potential I_n and the work function ϕ of the plane containing the evaporating atom. This has been expressed, as:

$$F = (en)^{-3} [\lambda + \sum_n I_n - n\phi]^2 \qquad \text{(IIIG.1)}$$

where n is the number of electrons depleted from the atom.

For a given applied voltage V the field F will be different for different sites of the specimen depending on the local work function and also on the local radius of curvature (Eq. IIID.1).

The evaporation rate Ke, is an Arrhenius type of relation

$$Ke = \nu \exp[-Q/KT] \qquad \text{(IIIG.2)}$$

$$Q = [\lambda + \Sigma I_n - n\phi_o] - (n^3 e^3 F)^{1/2} \qquad \text{(IIIG.3)}$$

where ν is a frequency factor and Q is the activation energy for field evaporation. Q is, to a first approximation, temperature independent.

Thus, the evaporation rate depends exponentially on the work function and the field. A large work function will produce an increase of the exponential factor and a preferential field evaporation of the high work function area. Also a large local field, as produced by a protruding atom (a kink atom or an impurity) will produce preferential field evaporation of these atoms.

The field evaporation end form of the specimen will then present a smooth, almost spherical surface, topped by small regions of different radii of curvature. These local differences of radius of curvature produce differences of brightness in the field ionization photomicrographs.

b. Field evaporation of dilute alloys. According to Brandon,[44] the modified sublimation energy for a monoatomic ion of a solute species can be given by the approximation

$$\lambda \approx \lambda_o - \Delta\bar{H}_s \qquad \text{(IIIG.4)}$$

where λ_o is the sublimation energy of the pure solute and $\Delta\bar{H}s$ is the relative partial molar enthalpy of solution. When the solute is a monoatomic gas

$$\lambda \approx \lambda_o - H_s \qquad \text{(IIIG.5)}$$

solution per gramatom of gas in the standard state. If the solute is a dimolecular gas

$$X \rightleftarrows E_d + H_a \qquad \text{(IIIG.6)}$$

where H_a is the heat of adsorption per gramatom of gas in its standard state and E_d is its dissociation energy.

To a first approximation $H_s \simeq -\Delta\bar{H}_s$ but values of $\Delta\bar{H}_s$ are to be preferred for these calculations when they are available.

For some diatomic gases H_s and H_a have been determined and it has been consistently observed that $H_s < H_a$, indeed in general $H_a > -\Delta H_F > H_s$, where $-\Delta H_F$ is the heat of formation of the appropriate compound per gramatom of gas. As a result, the solute atom has a lower free energy at the surface than in the bulk, and the difference in energy must appear as a reduction in the binding energy of the nearest neighboring atoms. Therefore, as field evaporation proceeds, solvent atoms directly above the solute atom will evaporate preferentially if by doing so they uncover the underlying solute atom.

This effect has been observed by Machlin.[45] Brandon[44] has calculated the evaporation fields of various solutes in an iron matrix. Of those listed Cr, Mn, Co, Cu and Al are expected to field evaporate preferentially while the rest of the metals will be retained on the surface.

2. Heat Flashing

The method of heat flashing consists of heating the tip electrically in vacuum to the point where contaminants decompose or evaporate. By this method alone it is not possible to clean metals with melting temperature lower than 1300°K.

Heating above a critical temperature causes surface diffusion which yields a spherical bulb at the tip of the emitter; and, if heating is continued, it produces blunting to the point where field ionization is no longer possible. Surface diffusion depends on the energy H_f necessary to produce mobile surface atoms and surface vacancies and the activation energy H_a to move the atom or vacancy on the surface. These energies depend on the atomic packing; thus, they vary from one surface orientation to another.

It is expected that formation of mobile atoms on close-packed planes requires a larger energy H_f than on loosely packed planes. However, it should be easier to move an atom on the relatively smooth surface of a close-packed plane than on the rough surface of a high index plane.

These two factors account for a slight buildup of material on the tip's surface in certain crystallographic directions when the crystal is heated to temperatures where surface diffusion is possible.

The end form of a "buildup" tip will have accumulated surface atoms at the low work function (high index) planes and a depletion of atoms at the low work function areas of the tip. Thus buildup accentuates the dark areas (high work function areas) of the emission

micrographs in contrast with the high emitting (low ϕ) areas. A more severe buildup can be attained if flashing is done with the high electric field on.

H. Image Interpretation of Field Ion Micrographs

Field ion micrographs of pure metals and alloys usually present regions of different brightness. The most outstanding features commonly observed are zone line decoration, symmetric regional image brightness, brightness contrast within the same crystallographic plane, bright streaks and dark zone or dark band symmetrical patterns.

The following is a brief description of these features and the explanations of them that have been published up to now.

1. Zone Line Decorations

Zone line decorations are rows of single atoms and groups of atoms that are substantially brighter than the rest of the atoms observed in the FIM. They occur along zone lines like the (110)-(100) sector of the tungsten micrographs (Fig. 15.1)

These zone lines have been explained by Müller[39] as isolated atoms sitting at metastable surface sites; however, Tong and Gilman[46] showed that the outstanding bright spots could be resolved into groups of three or four (triads and tetrads) on metastable positions.

2. Regional Brightness

Symmetric regional image brightnesses are brighter regions observed at a specific crystallographic orientation. Such regions could be accounted for by varying local radii of curvature due to preferential field evaporation.[39]

The brightest region of tungsten is around the {111} plane and the darkest is the {110} region (see Fig. 15.1). Also, the radius of curvature in the {110} region is several times larger than that of the {111} region. This dependence of brightness on radius of curvature can be better understood from Eqs.(IIIC.6 to 9). The larger r is, the smaller the ion current I will be.

3. Zone Brightness Contrasts

Brightness variations along certain zones are especially obvious in tantalum molybdenum and platinum. These sharp contrasts around regions that are assumed to have the same radius of curvature have been explained by Moore and Brandon[47] who took into account the changes in the atomic environment of the imaged atoms. They suggested that atoms with more than a critical number of first and second nearest neighbors do not appear in the field ion image and that the bond geometry of more distant neighbors can be correlated with overall variations of intensity in different areas of the stereographic triangle formed by {100}, {110} and {111} poles as vertices.

4. Dark Zone Patterns

Dark zones have been observed in micrographs of different metals under some imaging conditions. They are symmetrical dark bands stretching from one major crystallographic pole to another on the image. In some ways they are similar to the previously described brightness variation. These are very conspicuous effects in nickel alloys (Ni_4Mo) and have received ad-hoc explanations by different authors. The effect of dark zone regions was observed initially in nickel-molybdenum, by

LeFevre, Grenga and Ralph,[48] who observed a dark band pattern in the field ion micrographs of Ni_4Mo. They pointed out that these bands did not go through domain boundaries and did not seem to be symmetric with respect to the image. They tended to pass through fundamental planes and by-pass the major superlattice planes. They explained that the superlattice planes contain Ni and Mo layers alternately, while the fundamental planes are mixed. Thus, as W tends to image preferentially, the fundamental planes will tend to look darker. This appeared to be the origin of these dark zones.

Newman and LeFevre[49] also worked with Ni_4Mo and observed not only the dark zone pattern joining the major fundamental planes, but a secondary zone pattern, of thinner bands, which joined the superlattice planes. They attributed the dark zone pattern to the shape of the Fermi surface (following Nakamura and Müller). They considered that regions where the Fermi level approaches the Brillouin zone boundary correspond to directions in K space for which there is a reduced number of available energy states, thus a smaller probability of electrons tunneling in. The ionization probability of helium atoms is then smaller in these regions.

Using the shape of the Fermi surface of Ni for Ni_4Mo, they condluded that as it necks up toward the (111) direction (if we assume it is spherical elsewhere) there was a smaller probability of ionization in that direction. That would explain the darker bands in Ni_4Mo around the (111) planes. However, Newman and Hren[50] working with ordered and disordered forms of Ni_4Mo, did not find the

zone pattern at liquid helium temperature. No paper considering band structure in the disordered Ni_4Mo is known to the author.

The explanations for zone decorations, symmetric regional image brightness, and brightness contrasts within the same crystallographic plane have been fairly well accepted by field ion microscopists. However, there does not seem to be agreement in the origin of dark band formations as they appear in nickel and some of its alloys. Fe, Co and Ta, field evaporated at liquid nitrogen temperatures, also show the dark zone pattern extending from the major crystallographic planes.

In a previous work by the author[51] the field ionization micrographs of the Ni_4W as-quenched from 1300°C (α phase) showed a dark zone pattern when the specimen was observed at temperatures around the liquid nitrogen boiling point (78°K). The bands seemed to depart from the {111} poles and oriented toward the {110} poles (see Fig. 18). A second,pattern, not as dark as the first, was observed extending from the {100} poles toward the {111} poles (see Fig. 19). The dark band patterns as a whole disappeared upon cooling of the specimen to around liquid helium temperatures (4.2°K).

The dark band pattern was explained using a topographic model based on preferential field evaporation at the $\{11\bar{1}\}$-{110} regions of the specimen due to a higher work function of the planes involved.

Previous explanations of the dark band pattern in pure nickel and in Ni_4Mo, failed to account for the temperature dependence and other characteristics. The use of FEM in conjunction with FIM proved effective in making it possible to discard some of the previous

hypotheses and in ascertaining the work function as the primary cause behind the dark band formation.

5. Streak Contrasts

Some specimens show bright streaks in the field ion images that can not be considered zone dependent. Ralph and Brandon[52] interpreted the streaks seen in deformed tungsten-rhenium alloys as due to the step produced where a stacking fault on the {112} plane intersects the crystal surface. Ranganathan et al.[53] in a comprehensive study of streaks, shows that they might be the product of different causes. For example, specimens could sometimes present a forked and two images would be superposed. The superposed images present bright streaks, and present an obvious superposition of well imaged crystal planes. Specimens like this could be the result of poor electropolishing or irregularities produced by corrosion or bombardment. Interfaces also produce streaks but they are easy to interpret due to the mismatch of crystal planes. Slip planes and dislocation pileups have also been considered as the source of streaks.

IV. EXPERIMENTS ON WORK FUNCTION CHANGES WITH ADSORPTION (A Review of the Literature)

To complement the works cited in the previous chapters, it seems important to include a brief review of some pertinent experiments of adsorption using field emission microscopy and other techniques.

The field emission microscope has been used since the early 1950's as an instrument to study the processes which take place when foreign atoms or molecules are adsorbed on metal surfaces. Most of these works emphasized that the electron work function varies from one crystallographic plane to the next and that, in adsorption phenomena, the arrangement of the metal atoms on the surface plays an important part. In the last ten years, the powerful technique of field ionization has been used to complement data with respect to the exact position of adatoms on the crystallographic planes of the substrate. The subject of adsorption on metal substrates has been discussed in section IIB; however, it seems appropiate to review some of the ideas exposed at this time.

Adatoms and adions can be distinguished by the electrical fields or potentials they produce and by the way in which these fields affect the emission of electrons, ions and atoms from the substrate's surface. A positive adion induces a negative charge on a metal substrate and acts as a positive dipole. An array of such dipoles would produce large fields (of the order of 10^8 volts/cm) near the surface. As these fields are in a direction to make it easier for electrons to escape, adions lower the work function for electrons and are not preferentially evaporated under a strong external field.

Adatoms, on the other hand, particularly if they form paired electron bonds, would be expected to produce much smaller fields than ions and consequently affect electron emission only slightly.

Some of the alkali metals adsorbed on tungsten have especially attracted the attention of investigators because of the abrupt variation of the work function of the tungsten emitters. Langmuir and Kingdon, as early as 1924,[54] studied the adsorption of cesium on tungsten. They observed, among other things, that adsorbed cesium increased the thermionic electron emission enormously, and hence they deduced that the electron work function was drastically decreased. Ives et al.[54] arrived at the same conclusion using photoelectric emission. These experiments showed that, as the amount of adsorbed cesium, θ, increased, the electron work function, ϕ_e, decreased to a minimum value and then increased toward the value of bulk cesium. Later on, Becker devised a method for measuring θ over a considerable range of arrival rates and tungsten temperatures. He found that the coverage was 3.7×10^{14} cesium atoms per cm^2 of tungsten surface when the work function was minimum. This is nearly equal to 1/4 the number of W-atoms per cm^2 and 110 plane. Makukha[55] studied the emission and preferential adsorption of cesium films on a tungsten single crystal using an electron projector with a double spherical "jacket" which produced a directed beam of cesium atoms. He obtained a value for the minimum work function of 1.6±0.1 W. He also calculated the bulk work function for cesium as 1.9±0.1 W, and pointed out that the preferential adsorption for cesium on tungsten was on the faces

{112}, vicinites of {110} faces and between the principal crystallographic directions (high-index phases).

This experiment in relation with the theory developed later, suggests that adhesion atoms tend to accumulate on the areas where more free bonds are present. It will be observed that similar curves, have been obtained by various authors showing the work function dependence on the duration of deposition using different metals as adatoms.

Moore and Allison[56] studied strontium and barium deposited on W ribbon-receivers by evaporating from filaments in which a chemical reaction produced the pure metals. They calculated the work function ϕ for a monolayer of Sr as ~ 2.2 eV and for Ba as ~ 1.9 V. The thermionic activation was explained in terms of polarized adatoms rather than the usual assumption of partial ionization which according to them had no experimental justification for Sr and Ba films.

From heats of desorption and a theory of Prosen, Soxhs and Teller concluded that the atoms were "physically" adsorbed rather than "chemically" adsorbed. Even though the mean adsorption energies were 77.4 and 80.7 kcal/mole for Sr and Ba, respectively, they were considerably larger than for most examples of chemisorption.

Azizov and Shope[57] obtained, using thermionic emission, work functions of clean tungsten and tungsten covered with barium. The curve of electron emission vs time of barium deposition is similar in shape to those obtained by Mayukha and others.[55] The work function of the covered specimen was 2.3 eV independent of the Miller indices of the substrate.

Schmidt[58] also studied barium on tungsten. He observed at high coverages (θ=0.8) the evidence of rearrangement of atoms on heating and the production of a work function minima on the close-packed planes. He also found that the barium atoms were electropositively adsorbed on tungsten, rather than chemisorbed.

Ovchinnikov and Tsarev[59] showed that the deposition of lithium on single-crystal points of tungsten and rhenium leads to a reduction in the work function of all the faces to 2.9±0.2 eV. A well defined minimum in the work function was observed on the (110) faces of tungsten and the (1011) faces of rhenium. When the film thickness was doubled, a second minimum was seen to appear at these faces. The adsorption energies at the optimum coating of tungsten and rhenium (that producing the lowest work function) were 2.25 and 2.15 eV, respectively.

Collins and Blott[60] studied, the work function of uranium on tungsten. Using field emission they observed three distinct adsorption states that corresponded to the uranium α, β and γ phases. The final work functions they found were 3.60±0.03 eV at 295°K, 3.53±0.03 eV in the range 934 to 1042°K and 3.43±0.03 eV above 1042°K. They also found a drop in the work function at 934°K and 1042°K and noticed the changes were irreversible under all conditions. Their work function vs deposition time also shows the minima encountered in previously discussed papers. In an earlier paper, Collins and Blott[61] reported a similar experiment with zirconium on tungsten. Among their results, it is important to notice the characteristic drop in work function below one monolayer of Zr and its subsequent increase

to a final steady value of pure Zr work function. Contaminated deposits showed a slower drop in work function and then a leveling off followed by a further drop. The zirconium work function attained was 3.84±0.03 eV.

Collins[62] also studied silicon adsorption on tungsten. He found the field emission work function of a monolayer deposited at 295°K to be 4.72±0.05 eV. In this case the work function increased from the average tungsten work function of 4.5 eV to a maxima of ~ 5.1 at 25 coverage (arbitrary units) dropping then to a 4.7 eV where it leveled off.

Most authors cited in this review considered that the work function maximum change happened when a monolayer of adsorbed atoms was completed, after which the work function tended to reach that of the bulk of the adsorbate. In the Collins experiment, then, 25 units are equivalent to $\theta=1$ (one monolayer).

Smith and Anderson[63] studied the epitaxial growth of Nickel on tungsten; however, they only described the process observed in field emission and field ionization but did not give measurements of the changes of work function or electron emission.

Anderson and Thompson[64] studied titanium on tungsten and rhenium using field electron emission. They determined, among other things, the work functions of α titanium and β titanium as 4.00±0.05 and 3.65±0.05 eV, respectively. Again the already classical plot of (ϕ,θ) work function versus coverage, showed a minima.

Jones[65] studied the adsorption of silver on tungsten using field emission microscopy. He considered the increase of work function produced by silver (4.7 eV) at coverages below a monolayer as the formation of silver-W dipoles. Accordingly, the decrease of ϕ at higher coverages to a value that is independent of coverage (as is also observed in other metals), would be due to the gradual establishment of a layer which is like that of bulk silver in its electronic structure. Contrary to Gretz and Pound they found that silver crystallites occur only when the coverage of silver is greater than eight monolayers.

Jones estimated 3.5 monolayers coverage for nucleation of crystallites of Ni on tungsten; this is the same estimate accepted by Smith.[63] Copper, crystallites form only when five or more monolayers are adsorbed. The very recent work of Polanski and Sidorski[66] discussed the adsorption of copper on tungsten. They found that the work function increases for low coverages on the (111) and (211) tungsten faces. After reaching a maximum value the changes of work function on these planes have the same character as on (110) and (100) planes, i.e. the work function drops down when the coverage increases, passes through a minimum and saturates for a thick layer. They connect the increase of work function on (111) and (211) faces at low coverage with the loose structure of the substrate. They claim that adsorption of copper on these planes causes smoothing of the crystal surface, and this can lead to enhancement of the work function. This is in agreement with Smoluchowski's model of surface potentials.

Polanski's calibration of coverage shows that changes in work function are occurring during the formation of the first layer of copper atoms. One way of explaining the work function enhancement observed by these authors is by considering the depolarization effect of the tungsten atoms on the first adatoms of copper that are adsorbed in the valleys of the (111) and (211) planes.

Janssen and Jones[67] recently published a paper in which they use the combined techniques of FEM and FIM to study Ge and Si condensed on W. They reported finding uniform monolayers of Ge giving a work function of 5.1 eV on top of which was a second monolayer with work function 4.8±0.05 eV, a value close to the work function of Ge. They also observed crystallites on top of the second layer and the growth of larger crystal aggregates proceeding at temperatures around 680°K or from linear clusters on the (110) planes of W.

Above 600°K the second layer did not form, and crystallites grew directly on the first layer. They found, also, regions of disorder between the crystallites and the tungsten surface. In addition, they found that Si alloys readily with W above 600°K and above a minimum coverage of four monolayers.

They could not ascertain the detailed structure of the alloy of Si and W but supposed it to be WSi_2.

Most of the previous experiments discuss the adhesion phenomena either in a descriptive fashion, utilizing the chemical model or using a model of polarization of the surface layer to explain work function changes. In summary, we could say that most of these authors agree that

1. A monolayer of atoms on a metal plane changes the work function of that plane.
2. The work function will increase or decrease depending on whether the adsorbed atoms are electropositive or electronegative with respect to the substrate.
3. After several monolayers have been deposited the work function is that of the adsorbed material.
4. The work function increment produced by one (or less than one) monolayer is due to the "smoothing" effect of the adsorbed atoms deposited on the valleys of high index planes.

At this point it is useful to bring up the theoretical prediction of Duke and Alferieff [1] that radically changed these concepts. Using an exactly solvable one-dimensional pseudopotential model, they calculated the field emission probability and current from a free-electron metal through both metallic and neutral adsorbates. The adsorbate potential is taken to be atomistic in nature (instead of the surface-charge model used in the previous articles).

They considered the adsorbed atom as an attractive square well plus a delta function core (no image modification) outside the surface of the metal (see Fig. 2b). Metallic adsorbates lead to the wide[1] resonances in the emission probability and additional peak or shoulder in the energy distributions, larger (10^2-10^4) enhancements in emission current and reductions in slope of the F-N plots at fields $F \sim 5\times10^7$ eV/cm. Neutral adsorbate potentials without bond states lead to reductions of both the emission probability and current and to a simple sealing

of the F-N energy distributions.

Plummer and Rhodin[68] made field emission measurements on a field evaporated (110) tungsten plane correlating their results with direct observation of the atomic configuration of the surface for different degrees of perfection. Depositing a single atom on the (110) plane they found that the adsorbed atom produced a significant increase in the field emitted current.

They also made a F-N plot for a clear (110) surface, a surface with one adatom and one with 20 adatoms. For higher surface coverages they could not accurately measure the atomic density using FIM because the adatoms would tend to stack in multiple layers. This resulted in an enhanced field which invalidated the application of the F-N analysis.

Similar experiments were done using the (112) and (111) planes. It was found that there was no change in the (112) field emission up to a few monolayers of W deposited and a decrease of emission from the (111) plane upon adsorption. These results led the authors to think that significant contributions from transmission resonance (as proposed by Duke and Alferieff) could be ruled out, but the experiments were consistent with the possibility that enhanced emission is caused by changes in the local field resulting from the presence of the adatom and not by a true change in work function.

Clark and Young[69] pursued the same problem but did so using measurements of current-voltage characteristics (F-N plots) with total energy distributions and depositing Sr on W.

They found, among other things, that the tunneling current from the region of about 30 atoms (of W) near the (111) plane increased by a factor of 3 to 5 times when the Si atom arrived, so that the emission "through" the adsorbed atom was about 100 times greater than the emission through the surface atoms.

If the classical dipolar model is adopted to interpret this experiment, we must first notice that Sr is an electropositive atom that decreases the work function. Also the atom protrudes from the surface increasing the electric field. Both factors would no doubt increase the electron emission. However, they also found that the F-N slope did not change with the adsorbed atom, nor with an increase of the slopes of the logarithmic total-energy distribution plots. These results cannot be explained with the classical model but are qualitatively explained by the Duke and Alferieff model.

The last three works discussed have been greatly ignored by most researchers that still resort to consider the emission changes with an adsorbate as changes in work function; and from the work function change, they resort to calculating the polarizability and dipolar moment of the adsorbed substances. There are justified reasons to doubt results obtained in this manner.

V. PURPOSE OF THIS STUDY

The previous chapters have introduced the concept of work function and some methods of measuring it (Chap. II).

The effect of adsorbed layers on a metal substrate has also been presented from the point of view of electron emission, and the dipolar model that has often been used to explain the changes of work function with an adsorbate has been described.

However, it has been clear that the idealizations used to establish the dipolar model, among others, are not easily obtained in real experimental situations when the adsorbate is evaporated on a substrate. Thus, there is an evident need to find a different method to ascertain the influence of atomic layers on the work function of metallic crystals.

The experiments conducted by this author were designed to study the work function changes produced by a monolayer of adsorbed atoms on a known crystallographic plane of a metal. The initial experiments were directed toward obtaining epitaxially grown monolayers on a tungsten surface, while the subsequent experiments utilized the layered structure presented by the superlattice planes of an ordered alloy. Such a structure can also be interpreted using the models developed for adsorption.

The ideal experimental situation to study polarization effects on the work function using the Gomer-Topping model requires, by looking at the formula:

$$\Delta\phi = \frac{2\pi n\, Mo\alpha}{(1+\alpha n^{3/2}k)} \qquad (V.1)$$

(a) A substrate with a known crystallographic orientation

(b) A method to ascertain the work function from different crystallographic planes

(c) An adsorbed monolayer with the adatoms on the same geometrical plane (or nearly so) so that the depolarization factor can be calculated

(d) Some way of independently knowing μ and a

(e) Some way of determining the distance between the substrate atoms and the adatoms

The ordered alloys (for example Ni_4Mo, Pt-Co, Ni_4W, etc.) have been thoroughly studied by X-ray and electron diffraction and, lately, by field ion microscopy. They have been shown to present a structure of layers of the same atomic species in certain directions. Using one of these alloys for the work function measurements could present a situation much closer to the one required by the dipolar model than the situation provided by the evaporation of atoms on a substrate.

The alloy monocrystal could be observed using field ion microscopy to ascertain a specific crystallographic orientation, where atomic monolayers could be evaporated and the electron emission measured. From the electron emission and the knowledge of the crystallography of the alloy, the other variables can be found. Then we propose to use ordered alloys for the study of work function changes produced by the surface atomic species.

It is evident that this process provides

(a) A known crystallographic orientation from FIM and thus knowledge of interplanar distances

(b) A known density of the uppermost layer of atoms and also its atomic packing

(c) The certainty that all the atoms in the top layer lie close to the same geometric plane and not in the "valleys and hills" of the substrate

(d) The additional availability of finding the effect of several layers of an atomic species on the electron emission (work function) of the other, by properly choosing the alloy for the experiment.

The present experiment is an attempt to determine if, based on the previous work already discussed, the electron emission pattern of Ni_4W can be predicted by considering the layered structure as having a similar behavior to the adsorbed layers of previous experiments. Ni_4W has been chosen for these experiments because of its crystallographic structure and the availability of pertinent information on this alloy.

The ordered phase of Ni_4W presents a layered structure of four layers between tungsten layers forming the superlattice planes and mixed layers of Ni and W in all the other planes (see Chap. VI.) Thus, orienting a Ni_4W specimen so that one of the well developed superlattice planes can be studied, it should be possible to ascertain changes of emission.

The most developed superlattice planes in field evaporated end forms of this alloy have been shown to be the (101) and ($\bar{1}$11) planes. Thus, an effort must be made to orient the crystal in one of these directions. Ni has a slightly lower electronegativity than tungsten (1.8 and 1.9 respectively) and W will tend to donate electrons to Ni. Hence, a layer of W should present a positively charged surface that will tend to lower the work function. From another approach, the average work function of W (4.5 eV) is lower than that of Ni (4.8 eV) and the tungsten monolayer should allow electrons to tunnel through it more easily than would allow electrons to tunnel through it more easily than would a top layer of Ni.

In conclusion, if field evaporation is used to uncover different layers of a superlattice pole, it can be expected that

(a) when the uppermost atomic layer is tungsten, the electron emission should increase to a maximum,

(b) The change of electron emission should be of about the same order of magnitude as that produced by a tungsten layer on a nickel substrate or vice versa.

(c) The polarizability can be easily established by calculating the density of the top layer.

(d) By measuring the work function at the different stages of field evaporation, the dipole moment can be calculated.

Because this area of research is very time consuming, this thesis will concentrate on the first stage of this endeavor-that is, ascertaining if there are perceivable changes in electron emission from the superlattice poles of ordered alloys after evaporation of a few monolayers.

For this purpose the simplest approach is to use a field emission method and scintillation technique as described in section IIIA.1. The following two chapters will give more detailed information about the alloy used and explain more specifically the techniques utilized to obtain the data.

VI. THE METALLURGY OF Ni_4W

Alloying nickel and tungsten was important to industry since it provided one of the earliest methods of making tungsten ductile. It has also been important as a basis for acid resistant alloys. The most recent nickel-tungsten phase diagram, by Ellinger and Sykes,[70] is reproduced in Fig. 4 with two modifications. The first one is the new intermetallic δ phase introduced by Walsh and Donachie[71] and the second is the widening of the β phase to be discussed later. From the melting point of nickel (at 1726±4°C) the liquidus curve rises to a maximum (1505°C) at 35% W, and then falls to 1495°C, the eutectic temperature. The alloy of eutectic composition contains 45% W. It was believed, by earlier investigators, that the maximum in the liquidus was associated with a compound, Ni_6W capable of existing in two dimorphic states - the β state, stable above 900°C and the α state stable only at lower temperatures. At the present time it is believed that Ni_6W does not exist and that the solid phase (α), separating from the liquid in hypoeutectic alloys, is a solid solution of tungsten in nickel. The limiting solubility at the eutectic temperature is at about 40% W decreasing to 38% at 970°C and to 32% at 800°C.

During an interdiffusion study of nickel-tungsten, Walsh and Donachie[71] reported the observation of a new phase (δ) that fits the formula NiW. This phase was present in diffusion couples annealed 100h at 1000°C and 112h at 1038°C but was not observed in couples annealed 60h at 1093°C or at temperatures up to 1316°C. Additional

anneal of 488h at 1038°C resulted in a slight thickening of the intermetallic phase layer. The δ phase seemed to be peritectically formed from the α and γ phases.

Using X-ray diffraction, the authors determined that the new phase (δ) was orthorhomic with a_o=7.76Å, b_o=12.48Å and c_o=7.10Å.

On cooling to 970°C, another peritectic reaction occurs between α and the tungsten-rich solid solution γ to give an intermediate phase, β, containing 43.93% W.[72] Due to the marked change in solid solubility with falling temperatures, alloys containing 32 to 45% W exhibit age hardening. Aging occurs very slowly at temperatures of the order of 600°C, but relatively quickly at about 900°C. Ni_4W has a range of solid solubility that can be estimated to 2 weight percent (3 at.%) at 900°C and it has been suggested to have a low tungsten boundary at 17.6% W or even lower, below 850°C.

After quenching the Ni_4W alloy anneal, two phases will be present. The tungsten rich (γ) phase appears as small inclusions evenly distributed in the nickel rich (α) matrix. Thus, in a FIM tip there is a much higher probability of imaging the α phase, and whenever we mention the as-quenched alloy we are actually referring to the α phase with 38% W content.

This phase has the same structure as nickel: it is fcc with a lattice parameter a_{fcc} = 3.6248. A slight contraction occurs upon ordering (below 970±10°C) and the new phase has a body centered tetragonal structure.

The unit cell of the β phase contains 8 Ni atoms and 2 tungsten atoms. The parameters for the bct lattice are a = 5.730 Å and c = 3.553 Å, c/a = 0.620. This makes the space group $c_{4m}^5 - I_4/m$. There are six possible crystallographic orientations of a given ordered domain with respect to the original fcc matrix. Two of these orientations are shown in Figs. 5a and 5b. The unit cell is rotated by an angle θ = 18.4° with respect to the fcc unit cell.

Tong and Washburn[73] proposed the matrix equation

$$A_o = \beta_{oi} P_1 A_i \qquad \text{(VI.1)}$$

to relate the vector $A_o = \begin{bmatrix} h \\ k \\ \ell \end{bmatrix}$ formed with the Miller indices based on the distorted fcc lattice and $A_i = \begin{bmatrix} H \\ K \\ L \end{bmatrix}$, the vector form with indices based the unit cell of the β phase.

$$P_1 = \frac{1}{5} \begin{bmatrix} 3 & 1 & 0 \\ -1 & 3 & 0 \\ 0 & 0 & 5 \end{bmatrix} \qquad \text{(VI.2)}$$

and

$$\beta_{o1} = \sqrt{(h^2+k^2+\ell^2)/(H^2+K^2)\ \frac{2}{5} + L^2} \qquad \text{(VI.3)}$$

According to Tong and Washburn[73] no regions of α phase were observed for the alloy aged at 850°C for 30 minutes. Thus the range of stability of the ordered β phase must extend at least as far as 38 Wt% on the low tungsten side. Epremian and Harker, in their x-ray defraction study of Ni_4W also found basis for a wider β phase. On this basis, the β^4 phase is widened in the phase diagram of Fig. 4.

From the geometry, it can be seen that the crystal can be constructed by alternating tungsten layers with four nickel layers parallel to the superlattice planes (Fig. 5); that is, the major planes of the lattice are formed by W atoms (bct). The fundamental planes of the distorted fcc structure [as (211) bct which corresponds to (111) fcc] are formed of layers of intermixed nickel and tungsten atoms (see Fig. 6).

Three dimensional models of Ni_4W β phase are shown in Figs. 8 to 11. The (011), (112) and (113) planes are obviously layered planes, as can be seen from the models. These planes tend to develop preferentially in field evaporation end forms of Ni_4Mo and Ni_4W and will be the center of this investigation. The resistance of nickel to corrosion by sulphuric acid is greatly increased by alloying with tungsten, an alloy containing 18% tungsten showing a minimum rate of solution, less than one fortieth the rate for pure nickel.

The tensile strength of nickel falls to a minimum at 24% tungsten, and then increases. By suitable heat treatment, a Brinell hardness of the order of 490 can be obtained in alloys containing 32-34% W. Also, there is a linear increase in the electrical resistivity up to 25% W. The nickel tungsten alloys might find industrial applications in the fabrication of jet turbines and any other instrumentation requiring high strength and high temperature metals.[72]

VII. EXPERIMENTAL PROCEDURE

A. Preparation of the Alloy

The nickel-tungsten alloy was prepared from an ingot of pure Ni (99.99%) and 0.218 W wires (99.99%), melted in an arc furnace with an excess of 1 atomic percent Ni to make up for evaporation. The produce of the melting was then swaged and homogenized at 1300°C in vacuum (10^{-7} Torr) for 90 hrs, three consecutive times. The alloy so produced was chemically tested and found to be 20 at.% W and 80 at.% Ni. Further swaging and annealing was required until wires of 0.011 in. diameter were obtained.

B. Heat Treatment

These wires were then annealed in a helium atmosphere at 1100±10°C for 144 hours and quenched into water. Two batched of wires were separated; those as-quenched and the second batch, annealed at 850° for 168 hours in an argon atmosphere.

C. Preparation of the Specimen

The actual tips for the field-ion microscope were made of pieces of the polycrystalline wires spot welded to a holder or mount. (See description of the equipment.) The wires were then electropolished until a diameter of 500 to 1000 Å was attained at the tip. The following two electropolishing procedures were used:

Procedure A

A polishing solution suggested by Nakamura[74] for tantalum composed of 4 parts 48% hydrofluoric acid, 2 parts concentrated sulfuric acid, 2 parts concentrated phosphoric acid, 1 part concentrated glacial acetic acid was used. This mixture was diluted with 75% in volume of pure water.

For the ordered material an initial potential of 32 volts dc was used until thinning was noticed. Then the tips were finished by slow electropolishing at 18 V giving short electric pulses of 0.1 sec or less until the desired tip diameter was obtained. If voltages lower than 18 volts were used, a nonconductive film was deposited on the tip. This film could be removed by etching in 1 N NaOH at 5 volts dc. Several metals were used as cathodes but tungsten, tantalum and stainless steel 304 were preferred.

For the as-quenched material, the initial voltage was about 12 volts. The final shaping was obtained with short pulses of 0.10 and 0.05 sec at a potential between 2 and 5 volts dc.

Procedure B

Electropolishing in 25% hydrochloric acid solution in water, was done using 10 volts ac for the initial thinning and 2 volts ac for the final shaping for both ordered and disordered tips. However after each immersion in the etching solution, it was found necessary to "clean" the tips from nonconductive films by electropolishing in 1N NaOH, with a short (1/5 sec) pulse at the same etching voltage. The NaOH does not attack the tip material appreciably, but long exposures to it will cause the

formation of an oxide film which is removable by electropolishing with the HCl solution. The final shape of the tip was always ascertained with an optical microscope at 500x magnification. Most of the tips had preferential etching along the shaft and care had to be put into the final shaping. Tips that had a relatively thick shaft and a thin-end point were preferred as they seemed to better withstand the high stresses produced during the field evaporation process.

The tips after electropolishing were washed in water and alcohol and mounted on the cryostat. The final preparation of the imaging surface was done through field evaporation in helium gas or in vacuum. A new electropolishing setup is included in the appendix.

D. Temperature Control

To produce the required range of temperatures for the experiment, a glass-metal cryostat was used and the specimens were cooled using low temperature helium gas transferred from a standard liquid helium container. A resistor in the helium container, electrically heated by a controlled ac source, provided the vapor pressure to force the liquid helium to transfer.

Currents of 1.2 ma were found sufficient to maintain enough flow of liquid helium toward the cold finger to maintain temperatures of 10 K at the tip holders (as ascertained with a thermocouple). Currents of 0.5 ma were enough for temperatures around the liquid nitrogen range. During operation these current readings and the characteristics of the image itself (resolution of single atoms) were taken as rough indicators for the specimen temperature.

E. The Equipment

The equipment used in this experiment was a versatile metal field-ion-field-emission microscope constructed from a basic design by Dr. H. C. Tong and adapted by the author for these experiments (Fig. 42) and a Jarrell-Ash recording microphotometer (Fig. 44).

After 6 hrs baking at 120°C and 10 hrs pumping time pressures as low as 1.5×10^{-10} Torr could easily be obtained and maintained in the apparatus, thus allowing for field emission observations. A glass-metal cryostat was utilized that allowed four specimens to be viewed during each run and also permitted high temperature flashing of the specimens (Fig. 43). An all metal orientable cryostat was also used in the final experiments (Fig. 46). A gas supply of neon and helium was readily available in the apparatus.

For the deposition of metals on the tungsten substrate an evaporator was constructed. The evaporator consisted of a filament of tungsten (0.05 in. in diameter) heated by a small D.C. current passing though it. The filament was shielded by a 1 in. in diameter stainless steel tube that was topped by a finger fitting cap with a hole at the center. In front of the cap there was attached a smaller cylinder containing a swinging gate made of 400 steel. Outside the shield two bars of 400 steel served to concentrate the externally applied magnetic field to make the gate swing open. The gate would close by its own weight. This arrangement permited the outgassing of the filament without contamination of the specimen and also it was possible to control, by opening and closing the gate, the amount

of metal atoms deposited on the substrate (see Fig. 45).

F. General Description of the Jarrell-Ash Recording Microphotometer

The basic microphotometer is a table instrument designed for a wide variety of spectrochemical, X-ray diffraction applications, or for use in any field where emulsion measurements must be made (see Fig. 44).

The microphotometer consists of a stage with transverse motion, a photographic plate holder with cross motion, an optical system with projecting line images, and an analytical slit with controls changing length, width, and transmission density. The stage is connected to a precision ball screw which can be operated manually or by a 12-speed reversible drive system. The plate holder, mounted on top of the stage, is moved laterally by a rack and pinion drive, using the operating knob on the front of the stage.

Density Range: 0 to 3.5 or better

Resolution: Two lines, 5 μ apart, resolved at transmission level of 50%

Sensitivity: 75 square μ, effective slit area for full scale clear plate deflections

Reproducibility: ± 1/2% over a 20% to 70% transmission range

Linearity: ± 3%

Scattered Light: Less than 1% full scale

Clear Plate Stability: ± 1% for valtages, 100 V to 120 V. (Disregard momentary deflections due to surges faster than 1/10 sec)

Clear Plate Drift: Less than ± 1% per 30 min after a 45 min warmup

Zero Drift: ± 1/2% of full scale over 30 min.

The slit used in the present experiment was 0.2 mm width and 0.1 mm length. The total probe area was 0.02 mm^2. Maximum transmission (100%) was set 20% above the 80% level set for background transmission (intensity of the screen beside the image). Our zero line coincides with the 80% mentioned above. Other details of the equipment used are included in the appendix.

VIII. EXPERIMENTAL RESULTS

In this chapter we shall report the experiments related to electron emission changes due to variations in composition of the surface monolayers in Ni_4W.

Three basically different sets of experiments were carried out. The first set utilized evaporation of different materials on tungsten following similar experiments described in previous chapters. The second and third set of experiments were done with the α (disordered) and β (ordered) phases of Ni_4W; field ion and field emission micrographs were taken and current intensity differences were measured. The changes of current intensity were measured using the scintillation method and the photometric technique described in Chapters III and IV. These methods proved to be adequate for our immediate purpose of comparing emission currents to determine the effect of the top layer of atoms on the current emission, and, thus, on the work function of a given crystallographic plane. Special care was taken in keeping the size of the emitting area much larger than the area of the photometric probe.

In order to account for the screen luminosity produced by reflection, x-ray excitation and other spurious effects, all the intensities were compared with the background intensity At the screen taken as 80 units. Several intensity measurements were made to decrease the probable error involved in using this method. Each set of measurements was made on micrographs taken with the same imaging voltage and the same exposure time.

A. Deposition of Materials on a W Substrate

The initial experiments using the already described instrumentation were made using tungsten as specimens. Tungsten has been the classical material observed in field ion and field emission microscopes because the specimens are easy to prepare and can withstand well the high stress produced by the imaging and evaporating fields. Therefore, there is more experimental data available on tungsten than on any other material. It is proper then to use tungsten as a control specimen to obtain information on the validity of the methods utilized, as the results can be easily interpreted by comparison with those obtained by previous authors.

The specimens were prepared by the usual method of electropolishing in 1% NaCl and field evaporating in the microscope under a helium atmosphere or in vacuum. The field ionization patterns of tungsten were taken at liquid nitrogen temperature and 6×10^{-4} Torr of helium.

We addressed ourselves to three basic questions. First, was it possible using FIM, to observe the formation of monolayer of a substance on a tungsten plane at low temperature? Second, could such a "monolayer" be considered parallel to the substrate or did it form a three dimensional structure? And, third, what was the validity of the current measurement method utilized?

The evaporation of tungsten and other metals on the tungsten substrate (FIM tip) was accomplished by the use of a specially designed evaporator (See Fig. 45). With this evaporator the flux and

total amount of deposited adatoms could be controlled by changing the current through the evaporating W wire and by opening and closing the outlet though which the adatoms could fly to the specimen. The outlet's gate, as explained in Ch. VIII, could be controlled magnetically from outside the vacuum chamber.

To start the operation, the tungsten specimen was field evaporated after a background pressure not larger than 2×10^{-9} Torr had been achieved. The equipment was thoroughly outgassed by backing for several hours. The evaporating wire was outgassed by heating to temperatures above 2000°C using an electric current though the wire.

While the specimen was field evaporated to the desired size and shape, the evaporating wire was heated again to evaporate the impurities that might have collected in the last minutes. The contaminations were continuously pumped out using a 6 lt/sec ion pump and a titanium sublimation pump. Then the specimen's voltage was lowered or completely shut off and the evaporator's gate opened. The amount of atoms deposited were continuously being observed by increasing the pressure and the imaging voltage until the specimen was imaged.

The temperature of the specimen was controlled by the flow of low temperature helium gas into the cryostat. The temperature of the specimen during deposition was varied from room temperature to 10 K. There were no observable differences between the arrangements of the adatoms deposited at the various substrate temperatures.

The evaporation of tungsten was tried initially using short deposition times (10 sec) at a substrate temperature of 10 K. In all cases observed the W adatoms tended to adhere to the high index planes and in a few cases on the close-packed planes. The adsorbed atoms showed an amorphous array and often one or more atoms of each group showed a brighter image than its neighbors. These brighter spots can be expected when an atom protrudes from the surface and therefore presents a higher ionizing field than its neighbors. Figure 12 shows six micrographs in which the same W specimen was used as a substrate.

For orientation purposes Fig. 12.3 was labeled with the Miller indexes of several planes. The atoms pointed to by arrow B on the (±10) pole do not show any preferential arrangement; and the uppermost atoms in this array look brighter than the rest, suggesting that they are more protruding than the others. To the right of this arrangement another arrow, marked with the letter A, shows a pseudomorphic arrangement of atoms in the (013) pole. These arrays are often found in the {013}, {112} and other loosely-packed planes of tungsten. The arrays could be easily confused with a pseudomorphic monolayer of adatoms; however, these experiments showed that they are partially evaporated monolayers of the substrate. The larger arrow marked by C in Fig. 12.1 shows a single atom adsorbed on the stepped (high index) area around the (011) pole. Careful observation of the area shows many other atoms adsorbed in equivalent sites. Figure 12.2 shows the same specimen after field evaporation. The atoms adsorbed on the (110)

pole were desorbed before desorption occurred in the stepped regions. The arrows in micrograph 2 show the clean areas of the (110) and (013) poles after further field evaporation.

The arrows identified by G in several of the micrographs indicate a grain boundary that is barely visible in the first micrograph but becomes more conspicuous in the second.

Notice also in Fig. 12.2 that the grain boundary is more extensive, as shown by the small arrows marked g. After further evaporation the grain boundary once more becomes less conspicuous (Fig. 12.3). This feature is not important for this discussion, but it does show qualitatively the amount of layers evaporated from that region before all the adatoms were removed. Also, it will be used for comparison of similar features in Ni_4W.

In the next sequence of micrographs (Figs. 12.4 to 12.6), a much larger amount of W atoms was deposited on the substrate ($\theta > 6$). It can be observed that the adatoms in Fig. 12.4 practically cover the specimen, except for the {011} planes which tend to follow the zone line decorations in their adsorption pattern. Again, no pseudomorphic monolayers or epitaxial crystal formation were observed. Subsequently the deposited layers were slowly field evaporated with the hope of removing the atoms in metastable energy states leaving the atoms that were more strongly bonded to the substrate. However, the last adatoms to be evaporated still showed amorphous arrangements.

Figure 12.5 shows a typical result of the slow field evaporation process where a disordered array still persists. A typical amorphous arrangement is marked by arrow D in micrographs 12.4 and 12.5. In the last micrograph (Fig. 12.6), the clean specimen is shown again after field evaporation of several layers. Few adsorbed atoms are still present in the loosely packed areas (the area indicated by arrow D).

The second series of experiments was aimed at depositing monolayers of Ni atoms. Again, the purpose was to deposit a group of Ni atoms on a crystal plane so that at least some of the atoms could be seen as forming a layer closely parallel to the substrate.

A similar process to the one described before was utilized. The nickel source was a tungsten wire with a nickel wire (99.999% Ni) wrapped around it. For these experiments, temperatures slightly above 800°C were enough to produee a flux of nickel atoms and safely avoid the evaporation of tungsten atoms that occurred at ~ 2000°C.

The Ni atoms are smaller than the tungsten atoms and have more probabilities of forming ordered arrays in the flat tungsten poles. Evaporation of a few Ni atoms on the substrate showed similar amorphous arrangements to those of the tungsten atoms. The (011) and (111) poles were rarely covered by adatoms and the {001} poles showed small concentrations of adatoms in disordered array. The sequence of micrographs in Fig. 13 record a typical experiment of nickel evaporation on a tungsten substrate. Again, the (001) plane (uppermost plane in Fig. 13.4) shows a geometrical atomic arrangement on a clean specimen.

It should also be noted that the (111) plane and surrounding areas offer well developed flat surfaces for adhesion. Evaporating Ni for 20 min (about 12 monolayers) leaves the specimen completely covered (Fig. 13.2) and the zone decorations barely visible. Slow field evaporation exposes the clean specimen (Fig. 13.3 to 13.6). Area A, shown by the arrow, appears dark in the first micrograph, devoid of protruding atoms. In the next micrograph (Fig. 13.2) the area is covered by bright dots (adsorbed atoms). It is especially interesting to note that the (111) plane is barely visible to the right of A and its symmetry is still apparent; thus, Ni atoms did not deposit on it. Figure 13.3 shows the specimen after several layers of deposited material have been evaporated. The (011) plane is still covered by adatoms and so is the (001) plane. The area A presents fewer atoms in Fig. 13.3. Further field evaporation renders the closest packed planes almost clean of adatoms, but the high index planes still present the bright points (see area A)(Fig. 13.4).

Increasing the voltage (Fig. 13.5) finally evaporates the last Ni atoms from the (011) and other relatively close-packed planes (appearing as circles) but leaves Ni atoms decorating the stepped high index probes (area A). Field evaporation of several layers from the (011) and (001) poles was necessary to completely desorb the nickel atoms from the loosely-packed areas of the tungsten substrate (Fig. 13.6).

Comparison of the field evaporation voltage necessary for desorption of W and Ni adatoms from a W substrate, revealed that relatively small increments of voltage (~1 kV) above the best imaging voltage were

necessary to evaporate W atoms from the (011) pole. However, the nickel atoms were more persistent and required ~2 kV above the imaging voltage to be desorbed from the (011) plane. This result cannot be assumed to be produced by bonding forces, as the (011) planes for different specimens presented different radii of curvature and only the field at that plane could be indicative of the bonding strength.

Summing up, it was not possible, within our experimental conditions, to develop a pseudomorphic monolayer of metallic atoms on tungsten substrates. It was necessary then to investigate further the possibilities of epitaxial deposition. Organic substances were also deposited on tungsten. As it it known that the surface diffusion coefficients were lower for these substances, it was expected that epitaxially grown layers would result. Alcohol and acetone were separately evaporated on the tungsten substrate. These substances have a very low melting point (178.3 K and 158.6 K, respectively); therefore, the evaporation of these substances required a different experimental arrangement. The alcohol and acetone were kept as solids in glass containers at liquid nitrogen temperature (78 K). The containers were thoroughly outgassed and valved off from the main chamber of the microscope by a needle valve. Once the specimen was developed, the temperature of one of the organic compounds was increased to room temperature for one or two minutes to allow a vapor pressure built up in the container. Subsequently, the bottom of the container was cooled down again and a small amount of gas was allowed to flow into the main chamber through

the needle valve and deposit on the cold specimen that was kept at ground potential. The cryostat where the specimen was mounted served as a cold trap for a large part of the residual organic vapor, and a sublimation pump was used to pump out the remaining vapor. Some depositions were made in the presence of helium imaging gas and some in vacuum; however, there were distinguishable differences between the two. By observing the FIM image, it was found that slight increments in the imaging voltage would produce outbursts of field evaporation of the organic molecules. Thus, the compounds showed a very small bonding energy to the substrate.

It can be observed, in Fig. 14.1, that the alcohol molecules completely cover the specimen; however, they avoided the (110) plane (center). Most of the adsorbed molecules concentrate around the {111} and {130} areas. The alcohol molecules were continuously field-evaporated even at low imaging voltage and substrate temperature of 10 K. It was not possible to evaporate slowly the admolecules and leave a visible monolayer adsorbed on the substrate. It can be observed in Fig. 14.2 that the adsorbed molecules seem to form a ring pattern that is not congruent with the ring pattern of the substrate. Also, some chains of bright dots can be observed in radial directions from the (110) pole.

The procedure used to deposite acetone molecules on the W substrate were similar to that used for alcohol. The acetone molecules tended to be adsorbed at the zone line decorations, enhancing the brightness of the decorations. Contrary to the behavior of metals and the behavior of

alcohol, acetone molecules deposited preferentially in the (110) plane of W seemed to avoid the stepped, loosely packed areas around the (110) plane. The lack of image points in these areas could also be interpreted as adsorption of the molecules in the steps and valleys, thus lowering the ionization probability of the stepped areas.

B. Electron Current Intensity Measurements from Pure Tungsten Specimens

The next series of experiments was aimed at determining the validity of using a scintillation-photometric technique to ascertain changes in electron emission.

Again the tungsten specimens were field evaporated and field emission micrographs taken. Figure 15.2 shows a field emission pattern wherein the (310), (011) and (111) planes are clearly visible. The FEM micrographs from a field evaporated specimen of W usually present a clear bilateral symmetry. As was explained in Chapter IV, the heat flashing method produces nearly spherical specimens while field evaporation produces nearly parabolical or nearly hyperbolical surfaces. This is a product of preferential field evaporation of certain planes due to the orientation dependent differences in bonding energies (see Ch. III). It can be observed in Fig. 15.2 that the (111) region presents a larger field emission image on the micrograph than does the $(11\bar{1})$ region; the {130} areas are nearly equal.

Azimuthal intensity measurements were made on these negatives, taking two directions of sweep with the microphotometer. One direction covered the {130} planes, and the other was perpendicular to that, covering the {111} planes.

It was important to find if the electron emission from a well developed plane was the same before and after evaporating an atomic monolayer. It must be remembered that the electron emission depends exponentially on the work function and the local field. Both quantities are assumed to remain constant for a given plane before and after field evaporation.

The average intensities $\bar{I}$ for the high emitting planes {111} and {130} are included in Table I, together with the variances (s), standard deviations σ, and probable error ε.

The standard deviation of 2.93 for an average intensity of 62.3 in the (111) plane is indicative of relatively large differences in the intensities measured. It was expected that the intensities measured from the same or equivalent planes would not change abruptly with slight field evaporation. The discrepancy between the individual intensities (see Table I) is probably produced by the contribution of the edge atoms to the measured emission.

The average size of the FEM image from the emitting area of the (111) poles is .03 mm^2 (on the negative) and the photometric probe hole has an area of 0.02 mm^2 (see Table II). Thus, any small changes of area in the emitting plane or changes of position of the probe hole could either include or exclude the edge atoms from one measurement to another, abruptly varying the measured intensity.

The experiments of Dyke and Dolan[75] showed similar discrepancies from azimuthal measurements made with a similar technique on a heat flashed tungsten specimen. Thus, there are differences in electron emission from crystallographically equivalent planes, using either

one of the methods (field evaporation or heat flashing) to shape the specimen. This differences must be taken into account for the interpretation of current measurements.

The curves in Fig. 16 show the intensity differences from one plane to another. Different curves were obtained after field evaporation of one tungsten monolayer; that is, after observing the shrinkage and disappearance of the innermost atomic ring of the {310} planes.

The highest intensities measured were from the {310} planes, and second to these intensities were those measured from the {111} planes. The lowest intensities were measured at the (112) and (110) planes (not included on the table).

The (130) planes had larger emitting areas (1.5 mm^2 on the micrograph) and did not show large variations of intensities from one measurement to another. The maximum standard deviation was 1.25 units. After field evaporation of one monolayer, there were discrepancies as large as two units between the $\bar{I}$ measured from the {111} and one unit in the $\bar{I}$ from the {130} (probable errors of ~ 2 and 1 respectively).

From the foregoing discussion, it can be concluded that the intensity measurements, using a scintillation technique with a microphotometer, can be adequately used for comparative intensity variations from field evaporated planes with emitting areas that can produce an image larger than 0.9 mm^2 on the original negative. Smaller emitting areas might produce spurious effects. Also, the technique cannot be used to ascertain work function differences from different planes in the same specimen because the measured currents from

equivalent planes of equal work function can differ as much as two intensity units.

Field evaporation of a few atomic layers from a well developed plane did not produce detectable changes in the local radius of curvature of a given plane.

Based on these results, the technique was applied to the study of electron emission from Ni_4W specimens.

C. Electron Current Intensity Measurements in Ni_4W α and β Phases

1. The α Phase (as-quenched from 1100°C)

The α phase was obtained after quenching the specimen from 1100°C (α + γ regions in the phase diagram). The specimens tended to have a (111) pole as a center axis (see Fig. 17.2). However, some specimens had a (100) orientation (see Fig. 17.4).

The field emission micrographs of the α phase showed a disordered structure with dark lines (high work function zones) propagating from the {111} plane to the {110} planes (Fig. 17.1). These dark lines differ from their counterparts in Ni, in which there are six dark lines propagating from the {111} to the {100} planes. Current intensity measurements made along the dark bands showed (Fig. 20) small variations in electron emission from nearly equivalent crystallographic directions measured in three different paths at about 120° from one another. The lowest emission was measured at the {111} planes and the highest at the {301} and {100} planes. From these measurements we could ascertain that the area of highest work function

appear to be the {111} planes.

The field ion micrographs of the α phase showed a disordered arrangement of atoms and three dark bands, corresponding in shape and direction to those observed in FEM. However, a complete discussion of the FIM characteristrics of the α phase is irrelevant to this paper and has been discussed elsewhere.[51]

Current intensities were also measured after field evaporation of one monolayer from the (111) plane (the only plane clearly visible in the α phase ionization micrographs). The results are shown in Fig. 21. The three sets of curves correspond to three directions of sweep with the microphotometer. It can be seen, from set a and set c, that the different crystallographic areas other than the (111) plane do not suffer major changes in current intensity after field evaporation of one or more atomic monolayers.

In this experiment the film utilized was either 35 mm or 70 mm Tri-X Kodak pancromatic film. The photographic image of the 6 inches in diameter glass window of the microscope measured 1.5 in. on the film; thus, the reduction factor of the emission and ionization images on the film was 1/4.

The size of the slit utilized for photometric measurements was 0.2 mm width by 0.1 mm length; thus, the efficient area was 0.02 mm^2. The average diameter of the images studied was 2 cm. The emitting areas of the planes under study varied greatly, and some of the areas are presented in Table II.for comparison with the probing area of the microphotometer. The area of the (111) plane of the α phase was

~ $0.02/mm^2$ on the average; hence, the edge atoms might have contributed to the measured emission.

2. The β Phase (Ordered)

The phase obtained after further annealing of the as-quenched alloy at 850°C showed a large degree of order in field ionization. (Figs. 36 and 41). It was observed that atoms at random positions formed islands between well ordered regions. These islands were probably remnants of α that had not yet transformed. Most of the atoms imaged in the β phase were probably tungsten, according to Tong and Washburn,[73] But nickel atoms were observed in some instances (see Fig. 32).

The Ni_4W ordered specimens proved to be fragile under the tension produced by the large electric fields, so few of the specimens would be developed enough to study their field emission patterns. To increase their life expectancy, few FIM pictures were taken, consequently shortening the exposure of the specimen to the high electric field.

About the first ten specimens observed were short-lived and did not develop to a large enough diameter through field evaporation to show any detectable symmetry in field ionization micrographs. The field emission pattern of these specimens also presented a random array of dark and bright areas corresponding to the high and low work function planes.

Several sequences of field emission micrographs were obtained which had been alternated with the field evaporation process. Some of them showed quite different intensities after approximately one monolayer had been evaporated from one of the prominent planes. The

micrograph in Fig. 22.1 was made after completing an appropriate field evaporation end form of an ordered specimen. Evaporating approximately one monolayer from the specimen, we obtained the emission pattern in Fig. 22.2. Subsequently, after evaporating two and three monolayers, the emission pattern in Figs. 22.3 and 22.4 were obtained. The arrows in the micrographs (A and B) show some areas where the variation of intensities is perceivable with the naked eye.

Other intensity fluctuations were measured with the microphotometer and are shown in Fig. 23. These intensity changes could be attributed to two factors. One would be the changes in chemical composition of the uppermost layer of atoms in some superlattice planes. This can affect the electron emission in a similar manner as adsorbed atoms do in pure metals; that is, the top layer affects the tunneling probability and the work function. Second, the variation of the emitting areas during the field evaporation process might abruptly change the local field. Either one of these effects can change the exponential of the F-N electron emission equation, producing large variations in current emission.

To discover which of these factors caused the intensity fluctuation, it was necessary to obtain better developed specimens, oriented in such a manner that one of the major superlattice planes could be large enough to produce an emission image much larger than the photometric probe.

Attempts in this direction proved exhausting due to specimen mortality; however, well developed specimens showing large (101) and (011) superlattice planes were finally developed and a more controlled process of observation and measurement was employed.

Field ionization observations of ten specimens were made but only five of them yielded usable data. The specimens were typically evaporated at liquid nitrogen temperature and observed at ~ 20 K in the field ionization mode. The voltage at the specimen was always increased a few volts at a time in order to evaporate a few of the clearly visible tungsten atoms from the (101) plane until a large enough emitting area (> 1 mm^2 on the micrograph) was obtained. Once this condition was reached, a field ionization picture was taken. The field was then slightly lowered (under the best imaging voltage), the temperature was increased to ~ 80 K as to evaporate residual He atoms from the surface, and the whole system was pumped out to the background pressure of 10^{-10} Torr. A field emission image was then obtained at ~ -1 kv and rapidly photographed to avoid contamination of the specimen.

Helium imaging gas was once again admitted into the chamber, after the negative voltage of field emission was turned off and the positive field was slowly increased to a voltage below the best imaging voltage. Consequently, it was found that no visible contamination was yet apparent in the field ion pattern and that the size of the imaging plane had not changed appreciably in area. A micrograph was sometimes taken at this stage.

After the best imaging voltage was restored and the temperatures of the specimen increased above 20 K, the removal of the next atomic layer was attempted. An increase of temperature to ~ 50 K was sometimes necessary so that a lower evaporating field could be used and the high stress produced on the specimen by the field could be diminished. To evaporate the nickel monolayers, we followed the process described by LeFevre[48] for Ni_4Mo. By slowly increasing the field and concentrating attention on the center of the superlattice plane, it was possible to distinguish the evaporation of each nickel monolayer.

The nickel atoms were only visible an instant before the uppermost nickel layer was completely evaporated. Thus, extreme care was put into observing the "flash" produced by the evaporation of a nickel monolayer before a FIM micrograph was taken and the cycle resumed--lowering the field, pumping out the imaging gas, changing to the negative voltage, and observing the field emission image as explained before. Later it was learned that the Ni monolayers could also be observed more clearly by increasing the pressure of the imaging gas.

There were several instances in which the Ni atoms were observed. Most commonly the atoms were observed between the tungsten atomic layers as shown in Fig. 32.1, when the imaging gas pressure was high enough (~ 10^{-3} Torr) to increase the probability of ionization of He atoms by the nickel atoms. Figure 32.2 shows a partially evaporated Ni layer on top of a tungsten layer. The atoms were imaged moments before the whole layer was evaporated. Other instances of Ni atoms imaged are shown in Fig. 32.3 and 32.4.

Thus the solute tungsten atoms are preferentially imaged in Ni_4W as in other dilute alloys, but the nickel atoms can be imaged only under certain conditions.

It was observed that only three nickel monolayers were field evaporated before the outer ring of the tungsten monolayer started to evaporate rapidly. A possible explanation for the missing layer is that two Ni layers evaporate simultaneously. This is especially probable for the Ni layers just above a tungsten layer, as will be shown in the next chapter.

In Fig. 24.1 a FIM pattern showing prominent (101) and (011) planes can be seen. Between these planes, the (112) plane appears fairly well developed. Less conspicuous are the (213) and (123) planes.

By carefully evaporating the (011) plane, we are able to observe, with the naked eye, image intensity variations after evaporation of one or two monolayers. (Fig. 24).

In order to avoid extraneous effects due to imaging conditions, care was taken to evaporate each monolayer in such a way that the next invisible (Ni) layer would have a diameter large enough so that its edge atoms would not influence the emission at the center of the plane and the emitting area would always be much larger than the photometric-probe slit. It was assumed that the invisible Ni monolayers would not change size abruptly until the uppermost plane was totally evaporated. This assumption was later validated (See Fig. 32) by imaging a Ni monolayer at higher He pressure. The sequence of field ion micrographs and field emission micrographs

on Figs. 25 to 29 shows the observed changes of intensity after field evaporation layer by layer.

As has previously been shown, the intensities measured can be correlated with the work functions by using the F-N equations but due to the many spurious effects encountered using the procedure previously outlined, only current ratios and work function differences and not absolute work functions were calculated.

The current ratios showed changes as large as 56% in the (011) plane after field evaporating three monolayers. Even larger changes were observed in the (123) and (213) planes; but due to the small emitting areas ($> .9\ mm^2$) these changes cannot necessarily be considered as being caused by changes in composition of the top atomic monolayer of the planes. The emitting area of the (123) planes was comparable in size to the microphotometer slit probe. Therefore, the outer ring of the emitting plane could have contributed to the current in some photographs, overriding the effect produced by the varying uppermost atomic layer.

The (101) plane was also observed and intensity measurements recorded, but no record was obtained of the approximate number of monolayers evaporated between emission micrographs.

The following paragraphs relate a sequence of intensity measurements performed on ordered specimens. In the (011) plane, the highest intensity measured was $78.5 \pm .26$ arbitrary units, corresponding to a well developed visible ring assumed to be tungsten. Evaporating that ring, another intensity measurement was made and the lowest emission

was found (51.2±6.5). This surface layer was assumed to be Ni.

The nickel layer was evaporated without major visible changes in the diameter of the next tungsten ring. The next intensity measured after this nickel layer was evaporated was much larger than the precious intensity (75.4±.70). Again, another nickel monolayer was evaporated and the intensity measured was 76.60±.40. Finally, nearly the original intensity was reached again (77.90±.54) when the last of the nickel monolayers was evaporated and the tungsten plane had started to evaporate more rapidly, thus completing the cycle. The cycle could be repeated until the tip broke off (flashed). These values are shown in Table IV and Fig. 30.

The current intensity from the (101) plane also varied cyclically but the values did not correspond to those measured from the (011) plane. As can be seen in Table V, the (101) intensity reached a lower minima than the (011) -- (34.6 compared to 51.2 from (011) plane.). Such a variation could be produced by differences in local radii of curvature (see Chap. III) between the planes.

The (112) plane also presented a cyclical change of intensities. As stated for the (101) plane, we could not ascertain the composition of the layer producing the observed emissions; however, the current minima measured from this plane was closer to the minima of the (011) (47.8 units). This agrees with the previous suposition that differences in curvature might produce the difference in current emission minima. It must also be remembered that the (121) plane is more loosely packed than the (011) plane, which could also account for the emission difference between the planes. The fact that the emission difference

is in the minima can be explained considering that we normalized the data for maximum emission (reference line 80). By doing so, the uppermost W plane that could cause the maxima would undoubtedly produce a different (higher) maxima in the (121) plane than in the (011) plane. As stated before, the only planes reported here whose emitting area was as small as the photometric probe area were the (123) and (213) planes. Depending on the orientation of the superlattice with respect to the original fcc lattice, the (213) plane is formed by layers of either Ni or W (see Fig. 10)(as the previously discussed planes) and the (123) is formed by mixed layers of Ni and W (see Fig. 11) or vice versa. It can then be expected that emission from these planes would differ due to the different atomic composition of the uppermost layer. However, even though the emission from these planes changed cyclically, the cycles coincided in intensity and phase (see Fig. 31).

As in the previous group of experiments, it could be claimed that the changes in electron emission intensity from the (011), (101) and (121) planes could be due either to changes in the local electric field or changes in the chemical composition of the uppermost layer. However, the size of the emitting area discards the possibility of contribution from the edge planes. Moreover, to distinguish between the two contributions, a series of micrographs was made in which emitting planes of different sizes were displayed together with their emission pattern. It can be observed that the emission pattern is independent of the plane size if the emitting area is larger than 0.9 mm^2 in diameter on the micrograph (30Å in diameter at the specimen).

A bright spot (Figs. 33.2 and 33.4) (representing high current emission) is produced by a larger emitting plane and a comparable bright spot is also produced by a small plane (Fig. 33.6). A dark spot (representing low current emission) can be observed in Fig. 34.2. It should be noted that it is produced by an emitting plane that is very small in diameter. Then, even when the local field is as high as can be expected in Fig. 34.1, the increment in work function produced by the Ni atoms overrides any field increment producing a low current emission.

For comparison, Fig. 34 shows dark spots produced by planes of different relative sizes. It can be concluded, then, that the emitting area does not strongly affect the current emission unless it is smaller than 30Å in diameter.

D. Summary of the Results of Electron Current Intensity Measurements

1. The intensity measurements performed on field evaporated tungsten specimens showed:

   a. The electron current from a given plane remains nearly constant when a few atomic layers are removed from that plane.
   b. The electron current emitted by two crystallographically equivalent planes is not necessarily the same for both planes.
   c. The intensity might be severely increased by the edge atoms of an emitting plane if their emission contributes to the measured intensity.

2. The intensity measured from the disordered α phase of Ni_4W shows the following characteristics:

a. Low emissivity of the (111) and (110) planes.

b. High emissivity of the (301) and (100) planes.

c. Low emissivity of the (100) zones.

3. When the disordered (α phase) specimens were field evaporated

a. There were no major changes in the current intensity emitted by the same crystallographic areas except the (111) plane which presented a very small emitting area.

b. The intensity changed observed in the (1$\bar{1}$1) plane could be attributed to the contribution to field emission produced by the edge atoms of the relatively small emitting surface.

4. The intensity measurements performed with ordered (β phase) specimens yielded the following major results:

a. The electron emission from equivalent crystallographic planes (i.e. {011}) showed differences that could not be attributed only to small geometrical differences (i.e. radial differences).

b. Field evaporation of monolayers from the same superlattice plane produced large intensity fluctuations in the field emission of that plane.

c. Careful measurements of intensities from the (011) plane showed that the intensities were repeated cyclically with every four atomic layers evaporated.

d. The highest intensities were measured when the tungsten monolayer was at the surface and the lowest when four nickel layers lay on top of the next W layer.

e. The intensity variations were shown to depend on the size of the emitting area if the area produced a FEM image smaller than 1 mm^2 on the photographic image.

f. The intensity variations were shown to have little dependence on the size of the field emission image if the planes were larger than 1 mm^2 on the photographic plate.

In conclusion, it was observed that there were relevant differences in the current intensities from some crystallographic planes of the ordered alloy (superlattice planes) after evaporation of one or more atomic layers and small local variations from different areas of the disordered alloy.

The next chapter will attempt to interpret these results using the models developed for emission changes with adhesion atoms and present a model for the results that cannot be explained by these models.

IX. DISCUSSION OF RESULTS

A. Deposition of Materials on a W Substrate

The field ion micrographs obtained from tungsten specimens with atoms of different materials adsorbed on their surface showed that the atoms tend to agglomerate in some crystallographic planes in arrangements that are not necessarily monolayers and more probably are three dimensional amorphous arrays of atoms.

At the low temperatures necessary for field ionization, the amorphous arrangement of atoms can be expected, because, as there is little or no surface diffusion at temperatures $\leqslant$ 78 K, the arriving atoms will be trapped wherever their kinetic energy is overcome by the attraction of surface atoms with free bonds.(i.e. in high index planes or by previously adsorbed atoms). Preadsorbed atoms seemed to form preferential sites for adsorption, especially in the low index planes. This can be observed in the (011) plane (Fig. 12.1).

The adsorbed atoms on close-packed surfaces present a larger number of free bonds than the surface atoms of the substrate under them, and the total surface free energy is decreased if the adsorbed atoms form small patches instead of being adsorbed at isolated sites. Once three or more atoms are adsorbed, the interatomic spaces between them often form preferential sites for further adsorption (or a valley as in the high index planes) and the "pyramidal" or three dimensional type of adhesion process observed in Fig. 12.3 results. The arrays produced by organic molecules are similar to those produced by metalsatoms even though they show different preferential sites for adsorption.

The three dimensional array produced either by the deposition of atoms or molecules in the valleys of the high index planes or by the stacking of atoms on "pyramids" on the lower index planes produces large changes in the local field as can be easily seen from the expression:

$$F = \frac{V}{Kr} \qquad \text{(IXA.1)}$$

where $K \simeq 5$ has been used for most experiments and others have calculated K from the general geometry of the specimen ($K \propto \ell n \frac{1}{r}$).
However, Kr for the "pile-up" of adatoms is not of the same value as that at other sites of the specimen. It is a much smaller quantity that cannot be ascertained because the shape of the pile-up is unknown. A Kr reduction (from $r \approx 1000$ Å for the tip to $r \simeq 5$ Å for the pile up) will increase exponentially the emission of electrons, giving a misleading contribution to the electron current.

From our experiments, as from the experiments of evaporation of metals on a tungsten substrate reviewed in Chapters XIII and IX, it seems improbable that the evaporation method could yield planar monolayers where the application of the Fowler and Nordheim equation (Eq. IID.3) and/or the dipolar interpretation of electron emission variation (Eq. IIB.7) could be justified.

B. Field Emission from Tungsten

The field emission pattern from tungsten showed a different emission from the (111) and $(11\bar{1})$ planes and the same electron emission from the {130} planes. From the Smoluchowski model for metal surfaces and F-N equation, it is expected that planes of equivalent crystallographic orientation should give the same electron current density. The factors influencing the electron current are (from Fowler-and Nordheim) in order of importance.

1. Work function
2. Local electric field
3. Applied voltage
4. Size of emitting area

Two planes of the same crystallographic family in a cubic crystal should have the same work function. The applied voltage should be the same for the two planes because measurements were made from the same specimen. The emitting area can be considered constant as it has a geometrical relation (by Thales theorem) to the fixed area of the photomicrometer probe slit; one is a geometric projection of the other.and the emitting area is nearly a flat plane. Therefore, the only variable that might be affecting electron emission differences

from the {111} planes is differences in the local field. Again the relation $F = V/Kr$ shows that, for a given voltage, differences in local radii of curvature can affect the local field and thus the electron emission which is exponentially dependent on the local field. The field evaporation process could have produced such a radial difference due to the original orientation of the specimen. Müller[39] has shown such local radii differences in field evaporated W specimens. If the field evaporated surface approaches a quadratic surface other than a spherical shell, then the apex of the curve could be oriented slightly off the (110)(center) plane and produce a larger local radius of curvature for the $(11\bar{1})$ than for the (111). This is a common effect in field evaporated surfaces. Because of this fact, work functions of pure metals are often measured from "heat flashed" surfaces that have a shape closer to the spherical shell. However, if measurements are made from the same plane after field evaporation, there is no variation in the emission of electrons from the same {111} or {130} planes.

The above results show that the method of measuring electron emission from field evaporated specimens can be used for the study of work function variations with field evaporation from the same crystallographic plane. If the evaporation of several monolayers from a pure metal did not produce measurable changes in the electron emission, then any changes in electron emission from a superlattice plane of an ordered alloy can be interpreted as being produced by changes of the surface dipolar moments affecting the work function of that plane, and therefore the electron emission. Differences

in emission from equivalent planes in the same crystal can be caused, as shown before, by differences in local radii of curvature for the various planes.

C. Electron Current Intensity Measurements of Ni_4W

1. The α Phase

The current intensity differences ascertained by measurements along three different directions 120° apart can be interpreted as being produced by work function differences from the various crystallographic planes with some contributions from the random distribution of solute atoms on the surface. Even though the three sweeps made by the microprobe are nearly equivalent, small differences in orientation of the areas swept and differences of local density of the alloying elements produced electron emission discrepancies.

Using the present technique, it is not possible to assume that the three areas covered by the microphotometer are exactly equivalent crystallographically. There are only general reference points on the micrograph (i.e. the (111) plane and high work function directions) for the direction of the sweep and not specific reference points as in tungsten (i.e. (011) and (111) poles). Moreover, by using a computer simulation of α specimens, it has been shown that there are differences in solute distribution at the surface.[51]

By counting bright spots that represent solute atoms in the simulated micrograph and an actual FIM picture of the α phase, it can be shown that there are areas of different density of bright spots (See Table VII). It is known from Gomer's experiments on Si^{37} dissolved in W, the electron emission will depend on the density of solute atoms appearing on the surface. Therefore, the small changes of the emission pattern can be accounted for by the local change of the surface potential. The surface potential is changed by the difference between the effective charge of the solute atoms and the charge of the solvent atoms at the surface (electronegativity of solute vs. solvent). The contribution of the two effects (crystallographic differences plus changes on the surface potential field) give rise to the local differences in electron emission.

The abrupt variation of emission of the (111) plane produced by field evaporation of a few monolayers could be explained in a similar manner as the randon variation in the (011) plane of tungsten. In the α specimen, the (111) plane emitting area produced a smaller image than the photometric probe used Table II. Therefore, we measured contributions from the distorted field at the edges of the uppermost layer of atoms which tended to increase the emission by increasing the local field. This effect overshadows the dependence of the current on the work function of the (111) plane.

2. The β Phase (ordered phase)

The amorphous dark bands of the β phase mentioned in Chapter VIII will be discussed in more detail in the next chapter. We shall, however, continue with the discussion of the results of the current emission measurements in this chapter.

The intensity measurements obtained in our experiments have cyclic values with respect to evaporation of monolayers, showing a minimum value when the tungsten monolayer is evaporated. The ϕ values have the opposite behavior, as (from the F-N equation) the maxima of the work function coincides with the minima of the intensity. The data obtained, however, showed that only three Ni layers could be observed field evaporating between tungsten monolayers. To understand better the process of field evaporation, a schematic representation of a low index plane of a pure metal is shown in Fig. 7a.

The evaporation process is shown to start at the edge of the uppermost layer and once some atoms have been removed from it a few edge atoms of the next layer start to evaporate (left side of picture). However, fast evaporation of the second layer will not start until the uppermost layer is fully evaporated.

According to Muller's[76] interpretation of Bardin's model for alloys, "as field evaporation proceeds the solvent atoms just above the solute atoms will evaporate preferentially." This process is schematically shown in Fig. 7c. Open circles represent the solvent atoms and cross-hatched circles the solute atoms. Therefore, in Ni_4W,

Ni atoms which lie just above tungsten atoms will be preferentially evaporated. The process for a superlattice plane is simulated in Fig. 7b where the uppermost layer of Ni atoms (open circles) is been evaporated, exposing the underlying Ni layer that is just above a W layer. It can be expected that due to the lower sublimation energy of the second nickel layer, it will evaporate almost simultaneously with the first layer.

This effect can account for the "missing layer" observed in the field evaporation process of the (011) plane. The last two nickel layers could have evaporated almost simultaneously; thus, the experimenter could only observe the evaporation of three nickel layers.

The current emission measurements made from the (011) planes of the β phase presented two important characteristics. First, there was a marked difference of emission when a tungsten layer lay at the surface of the plane and when a nickel layer was exposed to the surface. Second, there was a difference of emission when the nickel monolayers were removed through field evaporation.

The first observed difference can be explained on the basis of the dipolar model presented by Gomer, if we consider the layered (011) plane similar to a Ni cyystal with a W monolayer adsorbed on its surface. However, the difference in emission currents after evaporating successive Ni monolayers falls outside the assumptions for this model.

a. The dipolar model interpretation of intensity variations. The field evaporation of atomic monolayers from the (011) plane of Ni_4W β phase can be considered as an inverse process to the adsorption of atomic monolayers on a metal substrate. The four nickel layers could be interpreted as forming a small crystal. When a tungsten monolayer of the (011) plane is brought to the surface by field evaporation, it can be considered as an adsorbed layer on a low index plane of the nickel "crystal." The changes of electron emission with the evaporation of the tungsten monolayer are qualitatively comparable to the changes produced by a tungsten ad-layer on a nickel substrate.

Using the Gomer-Topping model, the variation of work function produced by the evaporation of a tungsten monolayer can be expressed as

$$\Delta\phi = \frac{2\pi \mu_o n}{1 + 9 n_{max}^{3/2} \alpha} \qquad \text{(IXC.3)}$$

where n_{max} refers to the density of surface dipoles when the W layer completely covers the emitting surface. The expected work function change $\Delta\phi$ can be directly found from the geometry of the system. The polarizability is given by the following:

$$\alpha = 0.221\, n_{max}^{3/2} \qquad \text{(IXC.4)}$$

The (011) plane has a surface area of 38.2 $Å^2$ (per unit lattice) containing two surface atoms. Then 5.24×10^{-2} atom/$Å^2$ = 5.24×10^{14} at/cm^2.

The polarizability is then

$$\alpha = 18.71 \pm 0.02 \text{ Å}^3 \qquad \text{(IXC.5)}$$

μ_o is the dipolar moment of a tungsten atom, partially ionized, and its image charge, $n=n_{max}$, is the density of tungsten atoms on the (011) surface. The dipolar moment μ_o can be calculated from first principles if we consider that the tungsten atoms are single ionized. Then Z=1 and q=e (the electron charge).

The field penetration gives a value for $2d_o \simeq 0.5$ Å

$$\mu_o = 1.6 \times 10^{-27} \text{ coul-cm} \qquad \text{(IXC.6)}$$

Introducing the results in Eqs. (IXC.5) and (IXC.6) into Eq. (IXC.3) we obtain

$$\Delta\phi = 0.83 \text{ eV} \qquad \text{(IXC.7)}$$

$\Delta\phi$ is the expected work function change due to the removal of the tungsten monolayer from the (011) plane. This value of $\Delta\phi$ is comparable in order of magnitude to the difference between the average work functions of pure tungsten (4.5 eV) and pure nickel (4.8 eV), $\phi_{Ni}-\phi_W = 0.3$ eV.

b. The F-N Approach to the Intensity Variations. From the ratios of intensities measured from the (011) plane of Ni_4W and tabulated in Table VI, the actual change of work function can be calculated using the F-N equation. Writing the equation in a simplified form

$$\ln \frac{I}{V^2} = \ln A - b \frac{\phi^{3/2}}{V} \qquad \text{(IXC.9)}$$

where b is a constant given by 0.68/c (see Sec. IXC.)

$$\mathrm{d}V = E \qquad \text{(IXC.10)}$$

The current ratios for the same imaging voltage yield

$$\ln \frac{I}{I_o} = - b \frac{(\phi^{3/2} - \phi_o^{3/2})}{V} \qquad \text{(IXC.11)}$$

$$\ln \frac{I}{I_o} = - 68 \frac{(\phi^{3/2} - \phi_o^{3/2})}{E} \qquad \text{(IXC.12)}$$

In order to find $\Delta\phi$ from the current ratio, we must find an algebraic correlation between $\phi^{3/2} - \phi_o^{3/2}$ and $\Delta\phi$. This can be done by using the expansions:

$$\phi^x = 1 + x \ln\phi + \frac{(x \ln\phi)^2}{2!} + \frac{(x \ln\phi)^3}{3!} + \ldots \qquad \text{(IXC.13)}$$

and

$$\ln\phi = \frac{\phi-1}{\phi} + \frac{1}{2} \frac{(\phi-1)^2}{\phi} + \frac{1}{3} \left(\frac{\phi-1}{\phi}\right)^3 + \ldots \qquad \text{(IXC.14)}$$

For a small $\Delta\phi$, the relation (to a first approximation) can be written as:

$$\phi^{3/2} - \phi_o^{3/2} \approx \frac{3}{2}\left[\frac{(\phi-1)}{\phi} - \frac{(\phi_o-1)}{\phi_o}\right] \qquad \text{(IXC.15)}$$

then

$$\phi^{3/2} - \phi_o^{3/2} \simeq \frac{3}{2}\left[\frac{\Delta\phi}{\phi\phi_o}\right] \qquad \text{(IXC.16)}$$

Using this last expression in Eq. (IXC.12), we get

$$\ln \frac{I}{I_o} \approx -1.02 \frac{\Delta\phi}{\phi\phi_o E} \qquad \text{(IXC.17)}$$

It was shown that the (011) plane of Ni_4W is loosely packed. Therefore, the work functions for the electron emission from the (011) plane of Ni_4W (ϕ and ϕ_o) should be lower than the average work functions of pure Ni and W. Then, it would be reasonable to assume that the product of the average work functions of Ni and W ($\phi_{Ni}\ \phi_W$) is higher than $\phi\phi_o$ and it could be used as a first approximation for the purpose of finding $\Delta\phi$.

$$\phi\phi_o < \phi_{Ni}\ \phi_W = 21.6\ (eV)^2 \qquad \text{(IXC.18)}$$

Then an expression for $\Delta\phi$ can be written as

$$\Delta\phi = -\frac{21.6}{1.02} E \ln \frac{I}{I_o} \qquad \text{(IXC.19)}$$

The average electric field at the (011) plane is probably not less than 0.2 V/Å or higher than 0.6 V/Å and so a value of 0.5 V/Å is adequate for E.

$$\Delta\phi = - 10.6 \ln \frac{I}{I_o} \qquad \text{(IXC.20)}$$

Removing the tungsten substrate from the nickel "crystal" reduces the current from 78.50 to 51.20 (arbitrary units)(see Table VI) I=0.65. Hence, $\ln I/I_o = - 0.4277$ and

$$\Delta\phi = 4.51 \text{ eV} \qquad \text{(IXC.21)}$$

Thus, the required work function change to produce the electron current ratio of 0.65 observed after removing the tungsten monolayer is much larger than the expected change due to a dipolar monolayer at the surface ($\Delta\phi$ = 0.83 eV). The current increment of 1.5 times produced by the W monolayer on the Ni "crystal" may be produced by contributions from transmission resonance at the potential wells which in turn are produced by the tungsten atoms, as Duke and Alferieff proposed in their model.[1]

The effect of the W atoms on the external field should be nearly the same as that of the Ni atoms because the surface density is the same for both species in the (011) plane. Therefore, the enhancement effect produced on the current by the tungsten atoms at the surface seems to be related to the difference in tunneling probability between the electrons tunneling out through the tungsten atoms and

those tunneling through the nickel atoms. Tt is interesting to notice that the removal of the last two monolayers of nickel before the next tungsten layer is reached produce a change in electron current given by the ratio $I_4/I_5 = 0.98$ and the logarithm -0.01971. Then, using the expression IXC.20, we get

$$\Delta\phi = 0.186 \text{ eV} \qquad \text{(IXC.22)}$$

If we consider the substrate to end at the tungsten monolayer (inclusive), and the two nickel layers can be thought as adsorbed layers, their effect on the electron emission is comparable to that expected from a dipolar layer at the surface (Eq. XXC.7). Therefore, two layers of Ni seem to produce an actual change of work function at the surface. There is no evidence of field enhancement and tunneling resonance in this case. Not having the data pertaining to the work function changes of Ni on W, we must use the available data on Cu. Using Polanski and Sidorski's[66] data, we might be able to calculate the effect that three monolayers of copper would have on the work function of a substrate and then compare the results with the data obtained from Ni_4W.

The element copper is next to nickel in the periodic table and expected to behave chemically in the same manner as nickel. It follows that the dipolar moment is probably of similar value, and its influence on the work function of a substrate should be within the same order of magnitude.

To avoid field enhancement effects, let us consider the work function change that occurs when two or more monolayers of copper are deposited on the already "smooth" tungsten surface; that is to say, the change introduced after obtaining $\phi_{min} = \phi_o = 4.2$ (2 monolayers). The Fowler and Nordheim equation can be written as

$$I/V^2 = a \exp -b\, \phi^{3/2}/V \qquad \text{(IXC.23)}$$

where

$$b = 6.8\times10^{-7}\, \alpha \frac{Kr}{V} \qquad \text{(IXC.24)}$$

$$\alpha = (1-y)^{1/2} \qquad \text{(IXC.25)}$$

and using Gomer's tabulation for y:[5]

$$\bar{y} = 0.275 \qquad \text{(IXC.26)}$$

then

$$\alpha = 0.8514 \quad . \qquad \text{(IXC.27)}$$

k depends on the geometry of the system.

Using a paraboloid of revolution to simulate the shape of the emitter

$$k_1 = \frac{1}{2} \ell n(x/r) \qquad \text{(IXC.28)}$$

For a hyperboloid

$$k_2 = \frac{1}{2} \ell n(4x/r) \qquad \text{(IXC.29)}$$

x(cm) is the emitter to screen distance and r(cm) is the specimen radius.

For our system $x = 7.5$ cm (IXC.30)

and for the experiment under discussion

$$r \approx 1000 \text{ Å} \qquad \text{(IXC.31)}$$

Then using Eq. (IXC.28) and (IXC.29)

$$k_1 = 6.76 \qquad \text{(IXC.32)}$$

and

$$k_2 = 7.45 \qquad \text{(IXC.33)}$$

$$\phi_o^{3/2} = 4.2^{3/2} = 8.607 \qquad \text{(IXC.34)}$$

For six layers of Cu on a W substrate (from Polanski's data).[66]

$$\phi^{3/2} = 4.3^{3/2} = 8.916 \qquad \text{(IXC.35)}$$

$$\phi^{3/2} - \phi_o^{3/2} = + 0.309 \qquad \text{(IXC.36)}$$

For an order of magnitude approximation as

$$kr/V = F \approx 10^7 \quad \text{and} \quad \alpha = 0.85 \approx 1 \tag{IXC.37}$$

$$I/I_o = \exp - (\phi^{3/2} - \phi_o^{3/2}) \times 6.8 \tag{IXC.38}$$

Taking

$$b \approx 1 \tag{IXC.39}$$

$$I/I_o = \exp - 2.103 \tag{IXC.40}$$

$$I/I_o = 0.12 \tag{IXC.41}$$

for five monolayers of Cu on the smooth W/Cu surface. This ratio is of the same order of magnitude than the ratios shown in Table VI, between the currents through Ni layers and those through an uppermost W layer.

The work function changes observed by Polanski, after "smoothing" had taken place, were not of the some order of magnitude as the work function change produced by a single tungsten layer on the nickel "crystal". However, the large change produced by the "smoothing" process of Cu is closer in value to the one observed after removal of a W monolayer from the (011) plane of Ni_4W.

c. <u>The Application of the Dipolar Model for Changes Produced by the Evaporation of Ni Layers from the (011) Plane of Ni_4W β Phase</u>. The F-N equation provides an order of magnitude estimate of the work function variations that could be expected to produce the measured intensities. It is not clear, however, if the dipolar model can be used to justify these variations.

In the following pages, we shall discuss the applicability of the model to changes produced by the desorption of one or more monolayers. In the dipolar model only the top atomic layer is considered, and the measured effect seems to show that other layers are affecting the field emission process. The dipolar model is based on the often accepted model of surface space charge. The surface space charge model can be summarized as follows:

Any accumulation or depletion of charge carriers in a surface with respect to the bulk carrier concentration establishes a static space-charge region near the surface. An external electric field applied to the surface or an adsorbed monolayer of charged particles (ions or polarized atoms or molecules) can produce such a space-charge. The height of the surface potential barrier V and the penetration distance into the bulk depend on the concentration of mobile charge carriers in the surface region.

If N is the electron concentration on the surface and produces an image charge of equal density at the bulk, then the potential produced at any point by these charges is only a function of the distance x of the charge from the surface. It can be found, by using the Poisson equation,[77] that

$$\frac{d^2V}{dx^2} = \frac{eN}{\varepsilon\varepsilon_o} \qquad \text{(IXC.42)}$$

where ε is the dielectric constant of the metal and ε_o is the permittivity of free space. Integrating twice we get

$$V(x) = \frac{eN(x-d)^2}{2\varepsilon\varepsilon_o} \qquad \text{(IXC.43)}$$

Notice that at x=d V(x=d)=0. Thus d is the distance at which the electrostatic potential, due to the charge distribution at the surface, becomes zero and the electron concentration attains its bulk value again.

The height of the space-charge potential at the surface is given by

$$V_o = \frac{eNd^2}{2\varepsilon\varepsilon_o} \qquad \text{(IXC.44)}$$

As the density of charges at the surface is equal to the density of image charges

$$d \approx \left[\frac{2\varepsilon\varepsilon_o}{eN} V\right]^{1/2} \qquad \text{(IXC.45)}$$

The charges concentrated in the surface produce images on the bulk at a distance 2x from them. Then, approximating the charge density by the bulk electron concentration and using typical values of the surface barrier and of the permittivity (ε), we can notice that for electron concentrations of 10^{-7} cm^{-3} or larger the space charge is restricted to distances on the order of one atomic layer or less. This is due to the fact that the large free carrier density screens the solid from the penetration of the electrostatic field which is caused by the charge imbalance.

For most metals almost every atom contributes one free valence electron to the carriers. Since the atomic density for most solids is of the order of 10^{22} cm^{-3}, d could be of the order of .5 Å or less. Müller[39] uses the Thomas-Fermi approximation, in which the electric field decays exponentially with its distance from the metal surface. That approximation is expressed as

$$F = F_o \exp - \left(\frac{|x|}{\delta}\right) \qquad \text{(IXC.46)}$$

with the penetration depth given by

$$\delta = \frac{1}{2} (a_o d)^{1/2} \qquad \text{(IXC.47)}$$

where a_o = 0.53 Å is the Bohr radius and d is the dimension of the unit surface cell containing one electron. For a unit cell of size 3 Å, δ=0.63 Å, which is approximately equal to the quantity obtained using the Poisson equation (δ=0.5 Å).

On less densely packed surfaces, the local geometry is simply described by an average atomic spacing s. It is thought that one electron is spread over the volume $s^2 d$ of the surface unit cell, so that

$$\delta = \frac{1}{2} a_o^{1/2} (s^2 d)^{1/2} \qquad \text{(IXC.48)}$$

The {011} planes of Ni_4W are very loosely packed; thus Eq. IXC.48 should be applied for field penetration.

From the geometry $s \simeq a$

$$\simeq 5.70 \text{ Å} \qquad \text{(IXC.49)}$$

and

$$d_{(011)} = 0.672 \qquad \text{(IXC.50)}$$

then

$$\delta = \frac{1}{2} (0.53)^{1/2} (5.7^2 \times 0.672)^{1/6} = .635$$

The field penetration δ=.635 is still less than the interplanar distance (.953). Using this model, only the first layer of atoms should contribute to emission because it is the only layer affected by the external field as to be polarized. Thus, according to the surface space charge model, the electron moving toward the surface finds a bulk distribution of charges until it reaches the surface.

If the surface is defined as the locus plane for the atoms in the uppermost layer, then, as we said before, there should not be perceptible variations of emission due to removal of different Ni monolayers until the W layer is reached. Two nickel monolayers should not differ in their effect on emission if the emission only depends (as assumed by this model) on the packing surface dipolar moments and therefore electronegativity of the surface layer. The current variation with field evaporation of Ni layers cannot be explained using this simple model. It is important, them, to summarize these findings in a simple model for field emission from superlattice planes of ordered alloys that could also be applied to some adsorption phenomena.

d. A Simple Model to Interpret the Variation of Electron Emission from Superlattice Planes of Ni_4W β Phase. To return to the two models more often used to explain electron current charges due to adsorption, the surface dipoles model[9] and the resonance model[1] both accept the Summerfeld free-electron model for the metal. Consequently, the surface field only penetrates to the uppermost atomic layer (~ .5 Å).

However, our experiments show that the electron emission varies for different nickel layers having the same crystallographic orientation and therefore having identical surface packing. This effect suggests the influence of atomic layers within the bulk on the electron emission (i.e. the proximity of the W monolayer to the surface). Hence, the obvious path toward the interpretation of this effect is to redefine the surface or adopt an atomistic model instead of a model based on a continuously charged surface layer. The (110), (101) and (121) planes cannot be represented as a smooth plane surface but instead as a open surface where the atoms of at least four subsequent layers under the uppermost layer contribute directly to electron emission. Figure 35d shows a section of the (110) plane in which four (cross-hatched) layers are of Ni atoms and the fifth layer from the surface is of W atoms (open circles). The "size" of the atoms are drawn to scale with respect to atomic distances.

It should be noted that in Fig. 35d the underlying W layer is completely covered by the fourth Ni layer. This would correspond to the intensity current of 51.20 reported in the previous chapter.

Removal of the uppermost Ni layer leaves more than 50% of the underlying tungsten monolayer exposed (Fig. 35c). This corresponds with the current of 75.40 reported previously. Subsequent removal of Ni monolayers does not drastically expose the tungsten "substrate" (Fig. 35b the next current measured was 76.60). It can then be assumed that most of the electron current tunnels through the tungsten atoms. Covering the W atoms with Ni atoms diminished drastically the current. Then, exposure of the W atoms, even if it lies three layers under the surface, increases the current intensity by 47%. The emissivity of the tungsten monolayer does not seem substantially diminished by its distance from the surface, i.e. under three nickel layers. Thus, the field does not seem to vary exponentially from the uppermost layer, as expected from the Fermi-Thomas model. The electron current dependence on the work function and the electric field can be expressed as

$$j \propto \exp - \zeta \qquad \text{(IXC.53)}$$

where

$$\zeta = \sum_{i=0}^{n} - \left(\frac{\phi_{Ni}^{3/2}}{F_{Ni}}\right)_i + \left(\frac{\phi_W^{3/2}}{(F_W)}\right) \qquad \text{(IXC.54)}$$

where ϕ_W and F_W are the work functions and field of the W monolayer, respectively. F_W will vary inversely with the number of Ni layers above it. ϕ_{Ni} and F_{Ni} are the work function and field of the i^{th} nickel layer. N is the total number of Ni layers above the next W monolayer. Using the above expression we can interpret the

experimental results. The tunneling probability D(W) for the electrons, through atoms at the surface will be higher than for those below the surface. This can be seen from Eq. (IIC.16) which can be simplified as

$$D(W) = e^{-bW^{3/2}/F_i} \qquad \text{(IXC.55)}$$

where b is a quasi constant, W is the energy of the tunneling electron, and F_i is the external field on the i^{th} layer of atoms. The more superficial a layer lies, the higher is the electric field acting on it.

Because the work function of W is lower than that of Ni, the work function dependence of the current (as expressed in Eq. (IIIC.25)) would make the current through the tungsten atoms the most important contribution to the electron emission. Accordingly, when the W layer lies on the surface, most of the current measured is contributed by electrons tunneling through its atoms.

The four Ni layers will have a decreasing deformation of their electron potential barrier due to a smaller field F_{Ni} and that contributes proportionally less. Also because of the W atoms' lower ionization potential, they act as a positive charge and are a preferential path for the outgoing electrons. Once the tungsten monolayer is evaporated, (Fig. 35d), a nickel monolayer is at the surface. The next W monolayer will lie four layers deep. The electronegativity of W atoms (1.9) still makes them preferential paths for electrons. They contribute less, however, because the W atoms have a small field deformation of their potential and the tunneling

probability decreases when they are lying under Ni atoms that almost totally cover them (Fig. 36d).

The Ni atoms have the effect contrary to that of the W atoms on the current emission. Their electronegativity is lower (1.8) and they do not contribute with a net positive charge to the surface that is as high as that produced by W. However, the field deformation of the electric potential is larger and the tunneling probability through them increases. Nevertheless, their overall contribution is less than that of tungsten at a top monolayer. Further evaporation puts the W layer in the third layer below the surface. Obviously the electron electric potential barrier will now be narrower and the tunneling probability through it is increased. When the W monolayer is the third layer from the surface the total contribution of the W and Ni atoms is much closer to that of total contribution given by the W atoms at the surface. The largest difference results when the W monolayer lies under four layers of Ni and the field F_W is almost completely screened by the Ni atoms.

Most investigators point out that the electron emission depends on the number of layers deposited on the substrate. For example, Jones[65] observed that during the deposition of silver atoms on a tungsten substrate several layers were required (θ=5) before the current emission became independent of coverage. Larger coverages ($\theta > 7$) were needed for copper and gold. These results cannot be explained by the dipolar model because, again, the emission should depend on the dipolar moment of the uppermost layer, and two layers

of equal density and the same atomic species should present the same dipolar moment. Once the surface of the substrate is covered with adatoms, there should not be any further change in the electron emission caused by the dipolar moment (formed by the charged adatoms and their image on the substrate). However, as we said before, this is not true: the electron emission keeps "feeling the substrate" until several layers are deposited and then the current emission reaches a constant value that has been equated with the work function of the adsorbate. This effect can be better explained by the use of our simple model wherein the emission through one of the layers is the main contribution to the total emission current.

D. Summary and Conclusions

The experiments presented in this thesis were designed to study the effects of the uppermost layer of atoms on the electron emission current from a metal plane using a field emission-field ion microscope. The initial experiments were directed toward obtaining atomic monolayers of tungsten, nickel, alcohol, and acetone nearly parallel to a crystallographic plane of a tungsten field evaporated specimen which was imaged at 10 K with helium imaging gas. These attempts proved fruitless as it was not possible, within our experimental conditions, to develop a pseudomorphic monolayer of either metallic or organic adparticles. Instead, amorphous three dimensional arrays of adparticles were often observed. Considering these results and observing the results reported by others, this author believes that the use of the

dipolar model [Topping[9]] for the explanation of electron emission changes with adsorption may not be justified in many cases because the dipolar model is based on the assumption that there is a layer of polarized or ionized adparticles in a near planar arrangement parallel to the emitting surface. This condition is not satisfied by arrangements of adparticles observed.

As an alternate method for the study of the effect of dipolar moments on the electron emission from a metal surface, this author proposes the utilization of some ordered alloys that present an adequate layered structure in some directions with well defined surface density, crystallographic orientation, and chemical composition.

The preliminary studies along this line were done with the α (disordered) phase of Ni_4W in order to ascertain the magnitude of the changes produced by crystallographic differences. It was expected that the effect of chemical composition in the disordered alloy would be random and would produce the same contribution for any one of the crystallographic orientations chosen for the measurement of the electron current.

However, measurements of electron emission from the disordered α phase of Ni_4W showed differences of intensity from equivalent crystallographic directions. These differences were explained as being produced by variations in the density of solute atoms at the surface of the specimen. The variations in densities of solute atoms are to be expected from the random distribution of tungsten atoms in a nickel matrix, as was shown by counting imaged W atoms in different

areas of the field ion micrograph and using a computer simulation technique to represent the specimen's image. Similar variations of emission had been observed by Gomer[5] using a solid solution of silicon and tungsten as an emitter.

Subsequent experiments utilized the layered structure presented by the (011), (101), and (112) planes of Ni_4W β phase. Such a structure provided similar conditions to those encountered in adsorption experiments (a substrate with adsorbed layers).

Changes in electron current emission were measured after evaporating atomic monolayers from the (011) plane of ordered Ni_4W specimens. Some of the changes were found to be of the same order of magnitude as those expected by work function changes due to adsorbed atoms (applying the dipolar model). However, there were some large current emission changes noticed when a W monolayer was evaporated from the (011) plane. These changes could be compared to those predicted by Alferieff in his tunneling resonance model.

It was also observed that the intensity of the electron emission current depended on the number of nickel monolayers above the underlying tungsten layer. To explain this phenomenon, a simple model was proposed for the emission current from a layered superlattice plane. It was proposed that the same model could be applied to similar effects observed in adhesion experiments.

The model applied to Ni_4W ordered phase considers preferential tunneling electrons through the tungsten layer as the basic contribution to the electron current. Thus, the current may be affected by the

scattering produced by nickel atoms blocking the path of the electrons that have preferentially tunneled through the W atoms. (The tungsten atoms have a lower work function and electronegativity than the nickel atoms.)

Also, the nickel layers partially screen the electric field affecting the underlying tungsten layer.

However, the $\phi^{3/2}/F$ ratio of the tungsten layer lying under less than four nickel layers seems to be lower than that of the nickel layers above it. This makes the electron current through the tungsten layer larger than the current through the nickel layer.

In adsorption experiments, the preferential atoms for tunneling might be the substrate atoms or the first or second layer of adsorbed atoms (whichever presents a lower ratio $\phi^{3/2}/F$ as expressed in the model).

In his thesis the present author proposed another method for the study of electron emission. The preliminary results presented in this thesis show that the use of ordered alloys can be a promising field because it offers means to control different variables for the application of the existing models of electron emission and for the generation of new models.

In future research it would be important to proceed along the following lines:

1. Determine the work function of the layered planes of Ni_4W (or other ordered alloys) as atomic monolayers are evaporated. A method independent of the current density should be used (e.g. electron energy measurement). If there is no work function variation presented by the evaporation of monolayers on the emitting plane, another explanation must be found for the current variation observed in the experiments presented in this thesis.
2. Compare electron emission and work function changes from Ni_4W with those produced by adsorption of Ni atoms on W substrate and W atoms on Ni substrate. If four nickel layers deposited on W produce the same change in intensity (and work function) as those observed in the alloy, the dipolar model would be applicable to adsorption, in spite of the amorphous quality of the adsorbates.
3. Ascertain work function changes produced by depositing Ni or W on a Ni_4W substrate. This experiment would help in the clarification of the "smoothing" action of adsorbates. The experiments proposed above could finally clarify the use of the concept of work function change as an explanation of changes in current emission which have been produced either by (1) adsorbates or (2) layers of different chemical composition in superlattice planes of ordered alloys.

X. ADDITIONAL OBSERVATIONS OF Ni_4W

This chapter will include some observations of Ni_4W which were a by-product of the experimental process but do not bear directly on the central problem previously discussed.

A. Observation of the γ Phase of Ni_4W

Ni_4W at high temperatures (above 950°C) presents a two phase system (see Fig. 4) composed of a disordered phase (α) and a tungsten-rich phase (γ) which has the same crystal structure as pure tungsten (bcc).

For specimens annealed at 1300 K and water quenched, the probability of observing each of the two existing phases can be estimated from the proportion of the phases present at that composition. By using the phase diagram (Fig. 4), the amount of γ phase given by the lever-rule is 0.0875%, which gives a probability of ~0.01 for the imaging of the γ phase in specimens made out of polycrystalline wires containing both phases.

One of the specimens of Ni_4W annealed at 1300 K showed an unusually disordered structure decorated with streaks (Fig. 39.1). After field evaporating a few atomic layers, an ordered image which showed similarities with a pure tungsten FIM image was observed. The image attained at a very low imaging voltage (15 kV) was faint and required along exposure times to photograph it successfully (~8 min using a lens aperture f:0.87). Lowering the imaging voltage to 12 kV showed more clearly the tungsten-like image (Fig. 39.2) (in the white circle)

but other features obscured it.

Field evaporating the specimen and imaging again at the BIV did not improve the image quality. Therefore, the streaks appearing on the micrograph did not seem to be surface defects (Fig. 39.3).

To appreciate the likeness of the low voltage image (Fig. 39.2) with that of pure tungsten, a low voltage micrograph of pure W is presented in Fig. 39.4. Notice that the zone decorations are very similar to those of Fig. 39.2.

To identify further the phase under observation, a field emission micrograph was taken at 1.5 kV. The micrograph (Fig. 40.1) showed a tungsten-like emission image which, unfortunately, was surrounded by other bright spots that obscured its crystallographic characteristics. By lowering the FEM imaging voltage, a classical image of a field evaporated (110) oriented tungsten specimen appeared (Fig. 40.2). For comparison, a FEM micrograph of pure tungsten is provided in Fig. 40.4. Notice the similarities with Fig. 40.2.

Figure 40.3 shows a FEM of an α specimen imaged at low voltage. Notice that the superposition of Fig. 40.3 and 40.4 could give an image with a close resemblance to the image in Fig. 40.2. This superposition could also be the origin of the streaks, as will be shown later.

Thus, the field ion and field emission images from the as-quenched specimen could be interpreted as the first time in which the γ phase of Ni_4W has been imaged using these techniques (FIM and FEM).

The origin of the streaks could be better discussed by eliminating the most common possibilities. Figure 38.1 shows a tungsten specimen that was subjected to ion bombardment during one second by reversing the voltage on the specimen (from positive to negative) while there was a pressure of 10^{-4} Torr of helium in the microscope chamber.

Notice that the specimen shows an amorphous distribution of atoms with many bright streaks. These streaks are no doubt the product of cold work and surface pitting produced by the impinging ions. Figure 38.2 shows a micrograph obtained after "flashing" a W tip. Part of the tip was broken off by the high stress produced by the imaging field leaving a crater on the surface like that represented in the drawing of Fig. 41.a. Notice that the streaks are radial with respect to the crater (marked A) and that one of the planes sloping toward the crater (marked B) shows an elongated shape. The streaks shown in these micrographs differ from those obtained in the Ni_4W specimen, in that lowering the imaging voltage did not show any improvement in the symmetric characteristics of the image as it did in Fig. 39.2. Also, slightly changing the imaging field for the Ni_4W specimen displaced the streaks with respect to each other, and this did not occur with the W specimens.

The other possibility left for the origin of the streaks is the existence of a forked specimen (see Fig. 41.b), where the largest end of the would be a γ grain and the smaller end would be an α grain. An image produced by such a specimen would be a superposition of a disordered region with a tungsten-like image, as in Figs. 39.1 and 40.1.

Such a specimen is possible when the tip is made from a binary alloy wire, with both phases near the end of the wire.

The etching solution in this case is expected to preferentially etch the grain boundary producing the double tip and then, as it dissolves the Ni_4W α phase more than it would dissolve pure tungsten, we can expect that the α end of the fork will be reduced more than the γ end. At a high imaging voltage, both "tips" tend to image, but lowering the voltage will produce preferential ionization (or emission) at the most protruding "tip". The shorter tip will have a screened field with lower ionization (or emission) probability. This will explain why the lowering of the field exposed more clearly the W image by screening out the contribution of the α phase.

B. The β Phase

1. A Variation of the Standard Technique for Imaging Alloys

Field ion microscopy of a specific metal specimen is usually achieved at some determined optimum conditions of voltage (best imaging voltage-BIV) pressure (BIP) and temperature. The pressure is usually a constant determined from experience with a given imaging gas and a given microscope; the best imaging temperature is usually the lowest temperature achievable and the voltage is determined by the specimen evaporation potential. The best imaging voltage should yield the brightest image of the specimen without promoting field evaporation. For these experiments the BIP is 5×10^{-4} Torr and T=10 K.

In the case of some alloys and metals with relatively low melting temperatures, the BIV is very close to the voltage necessary for field evaporation; therefore, the condition for imaging becomes very difficult to produce without field evaporation.

The ordered β phase of Ni_4W, in general, could be imaged at voltages below the evaporating voltage, which would produce bright images with good atomic resolution below 78 K.

It was observed, however, that most specimens presented large irresoluble areas, comparable to those of Ni_4Mo[48,49] at BIV and BIP. It was also hard to ascertain if there were surface defects in the Ni_4W specimens.

Attempting to solve these technical problems, we found that by varying the pressure, voltage and temperature by small amounts, some of the surface features obscurred under normal imaging conditions could be clearly exposed.

Figure 36 shows a series of micrographs of Ni_4W ordered, in which variations of the above mentioned parameters yield remarkable resolution for otherwise obscurred features.

Figure 36.1 shows an FIM picture of a specimen at a helium pressure of 8×10^{-4} Torr, temperature $T > 80$ K and imaging voltage V=26 kV.

The upper arrows in the figure show sharp dark lines; the lower arrows show a pair of bright, almost parallel, lines that cut across the surface of the crystal. Similar streaks were explained by Ranganathan et al.[53] as being produced by steps at grain boundaries.

They also could be interpreted as slip lines. The letter A at the bottom of the micrograph shows one of the dark irresoluble areas of the crystal. Notice that in Fig. 36.1 the atoms cannot be resolved and appear blurred because of a slight field evaporation process. Figure 36.7 in comparison shows a field ionization pattern of the same specimen at the best imaging voltage (18 kV), pressure (5×10^{-4} Torr), and temperature (10 K). Atomic resolution is obvious; the dark bands are still present, area A is irresoluble and the sharp lines have disappeared. (Faint traces are pointed out by the arrows.)

Thus, increasing the temperature, field and pressure decreased the resolution but exposed some important surface features.

Figure 36.2 shows the FIM pattern at the same specimen temperature as Fig. 36.1 but at higher imaging pressure (2×10^{-3} Torr) and lower imaging voltage (18 kV). The area A is resolved in this condition.

By decreasing the temperature to 78 K and maintaining the same pressure and field as in Fig. 36.3, the feature marked by the arrows labeled a can be resolved. The area below the a-a line looks blurred but it is resolvable. It can be noticed that there is a small crystallographic misfit between the two areas at both sides of the plane. This is indicative of a twin boundary rather than a slip plane perpendicular to the surface. The defect marked by the next set of arrows above the a-a line could be better imaged by further decreasing the temperature of the specimen (Fig. 36.4). It can be noticed that the sharp line of Fig. 36.1 is definitely a grain boundary (right arrow), close to which a small area of α phase remains without transformating to β phase (peritectic transformation).

Further lowering of the temperature, (T=20 K) and maintaining constant the other conditions of pressure and voltage (Fig. 36.5) create an image with atomic resolution in which it is difficult to distinguish the position and characteristics of the features mentioned above. The arrows indicate the position of the grain boundary (top arrows) and the possible twin boundary (a-a line) which are barely visible. Notice again that the area A is not resolved.

Figure 36.6 shows the specimen in identical conditions as in Fig. 36.5, but the imaging gas pressure has been increased again to 2×10^{-3} Torr. Now area A is resolved as a well developed crystallographic plane with the twin boundary (now marked by black arrows) and the grain boundary above it almost invisible. However, the other bright lines visible at the bottom of Fig. 36.1 reappear. The crystallographic orientation of the thin slice of material between the bright bands also seems to be slightly different from the rest of the crystal (See Fig. 36.3 and 36.6). Consequently, it is safe to characterize the slice as shear twin probably produced by the high field stress. Figure 36.7 shows a FIM using the BIV and BIP at 10 K.

It is apparent that by varying pressure, temperature and voltage many other features of the field ionization specimens can be observed. The improvement on the image of the area above line a-a in Fig. 36.3., can be understood by looking at Eqn IIIE.5 that can be written as

$$i = \alpha[1 - \frac{2KrF}{3KT}] \sigma g P (2\pi KT)^{-1/2}$$

where KrF = V(F). When pressure P is increased, the ionic current i, from any point of the tip, is proportionally increased. The areas with a smaller ionizing field F, that were not imaged with the BIP, can be imaged with the increment of P making up for the small F (Fig. 36.4). The blurred area under the a-a line in Fig. 36.4 indicates a larger ion current from that area than from the area above it. The higher ion current is produced by an increment on the probability of ionization in that area as a consequence of the stepped surface. The blurred area is therefore at a slightly higher level than the area abbve the a-a line and presents a larger local field F. Because of this fact, the latter appears darker in Fig. 36.3 when the ionization probability of imaging gas atoms have been diminished by an increment of temperature. Equation IIIF.1 shows that the resolvable distance is linearly dependent of the absolute temperature T.

Therefore, increasing T decreases the resolution. At the same time, increasing T, increases the ion current especially from the more protruding areas (Eq. A.1).

Therefore, the salient features observed at higher temperature will be the steps produced at twin boundaries and slip planes (Fig. 36.1).

From the above discussion it is apparent that an increment of pressure above the BIP can serve to increase the depth of field of the microscope by few angstroms. Increments of temperature can be used to visualize larger features that would be otherwise obscure by the details of atomic resolution in alloys.

In pure tungsten, however, grain boundaries are clearly visible using BIP and BIV, as can be seen in Fig. 12 marked by arrow G(aug. g).

2. Dark and Bright Bands

Field ion micrographs of underdeveloped tips, that is specimens that show only a few poles developed, also show two unusual features that, to the knowledge of this author, have not been described before by other investigators. These features we shall call dark and bright bands.

The dark bands are characterized by filaments between the atoms of some crystallographic directions. (Fig. 37.3) It can easily be seen that not only the atoms in these sectors give darker images but the interatomic spaces are darker than the surrounding interatomic spaces. These bands follow very closely main crystallographic directions. By ascertaining the contrast between the dark bands and their surroundings, brightness differences as high as 75% were measured. The bright bands are rows of about six atoms in thickness that look much brighter than the surrounding areas, however these bands do not follow main crystallographic directions. The measured brightness difference for the bright bands was 22%. Both dark and bright bands of the ordered structure do not seem to be surface effects. This can be shown through field evaporation. Micrographs taken after subsequent field evaporation still show the bands (Fig. 37.2). It can also be observed that if they are produced by some kind of planar defect, these defects must be almost perpendicular to the surface under

observation, as there is no shifting of their position under field evaporation. Some of these bands appear sharper after field evaporation. Careful observation of the dark bands in Fig. 3 shows that the interatomic regions look darker, and mainly this effect produces the dark bands. The atoms of the alloy imaged under standard conditions are the tungsten atoms.

In the high index planes, like those presented in Fig. 37.3 and 4, imaging W atoms are not necessarily at the top atomic layer. Therefore, W atoms partially covered by Ni atoms just above them can be expected to image dimmer than those at the surface. Also, the area surrounding the tungsten atoms of the high index planes will image darker in the directions where the Ni atoms (with lower ionization probability) are more exposed than the W atoms. The projections of the Ni atoms in other words, occupy the interatomic spaces of the W atoms. The field ionization rate of the imaging gas is affected by the work function, surface energy states, their occupancies and electron orbital directions.

Therefore, the dark bands present in some high index crystallographic orientations (Fig. 37.3) can be explained as being caused by the lower ionization probability of the He gas at the partially covered (lower field) tungsten atoms and low ionizing Ni atoms. The bright bands shown in Fig. 37.1 and 37.2 and in the detail of Fig. 37.4, are probably formed by tungsten atoms at the uppermost atomic layer that contrast in brightness with the underlying Ni atoms (see Fig. 4). The surrounding regions that show slightly darker in the micrograph are probably mixed layers of Ni and W layers covered by one or two

loosely packed Ni layers. In both situations, the W atoms will have a lower ionization probability.

Therefore, at some stage of a field evaporation process of ordered binary alloys, it is to be expected that the image of the alloy will present patches and lines of contrast different than the rest of the crystal. This is due to the different imaging probability at the two atomic species.

ACKNOWLEDGEMENTS

The author wishes to express his deep appreciation and gratitude to Professor Jack Washburn for his advice and continuous support throughout the course of this investigation, to Prof. Alan Portis for the fruitful discussions and helpful ideas on the interpretation of my results and to Dr. Hua-Ching Tong, who introduced me to the study of surface phenomena. Special thanks are due to Prof. Ralph Hultgren, who encouraged me to de graduate work in Materials Science and was always available to answer questions. To Professors Earl Parker and Victor Zackay who often counseled and encouraged me in my studies my deep appreciation.

Many thanks are due to Ms. Alicia Ramirez who typed the manuscript and beared with me the process of organizing the material into a readable form and to Mrs. Shirley Ashley and Miss Jean Wolslegel for their patient support also during this process. Many thanks are also due to the personnel of the mechanical shop that under the direction of Mr. Ed Edwards built and often modified the field ion microscope, special thanks go to Messrs. Walter Toutolmin, Duane Newhart and Benedict Galik. To my friend and teacher Mr. Julien Patenaude who instructed me in the use of shop equipment many thanks. Many thanks are also due to Messrs. John Holthuis and Don Krieger who helped in the specimen preparation. Many thanks to Mr. Douglas Krietz and Mrs. Phila Witherell who with their art and techniques of photography enhanced this thesis, to Messrs. George Georgakopoulos and George Gordon who helped in the verification of the composition of the specimens, to Mr. Glenn Baum who kept the vacuum system functioning and Messrs. Dan Durtis, Fred Parks, Jim Severns,

Del Peterson, and Henry Brendel who designed, built and upkept most of the electronic equipment; to the industrious men of the glass shop, who made many of the delicate pieces of the microscope, and were always available at times of panic Messrs. Dane Anderberg and Paul Henickson; to Mr. Emery Kozak whose helpful ideas corrected many mistakes of my vacuum system; to Miss Sandy Stewart who promptly handled the adquisition of equipment and parts, and finally, my most expressive thanks to my co-workers and other support personnel not mentioned above who with their kind words, ideas and smiles injected hope into the moments of desperation that often plague any research endeavor.

This work was done under the auspices of the United States Atomic Energy Commission.

APPENDIX A

The Preparation of Field Ion Microscope Specimens

The preparation of sharp needles for field ionization or field emission microscopy specimens can still be classified as an art rather than a technique.

The authors would like to contribute briefly to this art with their experience.

Basically, there are two major approaches to "tip" making. These are (a) simple chemical polishing and (b) electro-chemical polishing. The latter technique is probably used more frequently and has as many variations as there are investigators in this field.

Some electrolytes are not transparent enough to permit observation of the thinning process.[1] Others require cooling.[2] Thus, the walls of the beaker get fogged and impair visibility. The authors found it convenient to use a small beaker made out of a tube 7 mm ID, the rim of which had been cut at a 45° angle (see Fig. 1). The adhesion of the liquid to the walls provided a slanted liquid-to-air interface allowing the experimenter to observe the thinning process by merely focusing the microscope to this interface and moving the specimen up and down with a manipulator.

The floating layer or double layer technique consists of suspending a thin layer of electrolyte on the surface of a denser, inmiscible, nonconducting liquid. This technique has been used by several investigators,[3] however, Müller[4] contends that the field ionization patterns of specimens obtained by this technique display indications

of plastic deformation and cold work. Also, shortly before break-off, the buoyance produced by gas bubbles at the lower part of the tip may bend it at the thinned section. Some of these effects have also been observed by us and have been avoided by using the following set-up.

A beaker, (2.5 cm in diameter), with a flat window was made and a tube 3 mm in diameter, closed at one end cut in half lengthwise, was attached to the glass window (see Fig. 2). When the beaker is filled with electrolyte, to a level just above the top open end of the small tube, air is trapped inside the tube. The wire to be thinned was introduced partially into the tube. Polishing then occurred in the thin layer of electrolyte between the two air interfaces. Motion of the tip up and down controlled the length of the thinned portion and thus the tip angle. Finally, after break-off, a pulse of current was sometimes necessary to produce the desired tip shape.

This method allows observation of the electro-chemical thinning process with a microscope, even if the electrolyte is not transparent.

Müller[5] suggests that the attack of the electrolyte should be reduced in a gradual fashion and not abruptly as with an interface. This can be accomplished using the same set-up described above but with the small tube open at both ends.

To attach the half tubes to the flat window, silicone rubber proved useful; however, as it is soluble in certain acids (e.g., HCL) wax can substitute for it. Another method is to glass weld the flat glass to the large tube and attach the small tube to the flat glass with either rubber sealant or wax.

APPENDIX B

Description of a Orientable Low Temperature-High Voltage Specimen Holder (Cryostat)

The purpose of this design was to make a sample holder that could be rotated 360° so that the specimen could be oriented toward a given instrument like a fixed electron probe, an atom probe, an ion gun or any other experimental apparatus and also toward the phosphorescent screen for direct observation of the image (Fig. 46)

The present cryostat can be described as made of two parts:

a) The cryogenic tube

b) The envelope

The cryogenic tube was made of 304 SS and is composed of three concentric tubes (see Fig. 47.1). The innermost tube serves as the cryogenic liquid inlet, (Fig. 47.2) a second tube serves as a vacuum jacket for the former and a third tube serves as a return tube for the cold gas evaporated from the specimen area (Fig. 47.3).

These three tubes were bent in 180° arc so that turning the upper shaft of the tube will produce a displacement of the lower end in such a way that the specimen would rotate on an axis passing through the geometric center of the spherical emitting surface (Fig. 47.1). Due to mechanical difficulties during construction however, the specimen rotated slightly off axis in the cryostat, but this did not disturb our experiments.

The envelope that goes over the three tubes was made from a bellows of stainless steel purchased from Standards Bellows (Fig. 47.6). The bellows was closed at one end by a glass-to-kovar tube that held a pin of tungsten, electrically insulating it from the rest of the cryostat.(Fig. 47.4 and 5).

This bellows allows the rotation of the tube and keeps the atmosphere-vacuum separation (see Fig. 46).

Under operating conditions liquid helium was used to cool the specimen.

The cryogenic liquid was thermally protected by the vacuum jacket and further protected by the returning cold gas through the return tube. The only exposed area to radiation loss was that of the glass insulator and specimen holder (tungsten pin: Fig. 47.5).

The images obtained showed that temperatures of 10 K and under were attained.

The cryostat also allowed for vertical motion of the specimen by contracting and distending the bellows. A free vertical motion of three inches was obtained.in this manner. The electrical connection was made by a tungsten wire spot-welded externally to the tungsten pin (Fig. 47.5). An spacer was found necessary (Fig. 47.6 left) to avoid grounding the wire. The spacer was found by a glass tube held by a tungsten wire that could be attached to the end of the bellows. The top plate observable in Fig. 46 is a fiber glass insulating wheel provided for turning the cryostat.

REFERENCES

1. D. B. Duke and M. E. Alferieff, J. Chem. Phys. 46(3), 923-937 (1967).
2. H. E. Clark, Field Emission through Single Strontium Alone Adsorbed on a Tungsten Ssurface (M.S. thesis) University of Maryland, 1968.
3. P. M. Gundry and F. C. Tompkins, in Experimental Methods in Catalytic Research, ed. R. B. Anderson (Academic Press, New York, 1968), p. 100-168.
4. R. Smoluchowski, Phys. Rev. 60(9), 611-674 (1941).
5. R. Gomer, Field Emission and Field Ionization, Harvard University Press, (1961).
6. R. D. Young and H. E. Clark, Appl. Phys. Lett. 9(7), 265-68 (1966).
7. H. W. Gowdy, A Study of Some Adsortive Properties of Iridium Using a Current-Probe Field Emission Microscope (Ph.D. thesis, University of California, Berkeley, California, 1973).
8. L. D. Schmidt and R. Gomer, J. Chem. Phys. 42(10), 3573-3598 (1965).
9. J. Topping, Proc. Roy. Soc. (London) A 114 67 (1927).
10. J. P. Jones, Surf. Sci. 32, 29-44 (1972).
11. L. D. Schmidt and R. J. Gomer, Chem. Phys. 43(6), 2055-2063 (1965).
12. M. Kapht, G. L. Schrenk and L. W. Zelby, Advanced Energy Conversion, 7(3), 177-189 (1967).
13. R. H. Fowler and L. W. Nordheim, Proc. Roy. Soc. (London) A 119, 173 (1928).
14. C. Hening and M. H. Nichols, Rev. Mod. Phys. 21(2), 185-270 (1949).

15. R. H. Good and E. W. Mueller, in Handbuch der Physik, ed. S. Flügge (Springer-Verlag, Berlin 21, 176-231 (1955)).

16. A. G. J. Van Oostrom, Phillips Research Reports, Supplement 1966, 102 pp. (thesis, University of Amsterdam, 1965).

17. New Values for the Physical Constants, Recommended by NAS-NRC J. Opt. Soc. Am. 54(2), 281-283.

18. F. I. Itskovich, Soviet Phys. JETP 23(5), 945-953 (1966).

19. L. W. Swanson and D. L. Dexter, J. Vac. Sci. and Technol. 6(1), 175-176 (1969).

20. R. G. Sochs and D. L. Dexter, J. Appl. Phys. 21(12), 1304-1308 (1950).

21. D. K. Dubey, Phys. Letts. A 34(3), 178-179 (1971).

22. D. Nogy and P. T. J. Cutler, Phys. Rev. Letts. 3, 263-264 (1964).

23. J. W. Gadzuk and E. W. Plummer, Phys. Rev. B 3(7), 2125-2129 (1971).

24. R. S. Hansen and N. C. Gardner, in Experimental Methods of Catalytic Research, ed. R. B. Anderson (Academic Press, New York, 1968) p. 169-216.

25. J. W. Gadzuk, Surf. Sci. 18(2), 193-203 (1969).

26. J. N. L. Connor, Phys. Rev. B 3(3), 1050-52 (1971).

27. J. L. Politzer and T. E. Fenchtwang, Phys. Rev. B 3(3), 597-604 (1971).

28. W. P. Dyke and W. W. Dolan, in Advances in Electronics and Electron Physics, Vol. 8, ed. L. Marton (Academic Press, New York, 1956) p. 89-185.

29. A. P. Ovchinnikov and B. M. Tsarev, Soviet Phys. Solid State 8(5), 1187-1190 (1966).

30. E. W. Mueller, J. Appl. Phys. 26(6), 732-737 (1955).

31. W. P. Dyke and J. K. Trolan, Phys. Rev. 89(4), 799-808 (1953).

32. L. W. Swanson and L. C. Crouser, Phys. Rev. 163(3), 622-641 (1967).

33. W. P. Dyke, J. K. Trolan, and W. W. Dolan, J. Appl. Phys. 24(5), 570-576 (1953).

34. Z. Sidorski, I. Pelley, and R. Gomer, J. Chem. Phys. 50(6), 2382-2391 (1969).

35. G. F. Smith, Thermionic and Surface Properties of Tungsten Crystals, Phys. Rev. 94, 295 (1954).

36. M. Kamisky, Atomic and Ionic Impact Phenomena on Metal Surfaces (Academic Press Inc. New York, 1965) pp. 402.

37. R. Gomer, Field Emission and Field Ionization (Oxford University Press, London, 1961) pp. 195.

38. W. B. Nottingham, J. Appl. Phys. 10, 73 (1939).

39. E. W. Müller and T. T. Tsong, Field Ion Microscopy (American Elsevier Publishing Company Inc., New York, 1969), pp. 314.

40. E. W. Müller, J. of Appl. Phys. 26(6), 732-737 (1955).

41. M. K. Wilkinson, J. of Appl. Phys. 24(9), 1203-1209.

42. L. W. Swanson and L. C. Cronser, Phys. Rev. 163, 622 (1967).

43. E. W. Müller, Act. Met. 26, 732 (1955).

44. D. G. Brandon, Surf. Sci. 5, 137 (1966).

45. E. S. Machlin, et. al., in The 12th Field Emission Symposium, The Pennsylvania State University (1965).

46. H. C. Tong and J. J. Gilman, in The Structure and Chemistry of Solid Surfaces, G. Somorjai, ed. Wiley and Sons (1962) pp. 1-70.

47. A. J. Moore and D. G. Brandon, Phil. Mag. 679-689 (1968).

48. B. G. LeFevre, H. Grenga and B. Ralph, Phil. Mag. 18, 1127-41 (1968).

49. R. W. Newman and B. G. LeFevre, Phil. Mag. 241-245 (1968).

50. R. W. Newman and J. J. Hren, Phil. Mag. 16, 211-214 (1967).

51. J. Lira-Olivares, Study of Nickel-Tungsten Alloy (Ni_4W) with Field Ion-Field-Emission Microscopy, (M.S. thesis, University of California, Berkeley, California, 1970).

52. B. Ralph and D. G. Brandon, Phil. Mag. 8, 819 (1963).

53. S. Ranganathan, K. M. Bowkett, J. Hren, and B. Ralph, Phil. Mag. 12(118), 841 (1965).

54. J. A. Becker, The Life History of Adsorbed Atoms in Annals of the New York Academy of Sciences, Vol. 58(6), 721-970 (1954), Roy Waldo, Ed.

55. V. I. Mukukha, Soviet Physics, Solid State 9(1), 111-116 (1967).

56. G. Moore and H. W. Allison, J. Chem. Phys. 23(9), 1609-1621 (1955).

57. U. V. Azizov,and G. N. Shuppe, Soviet Physics, Solid State, Vol. 7(7), 1591-94 (1966).

58. L. D. Schmidt, J. of Chem. Phys. 46(10), 3830-41 (1967).

59. A. P. Ovchinnikov.and B. M. Tsarev, Soviet Physics Solid State 9(12), 2766-2668 (1968).

60. R. A. Collins and B. H. Blott, Surf. Sci. 9, 1-17 (1968).

61. R. A. Collins and B. H. Blott, Surf. Sci. 10, 349-386 (1968).

62. R. A. Collins, Surf. Sci. 26, 624-636 (1971).

63. G. D. W. Smith and J. S. Anderson, Surface Science 24, 459-483 (1971).

64. J. R. Anderson and N. Thompson, Surf. Sci. 26, 391-414 (1971).

65. J. P. Jones, Surf. Sci. 32, 29 (1972).

66. J. Polanski and A. Sidorski, Surf. Sci. 40, 282-294 (1973).

67. A. P. Jansen and J. P. Jones, Surf. Sci. 41, 257-276 (1973).

68. E. W. Plummer and T. N. Rhodin, Appl. Phys. Letters 11(6), 194-196 (1967).

69. H. E. Clark and R. D. Young, Surf. Sci. 12, 385-389 (1968).

70. R. Hultgren, P. D. Desai, D. T. Hawkins, M. Gleise, and K. K. Kelley, Selected Valves of the Thermodynamic Properties of Binary Alloys, American Society for Metals 1973, pp. 1435.

71. J. M. Walsh and M. J. Donachue, Metallurgical Transactions 4, 2854-2855 (1973).

72. C. J. Smithells, Tungsten (Chemical Publishing Co. Inc. New York, N.Y., 1953).

73. H. C. Tong and J. Washburn, Crystal Lattice Defects 2, 221-238 (1971).

74. S. Nakamura and E. Muller, J. Appl. Phys. 36(8) (1965).

75. W. P. Dyke and W. W. Dolan, in Advances in Electronics and Electron Physics, Vol. VIII, pp. 89-137 (Academic Press 1956).

76. K. M. Bowkett and D. A. Smith, Field-Ion Microscopy (North-Holland, New York, 1970), p. 58.

77. P. Okamoto, UCRL-19175, (Ph.D. thesis), 1969, p. 20a.

78. K. M. Bowkett and D. A. Smith, Field-Ion Microscopy (North-Holland, New York, 1970), pp. 57-59.

79. E. Müller and T. T. Tzong, Field-Ion Microscopy Principles and Applications (Elsevier, New York, 1969), pp. 121-122.

80. E. Müller and T. T. Tzong, ibid, p. 122.

Table I. $\bar{I}$ average intensity measured from different crystallographic planes of a pure tungsten specimen after field evaporating a single layer.

	$\bar{I}$	S	σ	ε
(111)	62.33	8.58	2.930	2.774
(11$\bar{1}$)	60.67	3.58	1.893	1.792
(310)	78.17	1.58	1.258	1.191
(130)	77.67	1.33	1.155	1.093
(110)	55.4	85.30	9.235	6.77

Table II. A_B and A_D are the average areas of the FEM images of the planes named at left, as measured at the negative (plate).* Compare these areas with the size of the photon probe hole (0.02 mm^2). The planes that have an average image size equal to or less than 0.02 give erratic emission measurements.

Phase	Planes	A_B	A_D
ω	(111)	.03	
	(130)	1.50	
β	(101)	1.01	0.79
	(011)	1.76	1.13
	(112)	0.79	0.196
	(123)	0.008	0.008
α	(111)	0.03	0.03

* B = bright image, D = dark image (see Figs. 33 and 34)

Table III. $\bar{I}$ is the average intensities measured from three different planes of an α specimen taking three different azimuthal directions following the high work function areas (dark lines).

	$\bar{I}$	S	σ	ε
(111)	64.167	0.083	.289	.273
(301)	34.333	1.083	1.041	.986
(100)	37.500	.750	.866	.820

I_i intensities measured from the (111) plane of an α specimen after field evaporating a single atomic layer; $\bar{I}$ is the average intensity, S variance, σ standard deviation and ε probable error.

	I_i	$\bar{I}$	S	σ	± ε
1	31.5	30.166	1.583	1.258	1.1914
2	29.00				
3	30.00				

Table IV. $\bar{I}_1$ to $\bar{I}_5$ average intensities measured after field evaporation single layers of the (011) plane in Ni_4W β phase. S is the variance σ the standard deviation and ε the probable error of the measurements.

i	$\bar{I}_i$	S	σ	±ε
1	78.50	0.125	0.3535	0.26
2	51.20	77.075	8.77924	6.44
3	75.40	0.925	0.9617	0.70
4	76.60	0.300	0.5477	0.40
5	77.90	0.550	0.742	0.54

Table V. I_1 to I_5 average intensities measured at the (213), (112), (123) and (101) planes after field evaporating single layers of the (011) plane in Ni_4W β phase. ε is the probable effor of the measurements.

Intensities	Planes							
	(213)	±ε	(112)	±ε	(123)	±ε	(101)	±ε
I_1	75.80	.55	76.00	.52	75.90	.44	51.30	2.94
I_2	70.60	.65	67.40	.80	66.70	2.67	34.60	2.39
I_3	18.50	1.16	49.80	3.29	17.60	1.95	41.70	6.65
I_4	53.80	1.81	47.80	1.50	40.60	1.77	75.10	.52
I_5	74.50	1.24	76.13	0.98	75.00	0.25	70.75	1.43

Table VI. Ratio of the average intensities obtained from the (011) plane (Table IV) and the work function change $\Delta\phi$ obtained from the F-N equation.

	011	I/I_o	$\Delta\phi$
I_1/I_5	1.00488	- 0.04788	.51
I_2/I_5	.65536	- 0.422571	4.48
I_3/I_5	.96512	- 0.3550	3.76
I_4/I_5	.98048	- 0.01971	.28
I_2/I_1	.65271	- 0.4277	4.51

Table VII. Density of spots (imaged atoms) in the field ion microscope and computer simulation pattern of as-quenched Ni_4W (α phase) (from Ref. 51).

Field Ion Micrograph		Computer Simulation
Sector	Density (spots) / cm^2	Density (spots) / cm^2
	78°K	
(111) - (110)	5.0	3.54
(111) - (100)	30.0	7.05
Random areas	30.0	10.05

FIGURE CAPTIONS

Fig. 1. (a) Potential energy diagram for electrons at a metal surface in the presence of an applied electric field (——) showing contributions from the image potential (---) and the applied field of 30 mv/cm (-·-·-·) (from Ref. 2). A shows the direction of motion of the tunneling electron in field emission. ϕ and μ are the work function and chemical potential respectively. X is the distance from the surface. F=E in the text.

(b) Potential model used by Duke and Algerieff calculation for tunneling through an adsorbed atom (from Ref. 1).

Fig. 2. (a) Potential energy of an electron of an atom.

(b) Potential energy of an electron of an atom in an electric field.

(c) Potential energy of an electron of an atom near a metal surface that is the source of an electric field. I is the ionization potential of the atom, ϕ is the work function for electrons going into or out of the metal surface. (from Ref. 39, p. 10).

Fig. 3. Schematic diagram of work function versus coverage of copper dependence for loosely packed planes of tungsten (from Ref. 66).

Fig. 4. Phase diagram of nickel-tungsten alloys, including the newly discovered δ phase and broadening of the β phase (from Ref. 70, 71 and 73).

Fig. 5a & b. Crystallographic orientations of a given order domain of the β phase with respect to the α phase. Cross-hatched circles are atoms in the (002) plane. Open circles are atoms in the (001) plane. Large circles represent W atoms and small ones Ni atoms.

Fig. 6. (a) Alternating tungsten layers with four nickel layers parallel to the (121) superlattice plane.

(b) Layers of intermixed nickel and tungsten atoms forming the fundamental (211) plane (from Ref. 48).

Fig. 7. (a) Schematic representation of the field evaporation process in a low index plane of a pure metal. The uppermost layer evaporates much faster than the other layers.

(b) Schematic representation of a field evaporation process in a layered alloy. The second layer tends to evaporate at the same time as the uppermost layer (see Chap. III, Sec. F. 1b).

(c) Schematic representation of field evaporation of an ordered alloy showing that solvent atoms evaporate preferentially when they are just above a solute atom (based on Ref. 39).

Fig. 8. Three dimensional drawing of four unit cells of the Ni_4W β phase. Large circles represent tungsten atoms, small circles represent nickel atoms. The planes drawn are (101) planes that are crystallographical equal to the (011) planes in this structure. Cross-hatched planes are "all tungsten" planes.

Fig. 9. Three dimensional drawing of a unit cell of Ni_4W β phase showing partially the (112) layers.

Fig. 10. Three dimensional drawing of a unit cell of Ni_4W β phase showing the (213) layers.

Fig. 11. Three dimensional drawing of a unit cell of Ni_4W β phase showing the (123) layers.

Fig. 12. Field ion micrographs of a tungsten specimen showing the process of adsorption of tungsten atoms and its subsequent field evaporation. (See text Sec. VIII.C)

Fig. 13. Field ion micrographs of a tungsten specimen showing the process of adsorption of Ni atoms and its subsequent field evaporation. (See text Sec. VIII.C)

Fig. 14. (1) Field ion micrograph of a tungsten specimen with adsorbed ethyl alcohol molecules at 10 K.

(2) Field ion micrograph of a tungsten specimen with adsorbed acetone molecules at 10 K.

Fig. 15. (1) Typical filed ion micrograph of a field evaporated tungsten specimen with some of the low index planes indexed.

(2) A typical field emission micrograph of a field evaporated tungsten specimen with some of the low index planes indexed.

Fig. 16a & b. Graph of azimuthal measurements of intensities on a tungsten field evaporated specimen. Using a Jarrell-Ash recording microphotometer, each measurement was made after evaporating one monolayer. The dashed line is an average of the intensity around the (110) plane.

Fig. 17. (1) Field emission micrograph of a field evaporated Ni_4W specimen α phase with a (111) orientation (T=20 K).
(2) The corresponding field ion micrograph to Fig. 17.
(3) Another field emission micrograph of the same specimen after evaporating one monolayer from the (111) plane. There are no noticeable changes in intensities.
(4) A field ion micrograph of a (001) oriented specimen of Ni_4W α phase (T=80 K).

Fig. 18. Stereographic projection of an fcc crystal with the same orientation of Fig. 17.1 to 17.3, showing the high work function (low emission) areas (cross-hatched).

Fig. 19. Stereographic projection of an fcc crystal with the same orientation as Fig. 19 and showing the high work function areas (cross-hatched).

Fig. 20. Graph of azimuthal measurements of intensities performed on a Ni_4W α phase specimen using a Jarrell-Ash microphotometer. Notice that there are only minor variations of intensities between the three different directions A, B and C taken at 120 degrees from one another.

Fig. 21. (a) Four measurements of intensities taken across the (111) plane of a field evaporated specimen of Ni_4W α phase. Figure 21(b) and (c) were measurements made after evaporating one and two monolayers respectively from the original specimen in Fig. 21(a).

Fig. 22. Field emission micrographs of a Ni_4W β phase specimen. Notice the variation of intensities in the areas shown by the arrows A and B after evaporating a few monolayers from the surface. (Fig. 22.2, 22.3, and 22.4) Figure 22.3 shows two lines in the direction of sweep of the microphotometer.

Fig. 23. Intensity measurements performed on the specimen shown in the FEM of Fig. 22 using the Jarrell-Ash microphotometer. Figure 23a, 23b, and 23d present four different directions of sweep, parallel to the lines shown in Fig. 22.3. Curves A, B and C were taken after evaporating a few monolayers from the surface.

Fig. 24. A typical sequence of field ion micrographs and its corresponding field emission micrographs from Ni_4W β phase specimen. The two highest emissions are marked W in the FEM as they correspond to a tungsten monolayer at the surface. The numbers 1 to 5 indicate the evaporation process initiated at 1 and the cycle is completed at 5.

Fig. 25. Intensity measurements taken from a field evaporated Ni_4W (β phase) specimen using a Jarrell-Ash microphotometer when the (011) plane presents a maximum emission.

Fig. 26. Shows the intensity measurements after evaporating a monolayer from the (011) plane.

Fig. 27 to 29. Obtained after evaporating 2, 3 and 5 monolayers respectively.

Fig. 30. Average intensity versus evaporation plot for the (011) plane of Ni_4W phase. The Roman numerals I to V indicate the evaporation of 0 to 4 monolayers from the (011) plane.

Fig. 31. Intensity versus evaporation plot similar to Fig. 30 but for the (123) planes. Circles are average intensities measured from the (123) plane and triangles from the (213) plane.

Fig. 32. Field ion micrographs of a low index plane of Ni_4W phase showing Ni and W atoms. (See text Chap. III)

1. The nickel atoms are under a layer of tungsten atoms.
2. A nickel layer is partially evaporated at the surface of a plane.
3. A nickel layer (barely visible) during field evaporation.
4. A clearly visible Ni layer on top of a W layer on a (011) plane.

Fig. 33. Field ion and corresponding field emission micrograph of low index planes of Ni_4W phase.

1. The uppermost visible layer if 45 Å in diameter and produces a bright field emission image (2).
3. The uppermost visible layer is 30 Å in diameter and produces a bright field emission image (4).
5. The uppermost layer is 20 Å in diameter and produces a bright field emission image.

Fig. 34. Same as Fig. 33. However, the field emission images are dark.

1. Uppermost visible layer is 15 Å in diameter and produces a dark field emission image.
2. Uppermost layer 20 Å in diameter and produced a dark image.

Notice that 1 and 2 are comparable in size to 3 and 5 of Fig. 33. However, their field emission images are remarkably different.

3. Uppermost layer about 35 Å in diameter and produces a dark field emission image. These micrographs compare in size with Fig. 33.1 and 33.2.

Fig. 35. Schmatic diagram of a section of a (011) plane of Ni_4W β phase showing the position of the nickel atoms (cross-hatched circles) with respect to the tungsten atoms (open circles) lying under them. Figure 35a, 35b, 35c, and 35d represent one, two, three and four monolayers of nickel on a tungsten monolayer.

Fig. 36. A sequence of field ion micrographs of Ni_4W β phase. (See text Sec. X.B).

1. Shows a field ion micrograph of a specimen at an imaging gas pressure $P=8\times10^{-4}$ Torr, temperature T=90 K and imaging voltage V=26kv. Arrows show streak contrasts. Letter A shows irresolvable area.
2. Same specimen. T=90K, $P=2\times10^{-3}$ Torr, V=18KV
3. T=78K, $P=2\times10^{-3}$ Torr, V=18KV

4. T=50K, P=8×10^{-4} Torr, V=20KV

5. T=20K, P=8×10^{-4} Torr, V=20KV

6. T=20K, P=2×10^{-3} Torr, V=20KV

7. T=10K, P=6×10^{-4} Torr, V=22KV

Fig. 37. (1) Bright bands observed in a FIM of Ni_4W β phase at T=10K, P=2×10^{-4} Torr, V=18KV

(2) Same as 37.1 after field evaporation.

(3) Dark bands shown by arrow observed in a FIM of Ni_4W phase specimen at BIV and BIP. (T=10K, P=4×10^{-4} Torr, V=18KV)

(4) A detail of 37.2.

Fig. 38. (1) Field ion micrograph of a tungsten specimen damaged by ion bombardment produced by reversing the potential from + 28KV to -1.5KV in a helium atmosphere.

(2) A crater produced by "flashing" of a W specimen shown by letter A. Streaks produced by cold work are shown by arrows (a).

Fig. 39. (1) Field ion micrograph of a Ni_4W specimen as quenched from 1100°C showing an unusually disordered structure decorated with bright streaks. (See text Sec. X.A.)(V=18KV)

(2) Same specimen as in Fig. 39.1 but at a lower voltage (V=12KV). Notice the tungsten-like structure (γ phase).

(3) Same specimen as Fig. 39.1 and 19.2 after field evaporating several atomic layers (V=18KV).

(4) A field ion micrograph of pure tungsten at a voltage well below BIV to show its similarity with Fig. 39.2.

Fig. 40. (1) Field emission micrograph of the Ni_4W specimen shown in Fig. 39.1 to 39.3 (V=1.5KV). It has been tentatively indexed with a (110) central plane.

(2) Same as Fig. 40.1 but at a lower imaging voltage (900V). Notice the tungsten-like image with a definite (110) orientation. (This is evidently a γ phase specimen.)

(3) A field emission image of a Ni_4W γ phase specimen at a voltage well below the BIV (V=700V).

(4) A typical field emission micrograph of a pure tungsten field evaporated specimen. Notice the similarities with Fig. 40.2.

Fig. 41. (a) A sketch of a field-ion-field emission microscope tip, highly magnified, showing a central crater produced either by bombardment or be "flashing" of the specimen. A tip like this would produce an image similar to Fig. 38.2.

(b) A sketch of a forked tip presenting a γ crystal in the more protruding end of the fork and an α crystal forming the other end and the shank. It is believed that the micrographs in Fig. 39 and Fig. 40 were produced by a specimen with a shape similar to the one on the sketch.

Fig. 42. A photograph of field ion-field emission microscope used for the experiments reported in this thesis. Some minor modifications were made for individual experiments.

Fig. 43. Diagramatic drawing of the instrument shown in Fig. 42.

1. Specimens
2. Cold finger (cryostat)
3. Glass window with quartz screen covered with a phosphorescent material.
4. High voltage connections.

Fig. 44. Schematic diagram of the optical system of the Jarrell-Ash microphotometer used in these experiments.

Fig. 45. The metal evaporator used in the early part of these experiments. Notice the cap (lower left) with the magnetic swinging gate and the orifice. Also notice the intermediate chamber at right that houses the gate and the two steel bars that conduct the magnetic field from the outside.

Fig. 46. The steerable cryostat used in the latter part of these experiments. Notice the standard bellows that provides the possibility of vacuum tight circular and vertical orientation. Lower left (1 near end of the meter stick) the electrically insulated specimen holder. Upper right, thermally insulated steering wheel. (See text Appendix B)

Fig. 47. Components of the cryostat shown in Fig. 46.

1. Triple tube (bent at 180° at the end) which serves as inlet and outlet for the cryogenic liquid (or gas). The innermost tube is surrounded by the outlet tube and both are protected by a vacuum jacket.
2. A detail of the lower end of the cryostat (lower left in Fig. 47.1). The two visible tubes are the inlet tube and the outlet tube. The vacuum jacket only reaches up to the flange shown.
3. Upper end of the cryostat. The three tubes mentioned in caption 47.1 are clearly visible.
4. Specimen holder. Rear view. Notice that it is electrically insulated (surrounded by glass) and will set within the lower end of the inlet tube. The whole cap is finally welded to the standard bellows. (See Fig. 47, lower left).
5. Front view of the specimen holder (a forked holder was also tried). Notice the insulated tungsten pin.
6. The standard bellows used as a vacuum tight capsule for the whole system.

Fig. 48. Photographic camera built for these experiments. The lens is a Super-Fanon 1:87 with a compur system for a shutter. The base shown slid on parallel bars in front of the screen.

Fig. 49. Sketch of a small beaker used for specimen preparation when opaque electrolites were utilized. (See Appendix A).

Fig. 50. Sketch of a small beaker used for the preparation of specimens. The flat side allows microscopic examinations of the whole process and the air bubble trapped in the smaller tube permits the control of the area to be polished. (See Appendix A).

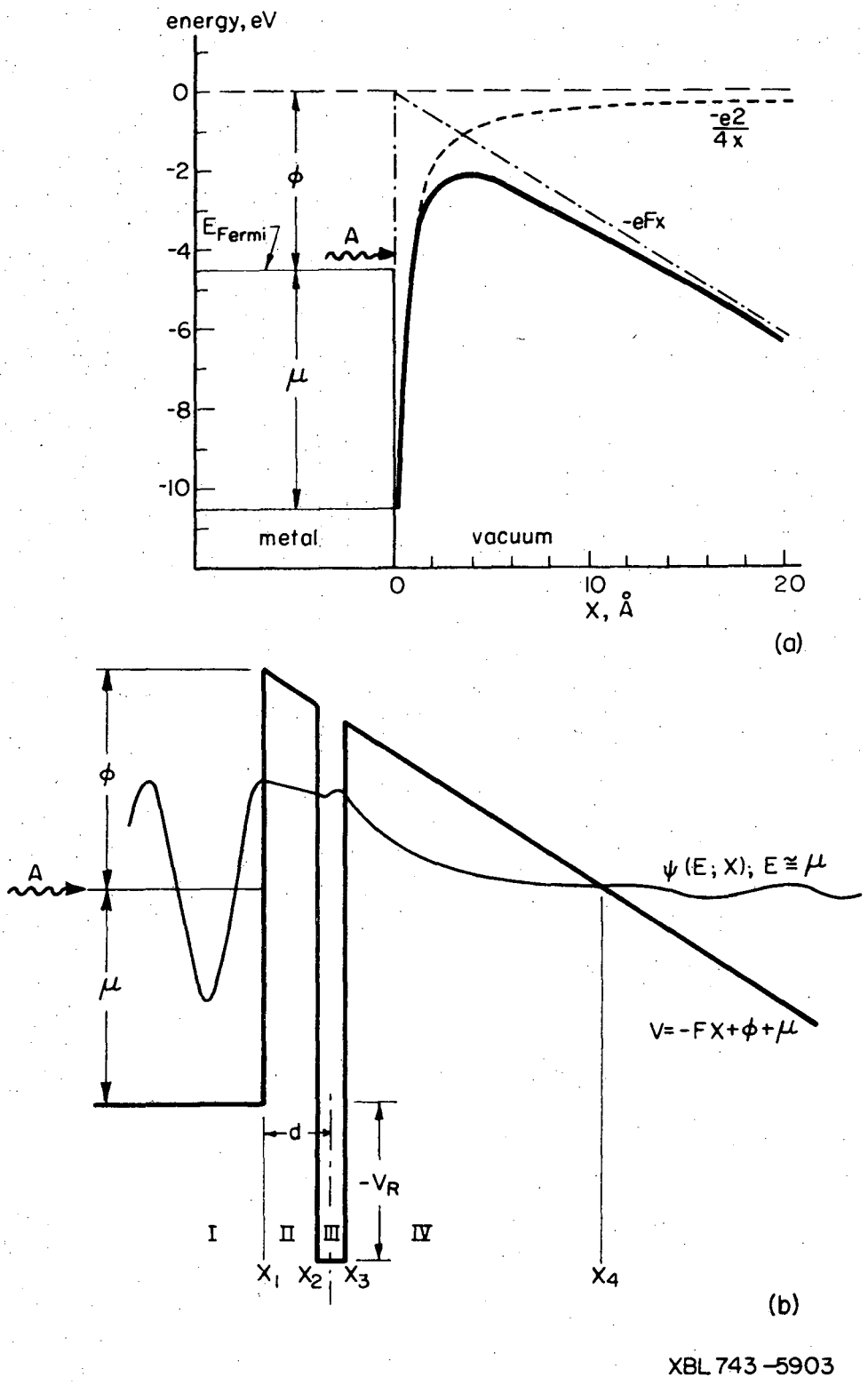
energy, eV
0
-2
-4
-6
-8
-10
ϕ
E_{Fermi}
A
μ
$\frac{-e2}{4x}$
-eFx
metal
vacuum
0
10
20
X, Å
(a)
ϕ
A
μ
$\psi(E;X)$; $E \cong \mu$
$V=-FX+\phi+\mu$
d
$-V_R$
I
II
III
IV
X_1
X_2
X_3
X_4
(b)
XBL 743-5903

Fig. 1.

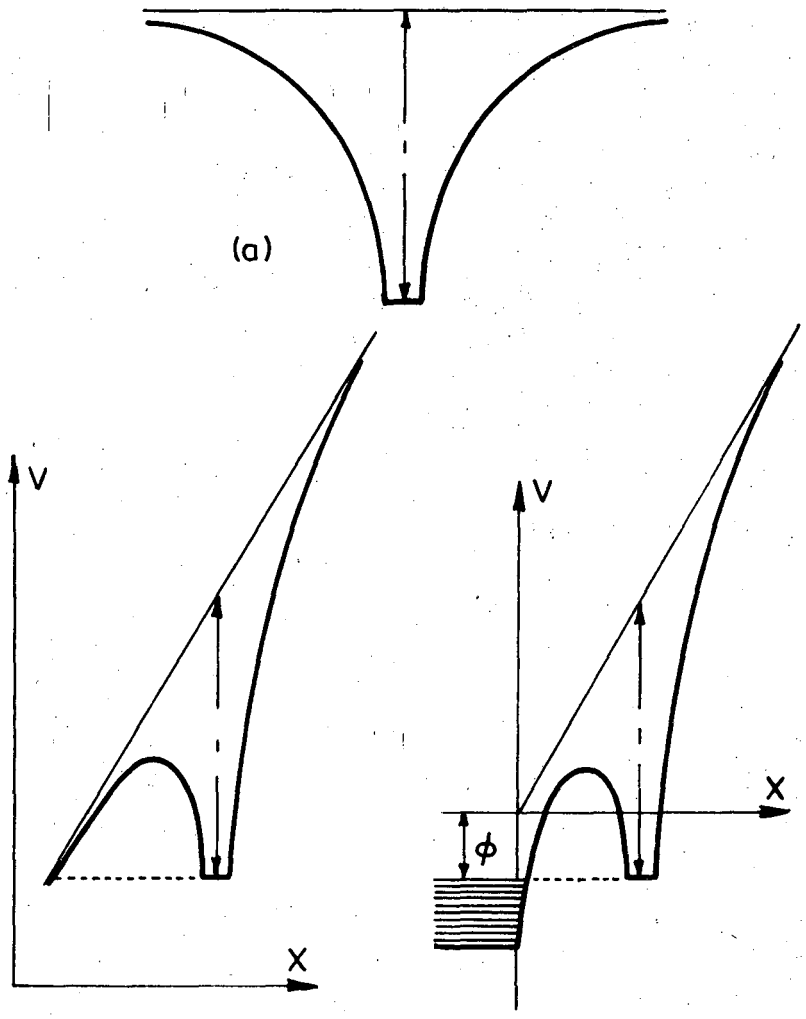

Fig. 2.

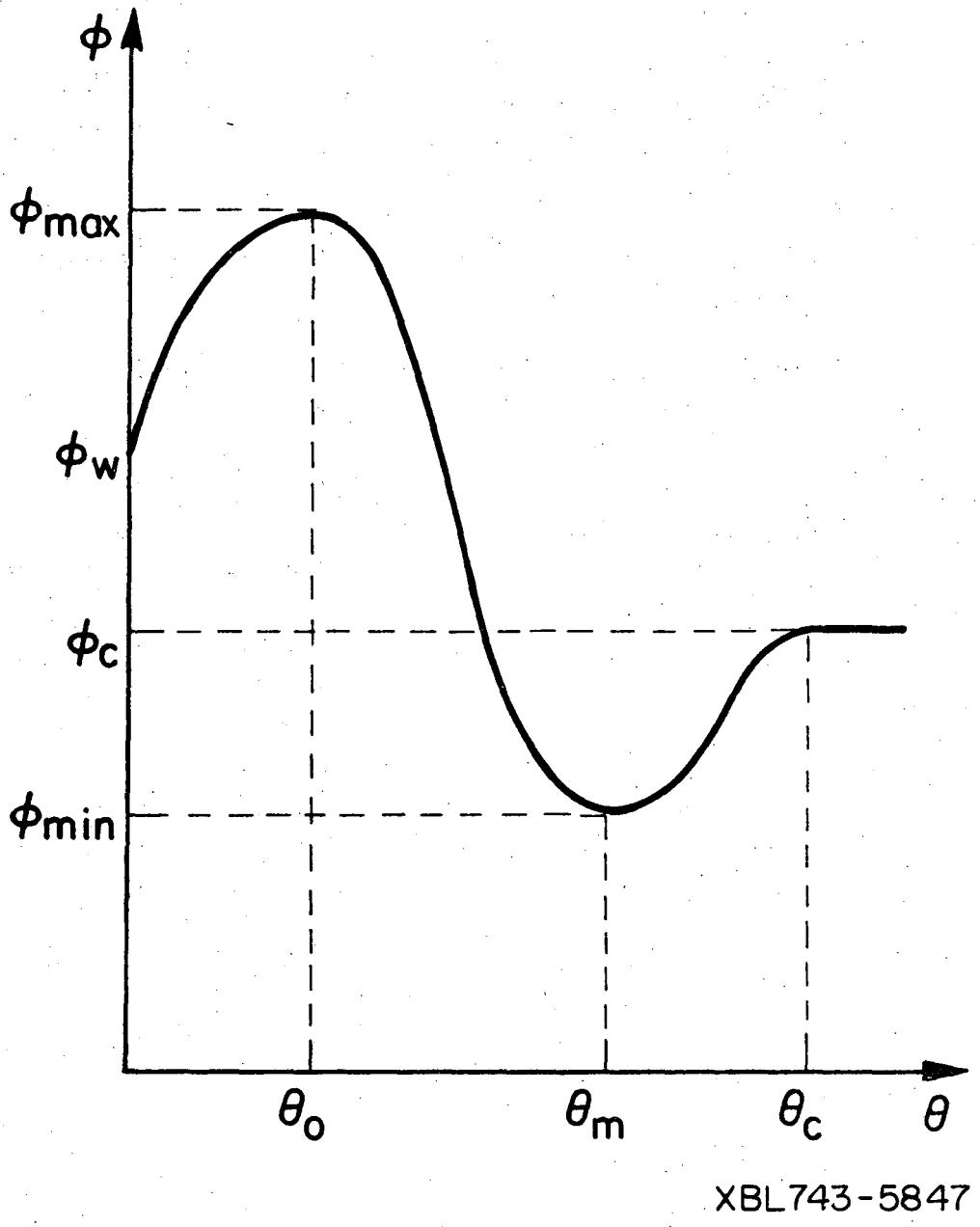
ϕ
ϕ_{max}
ϕ_w
ϕ_c
ϕ_{min}
θ_o
θ_m
θ_c
θ
XBL743-5847

Fig. 3.

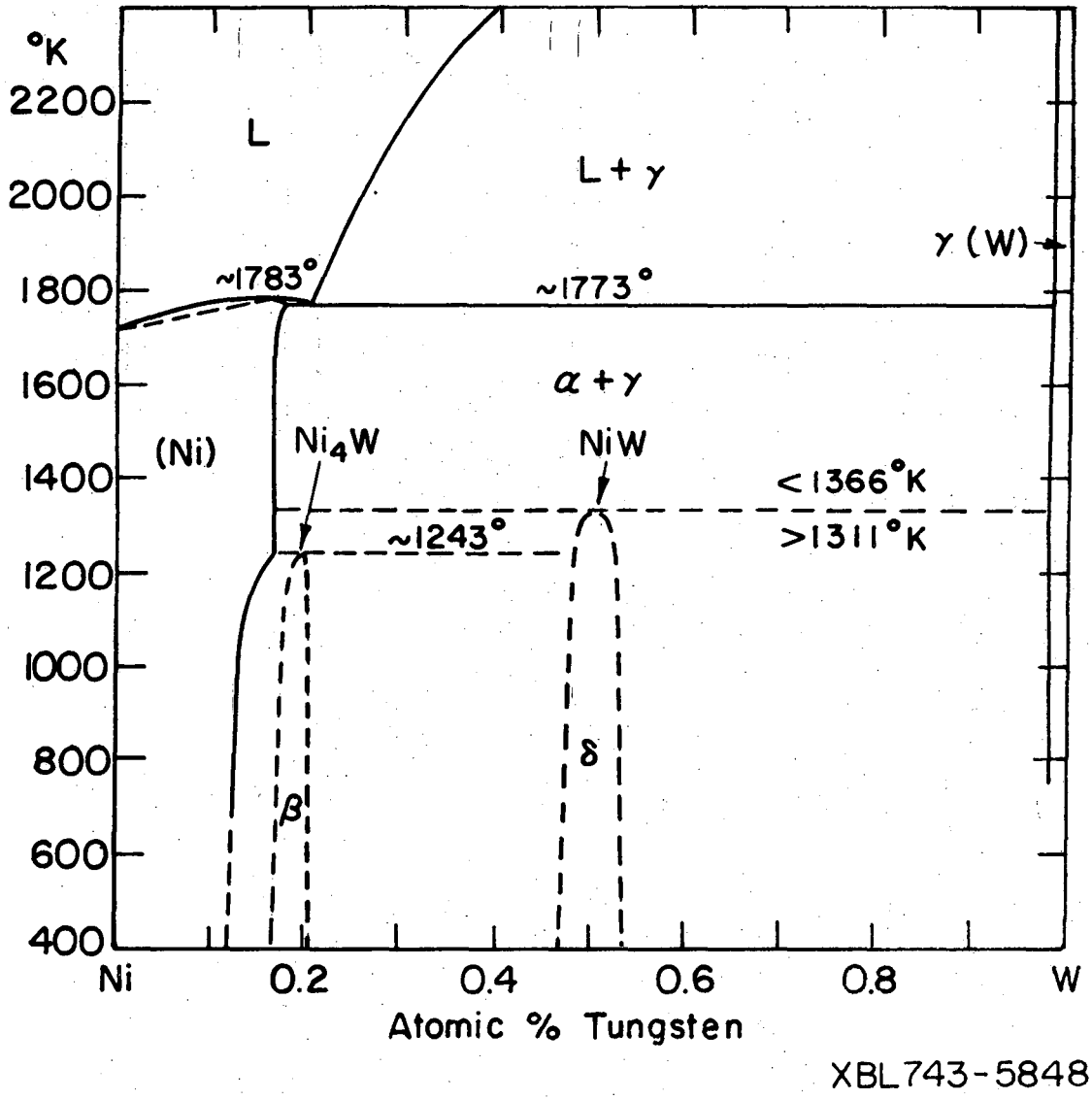
°K
2200
2000
1800
1600
1400
1200
1000
800
600
400
L
L + γ
γ (W)
~1783°
~1773°
α + γ
(Ni)
Ni4W
NiW
<1366°K
>1311°K
~1243°
β
δ
Ni
0.2
0.4
0.6
0.8
W
Atomic % Tungsten
XBL743-5848

Fig. 4.

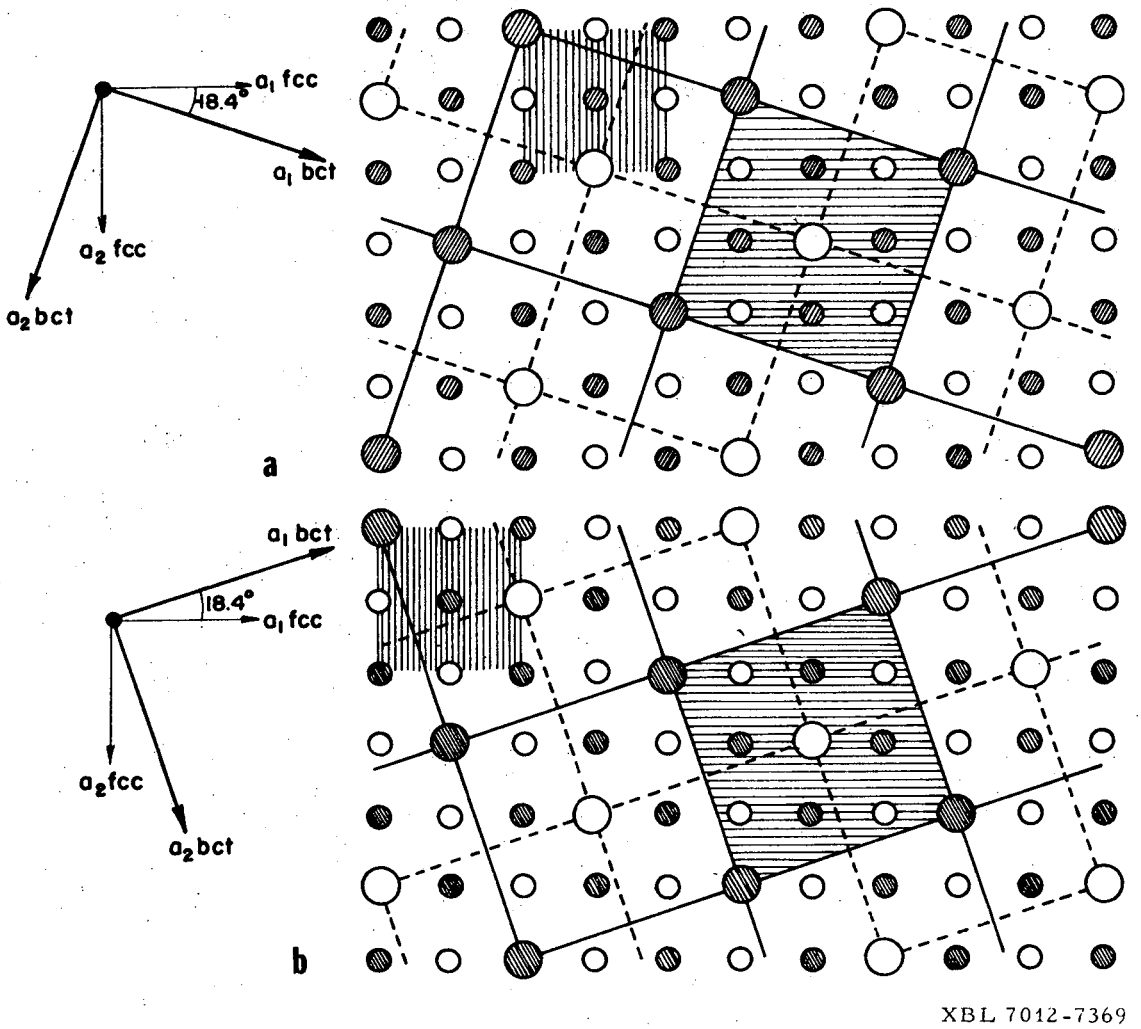
a1 fcc
18.4°
a1 bct
a2 fcc
a2 bct
a
a1 bct
18.4°
a1 fcc
a2fcc
a2bct
b
XBL 7012-7369

Fig. 5.

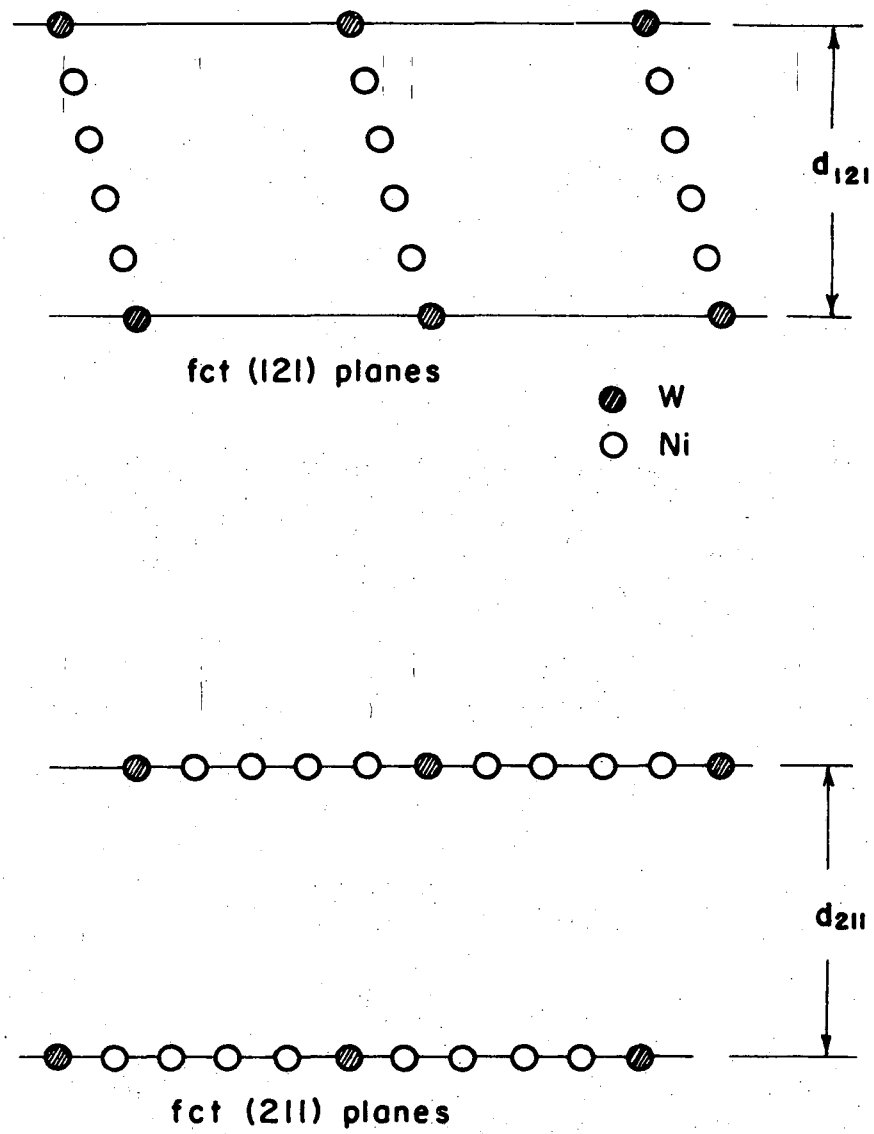

XBL 7012-7373

Fig. 6.

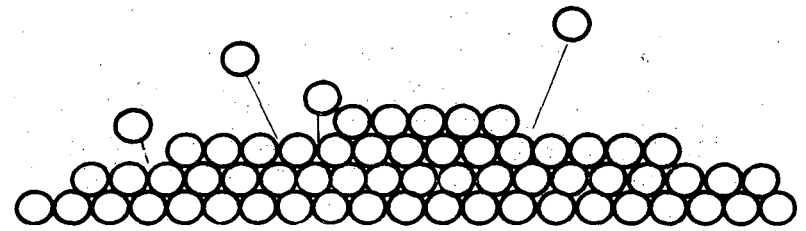

(a)

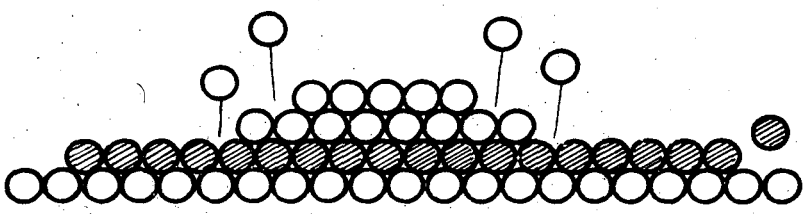

(b)

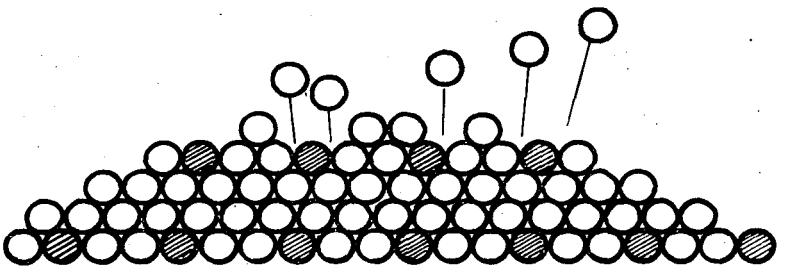

(c)

XBL743-5849

Fig. 7.

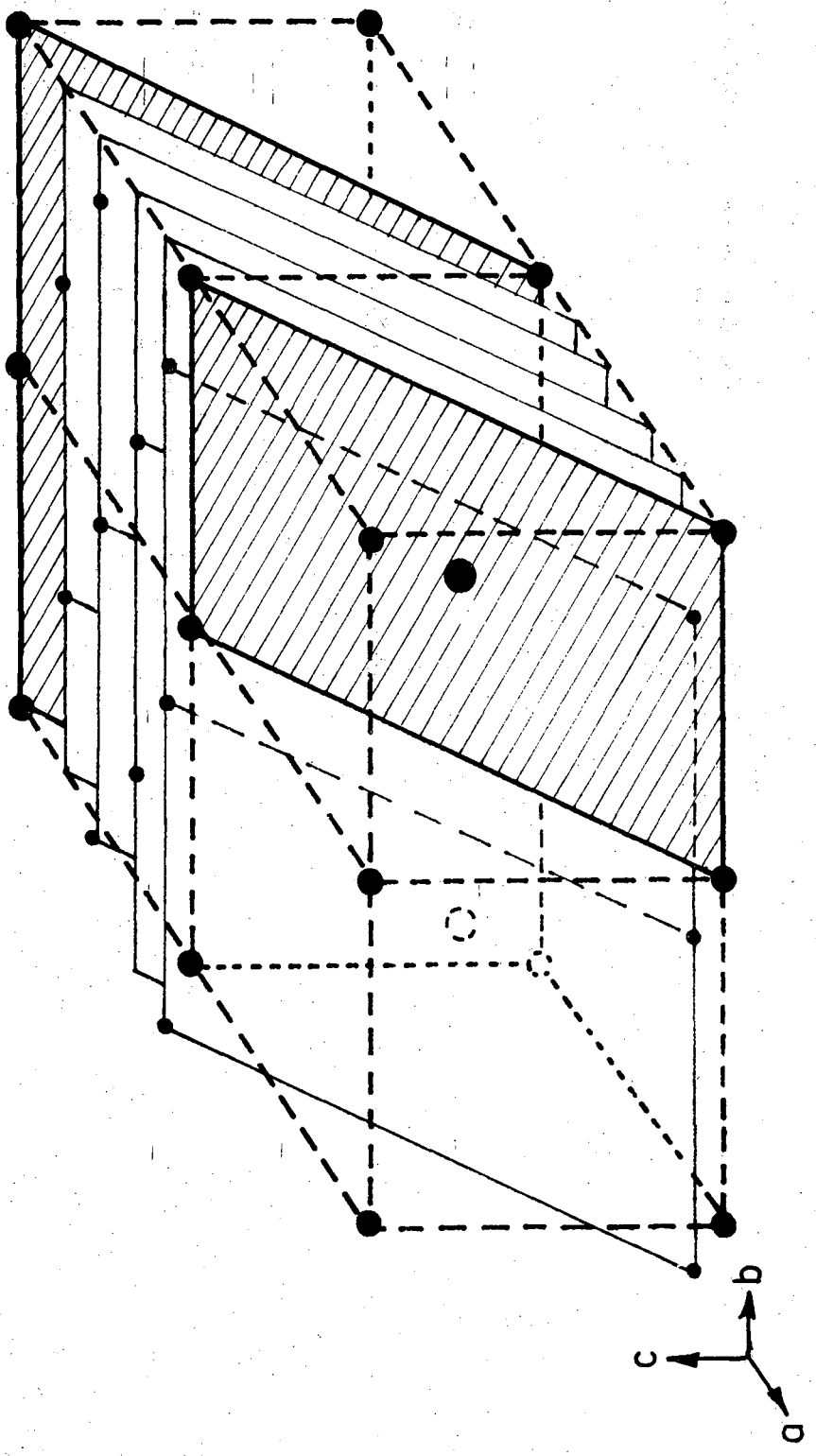

XBL743-5852

Fig. 8.

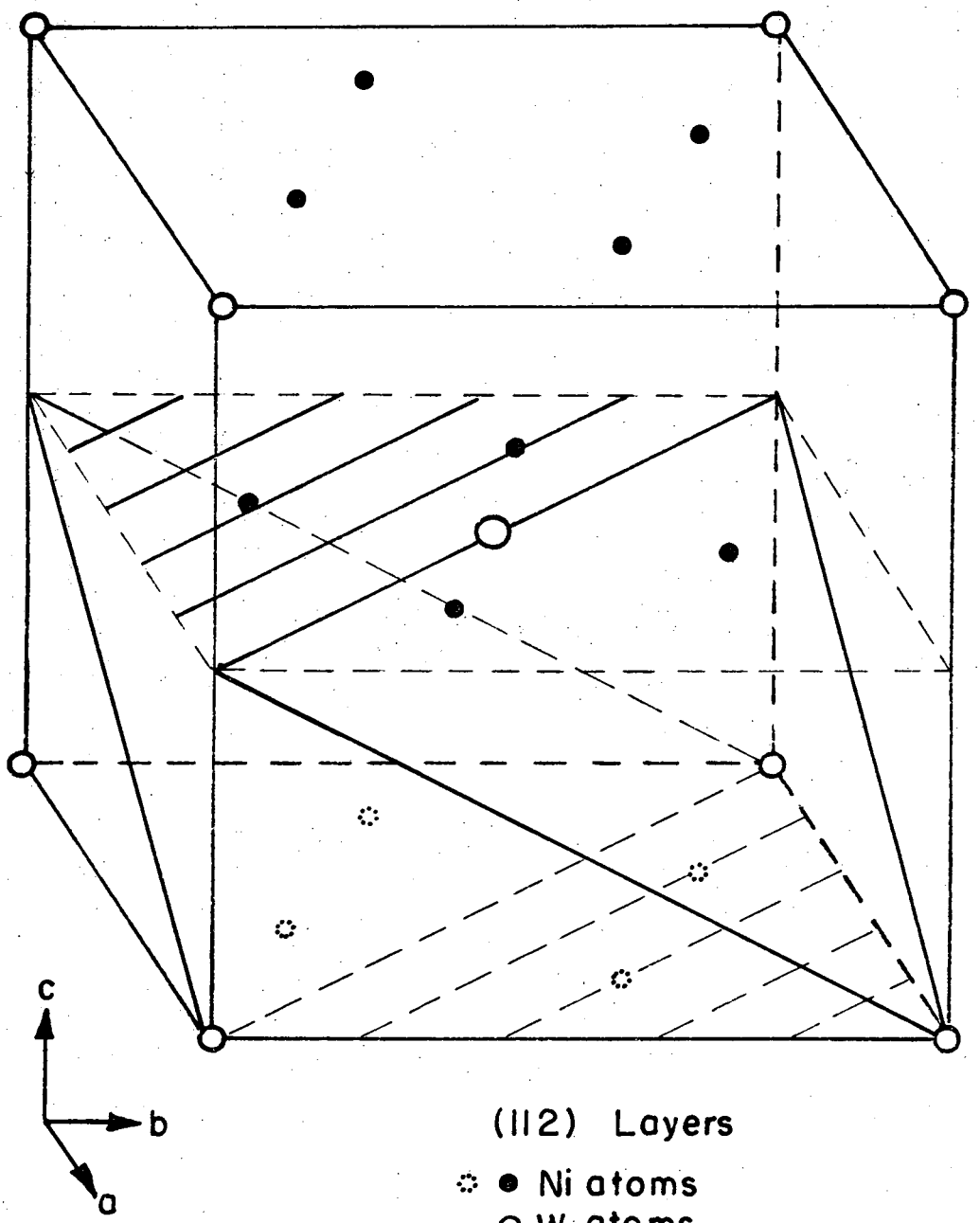

Fig. 9.

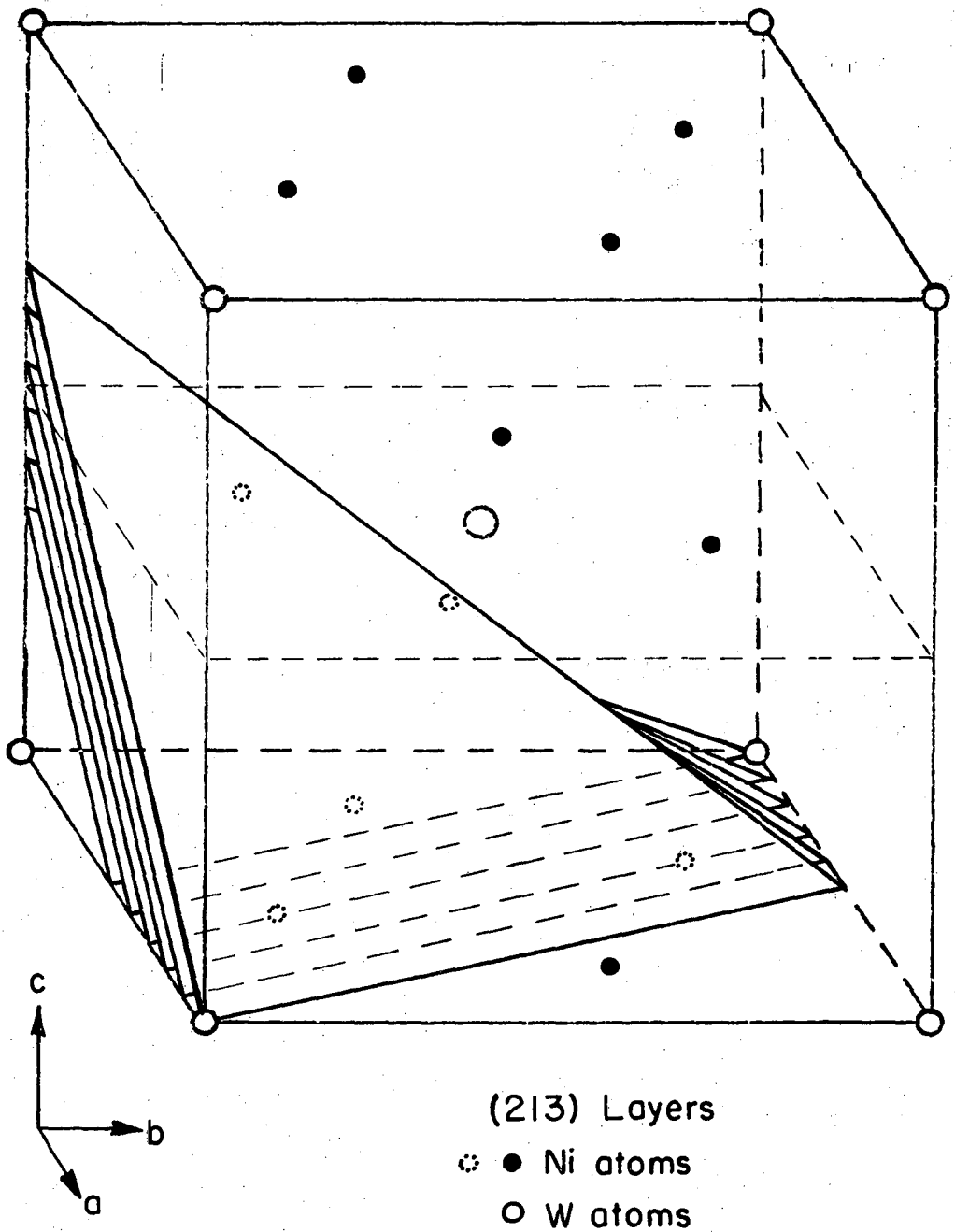

Fig. 10.

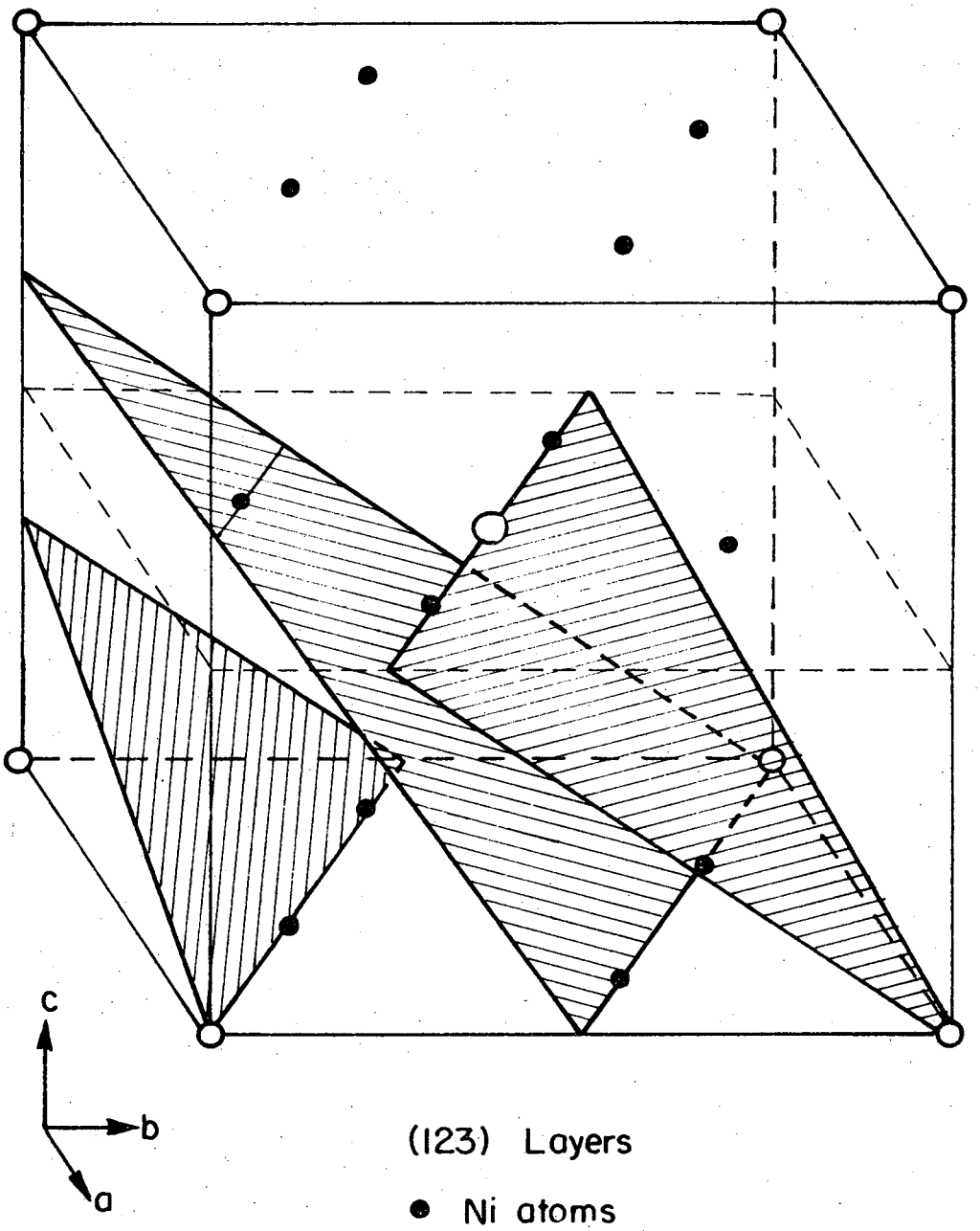

Fig. 11.

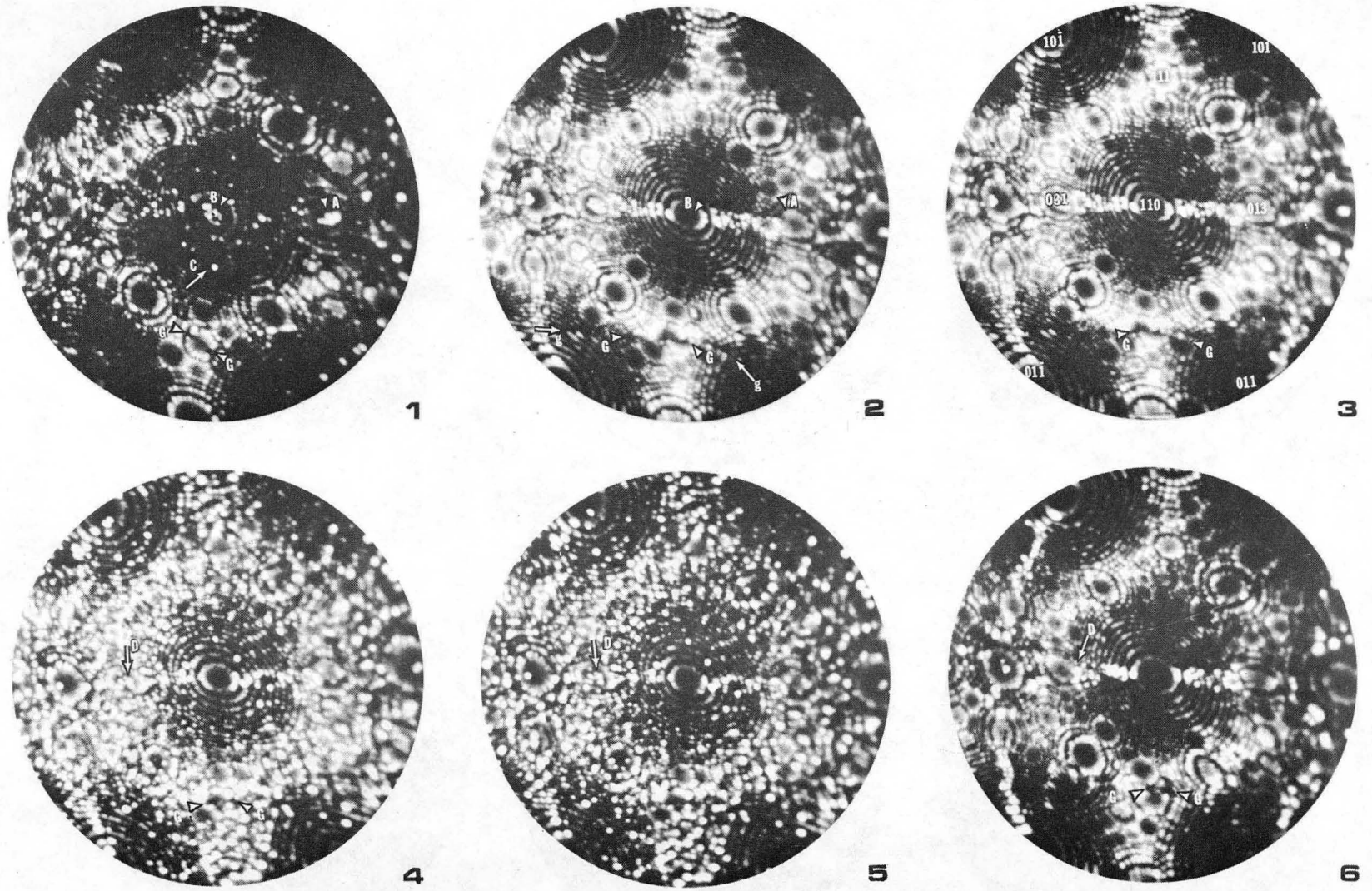

XBB 742-1149

Fig. 12.

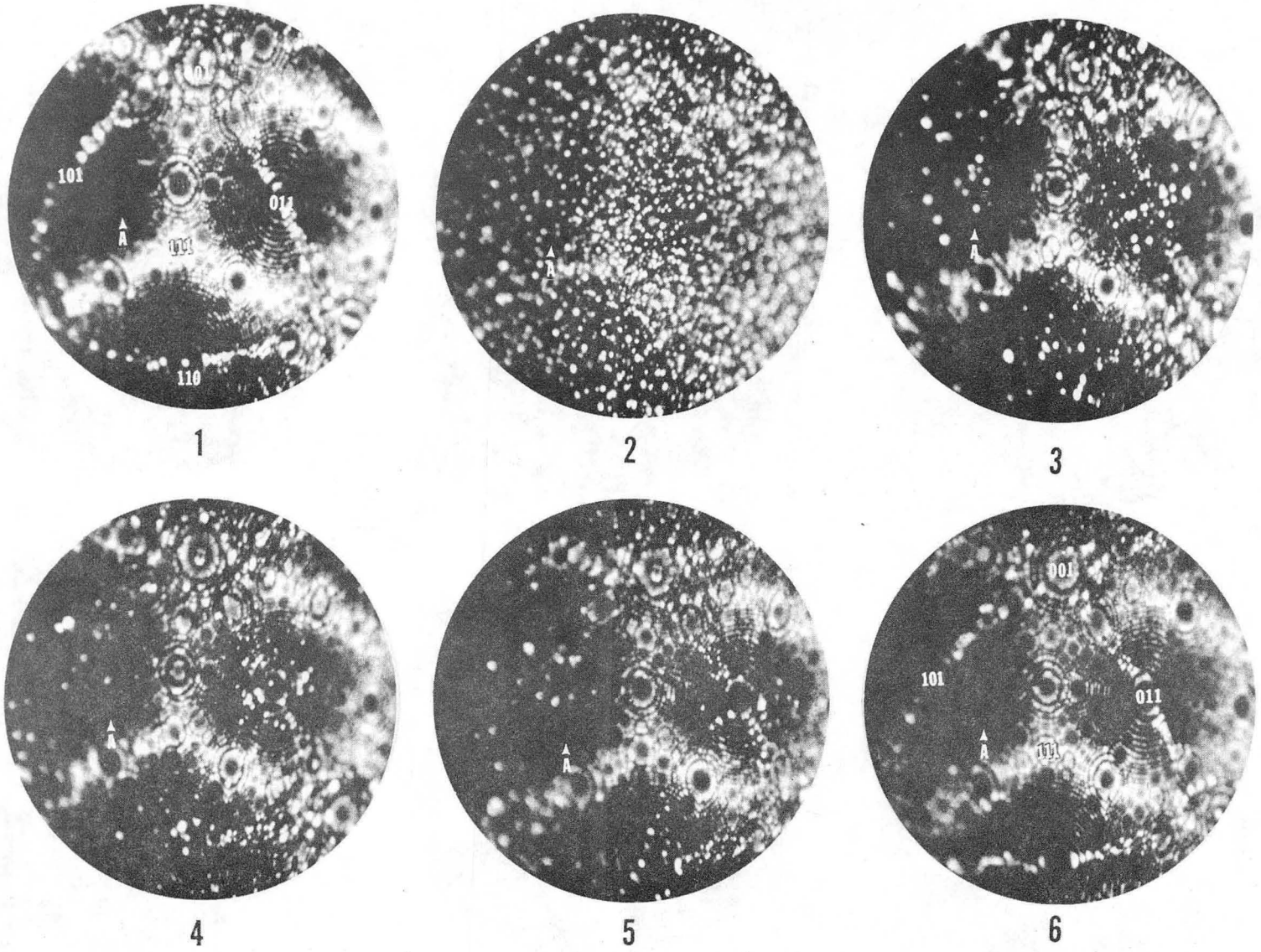

XBB 743-1602

Fig. 13.

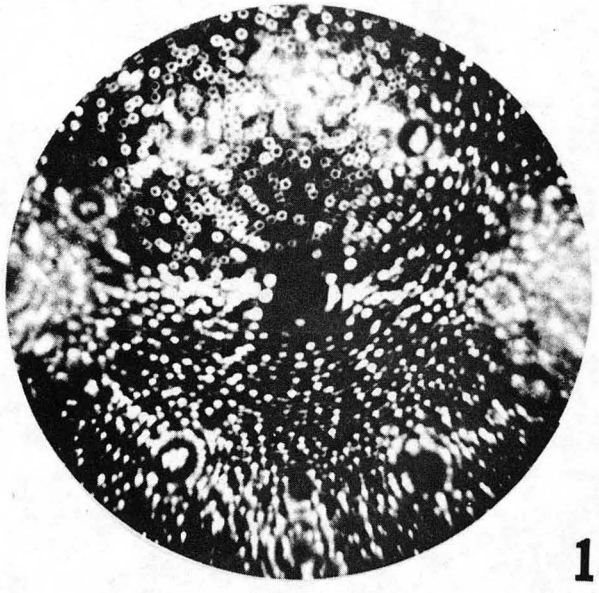

1

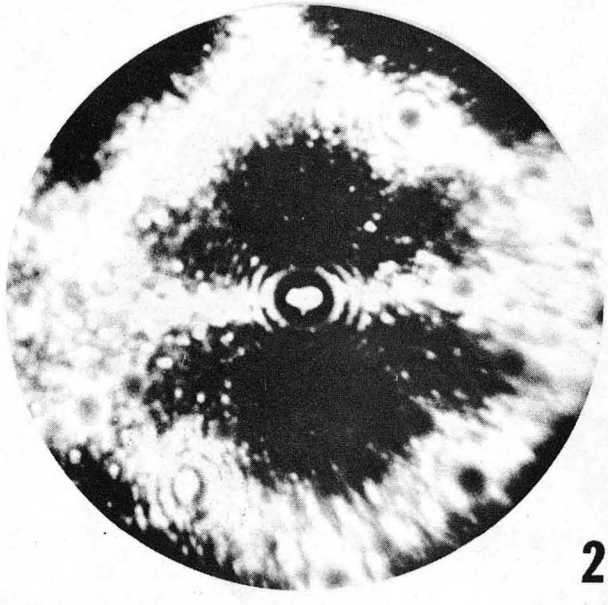

2

XBB 742-1603

Fig. 14.

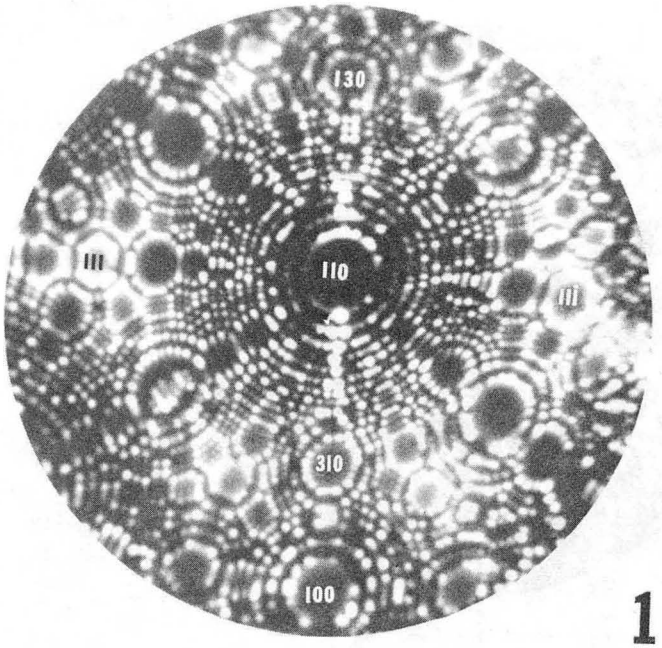

1

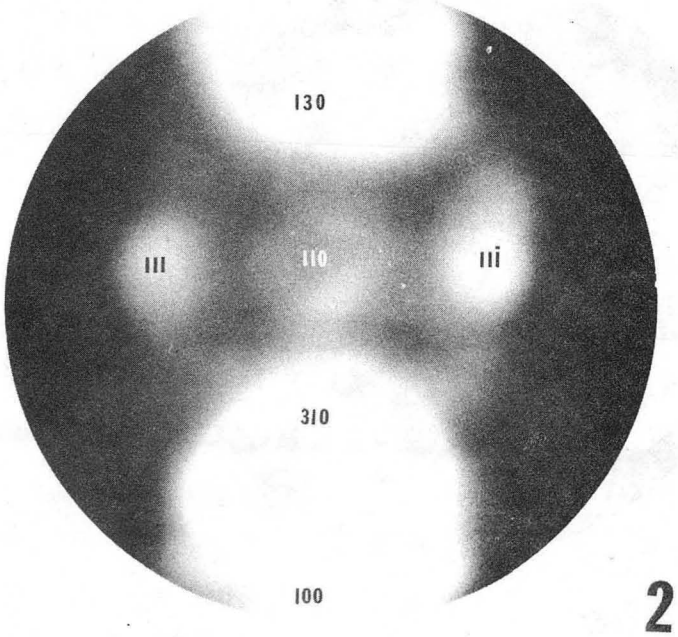

2

XBB 743-1600

Fig. 15.

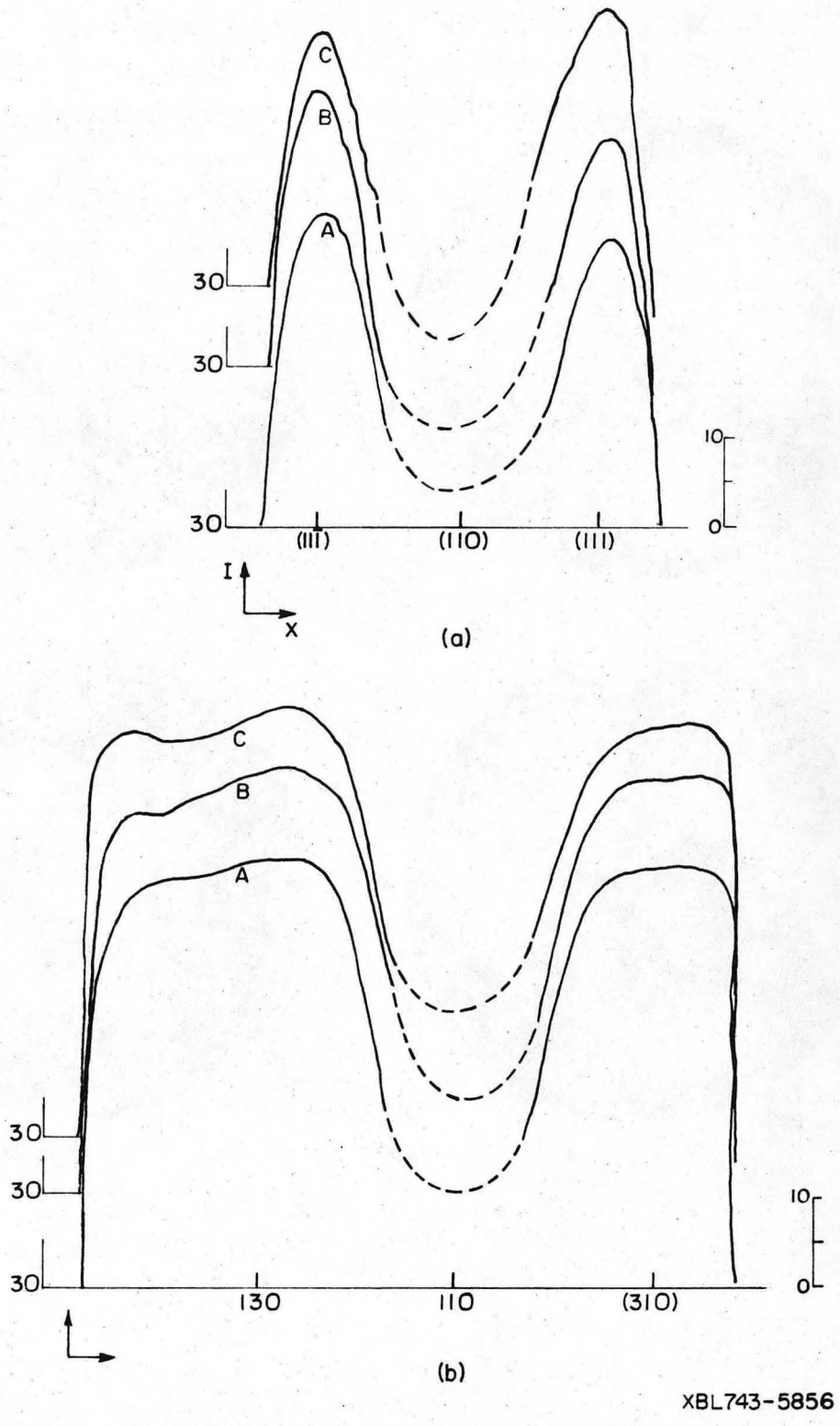
C
B
A
30
30
30
10
0
(111)
(110)
(111)
I
X
(a)
C
B
A
30
30
30
10
0
130
110
(310)
(b)
XBL743-5856

Fig. 16.

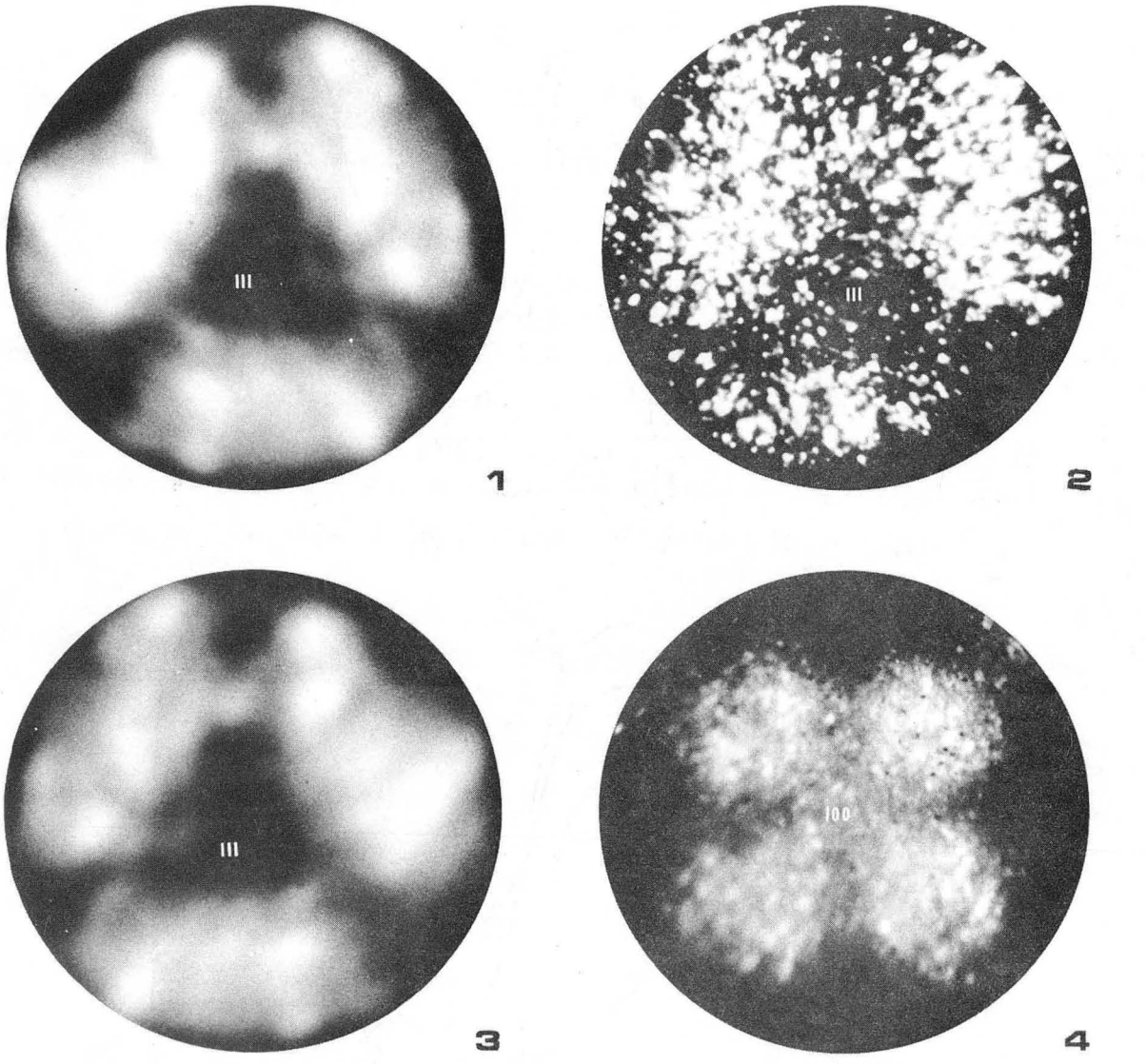

XBB 742-1158

Fig. 17.

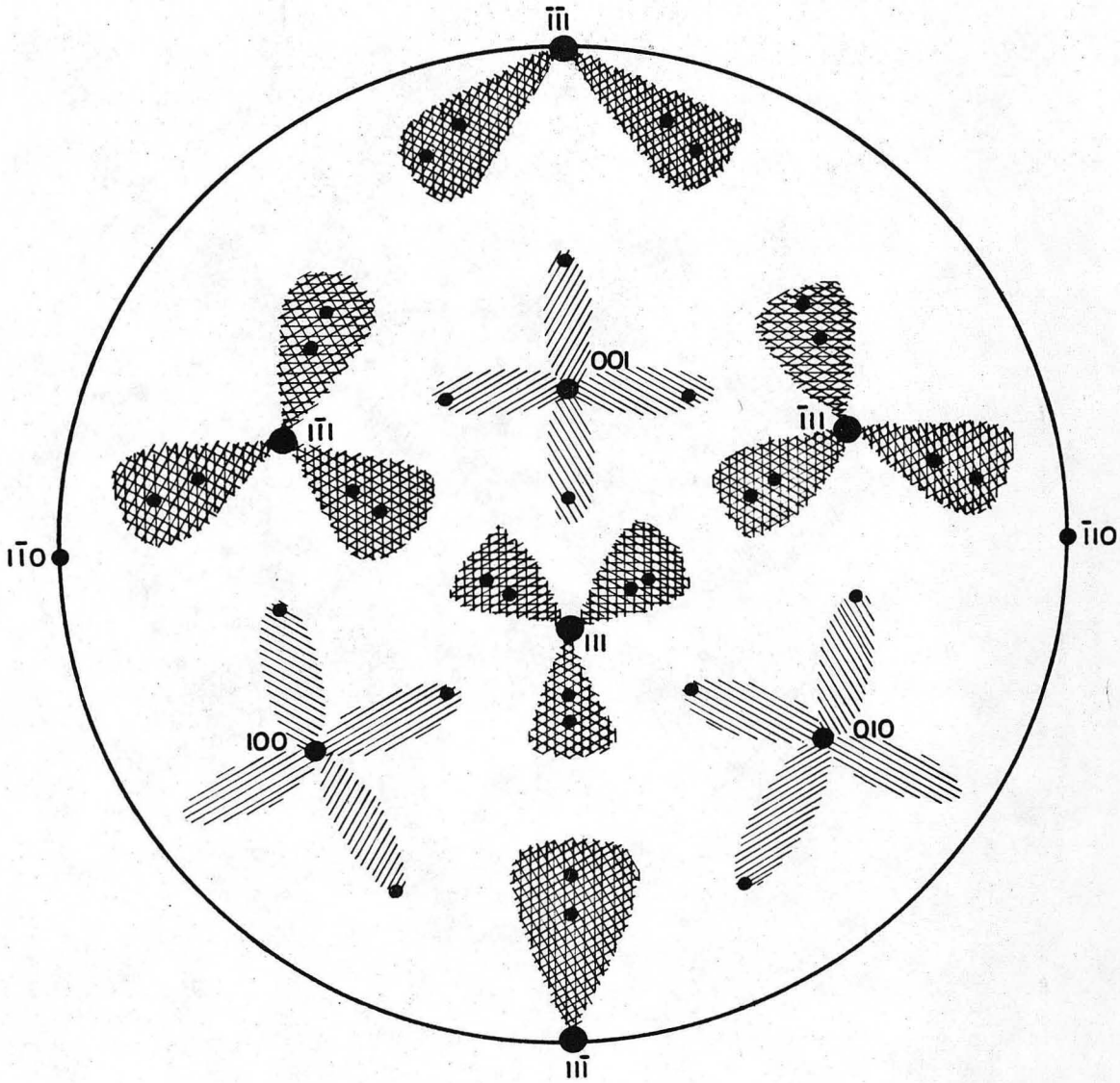

XBL 7012-7372

Fig. 18.

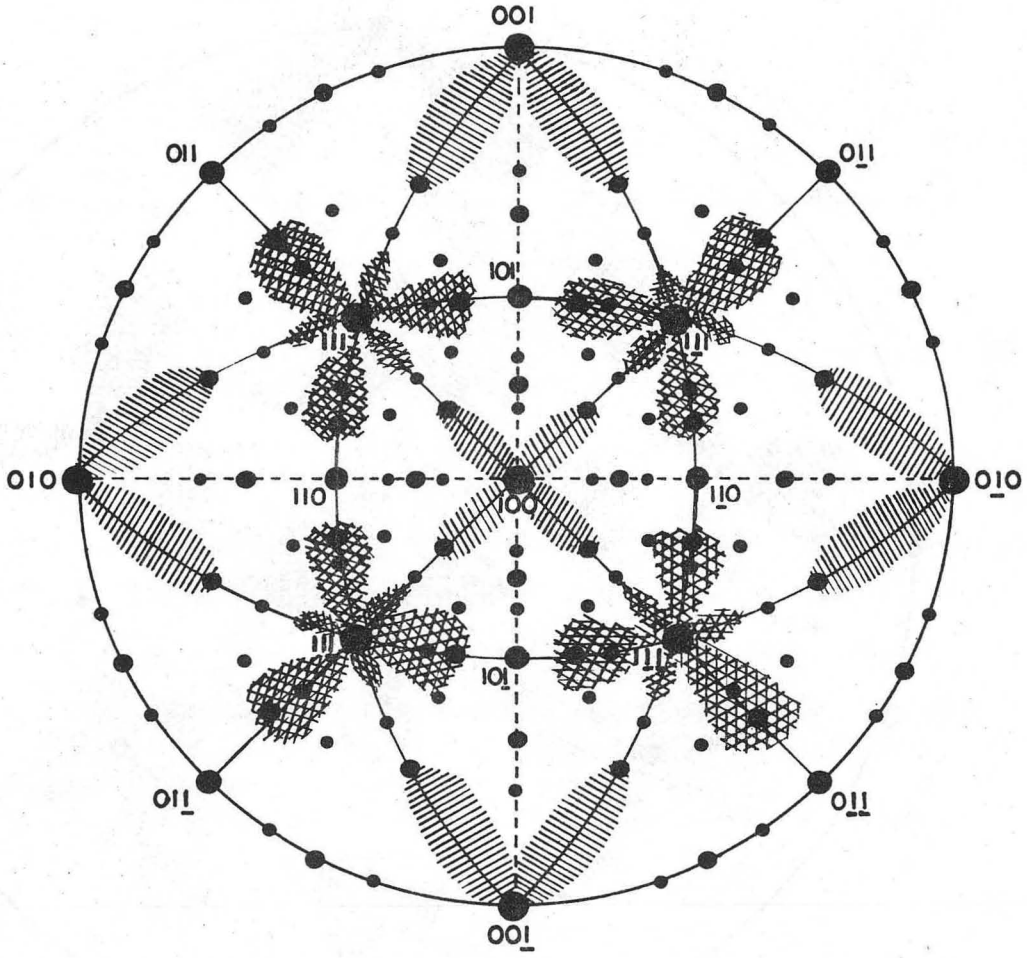

XBL 7012-7371

Fig. 19.

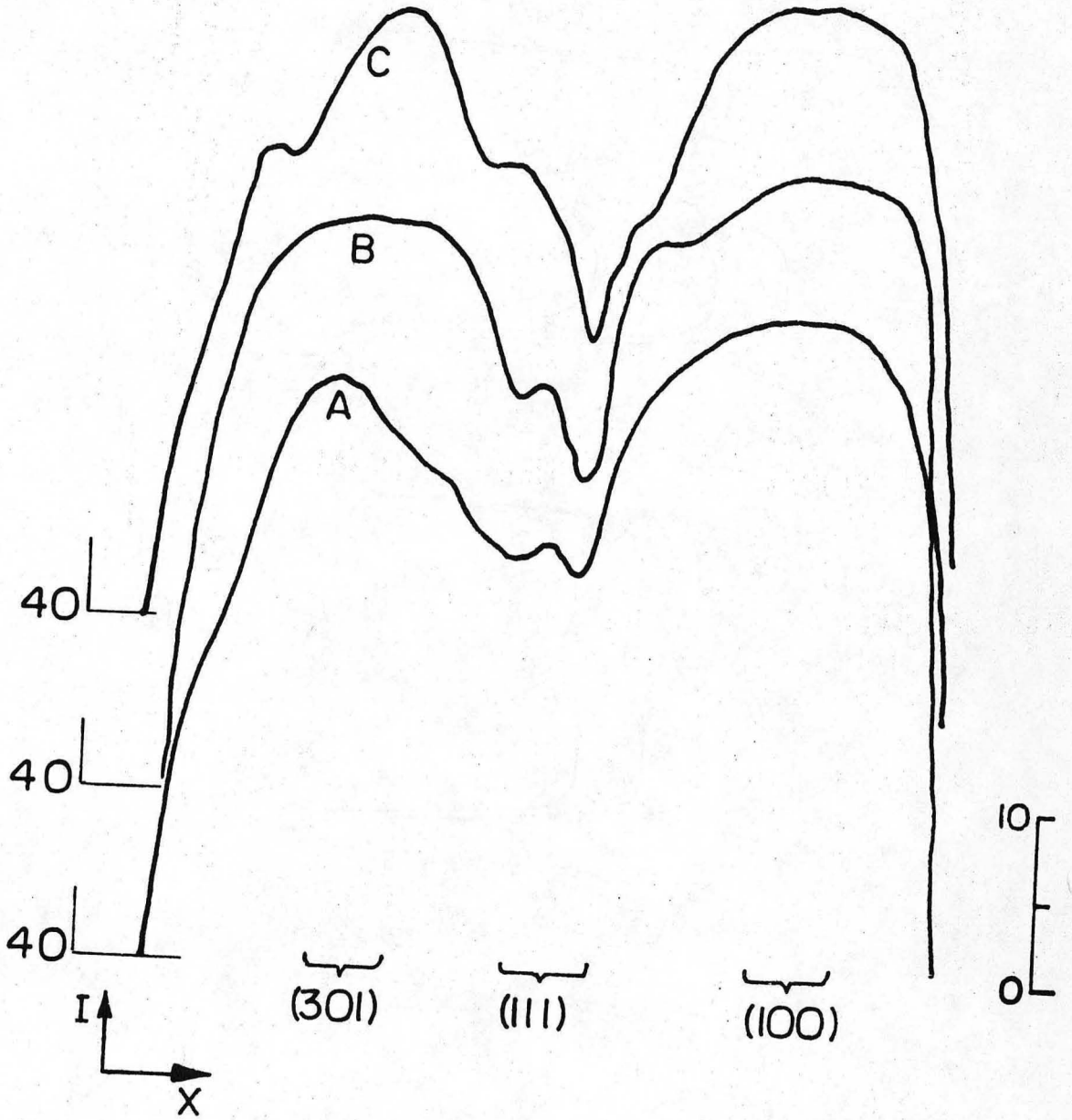

Fig. 20.

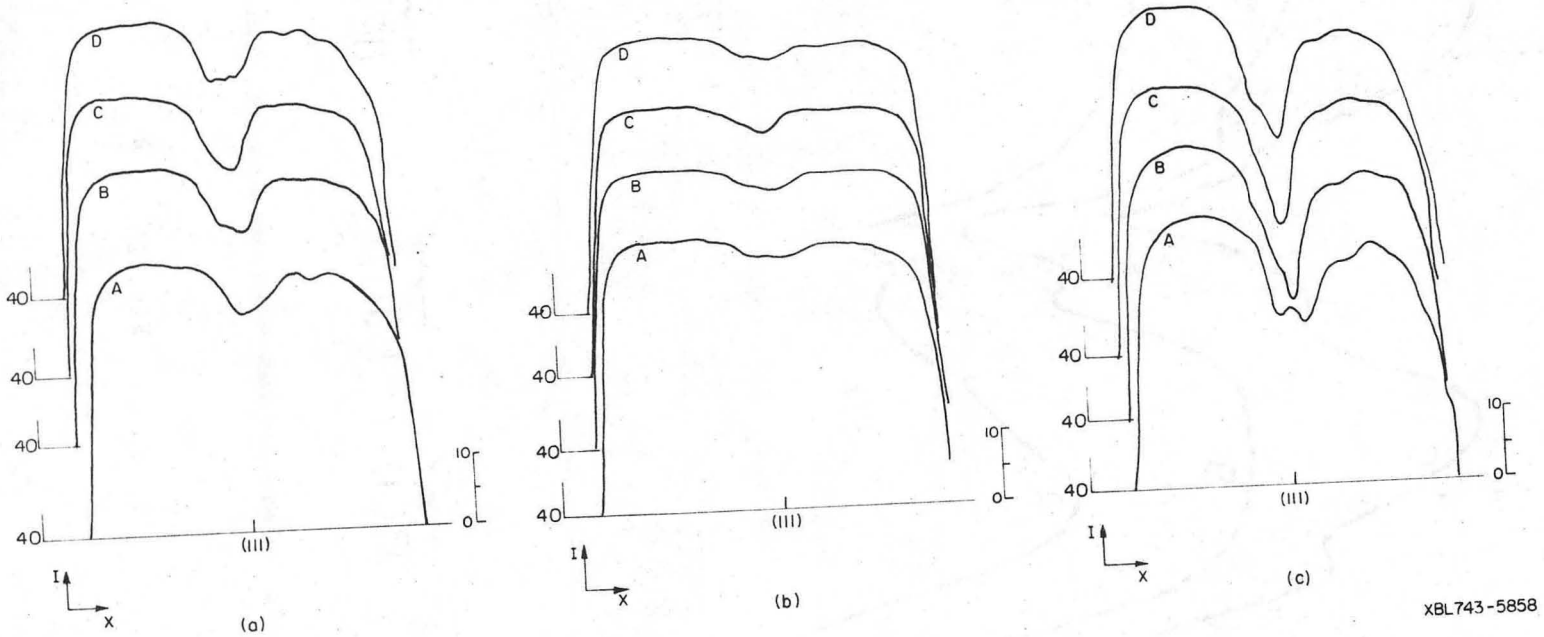
D
C
B
A
40
40
40
40
10
0
(III)
I
X
(a)
D
C
B
A
40
40
40
10
0
(III)
I
X
(b)
D
C
B
A
40
40
40
10
0
(III)
I
X
(c)
XBL743-5858

Fig. 21.

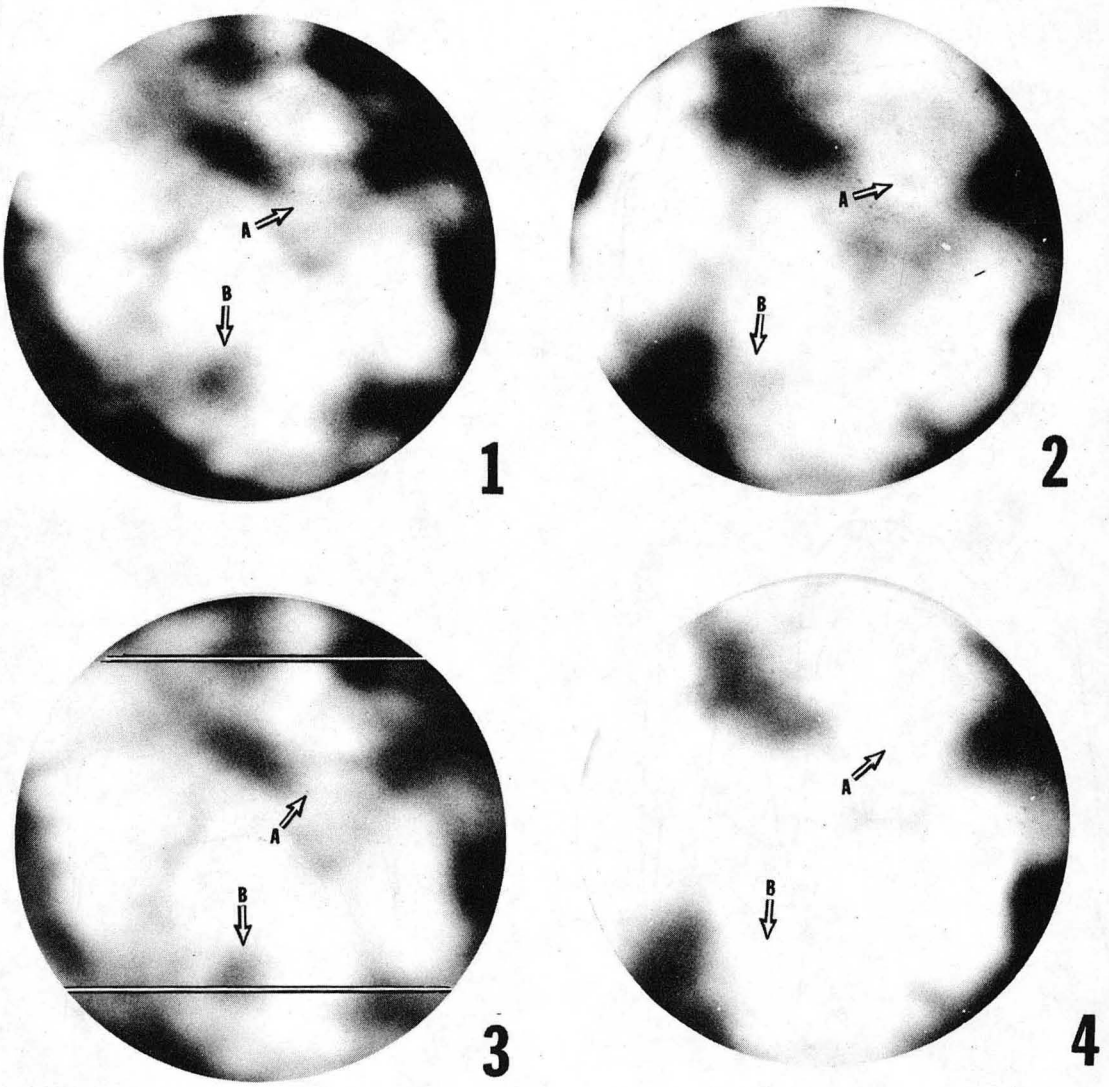

XBB 743-1599

Fig. 22.

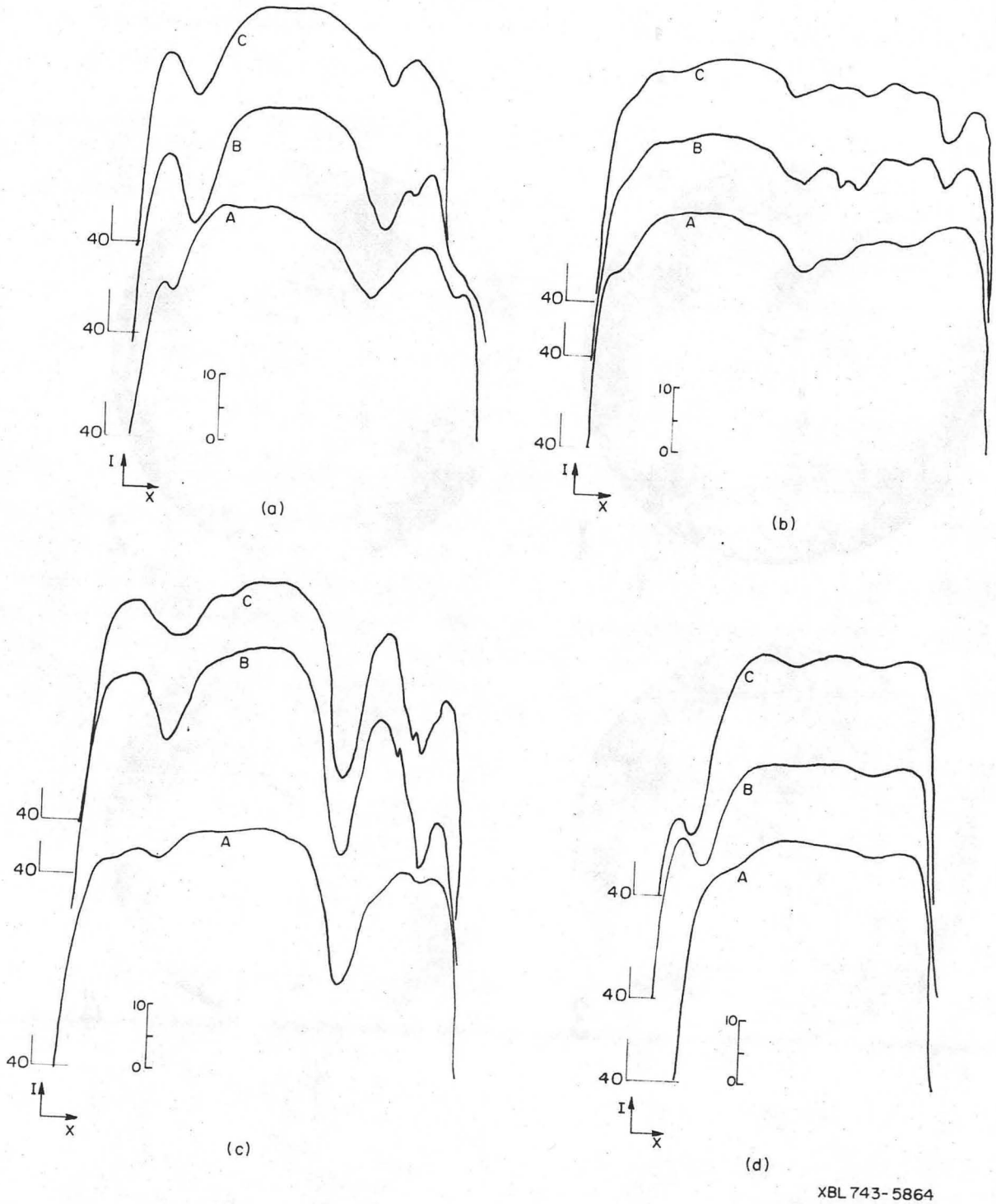
C
B
A
40
40
40
10
0
I
X
(a)
C
B
A
40
40
40
10
0
I
X
(b)
C
B
A
40
40
40
10
0
I
X
(c)
C
B
A
40
40
40
10
0
I
X
(d)
XBL 743-5864

Fig. 23.

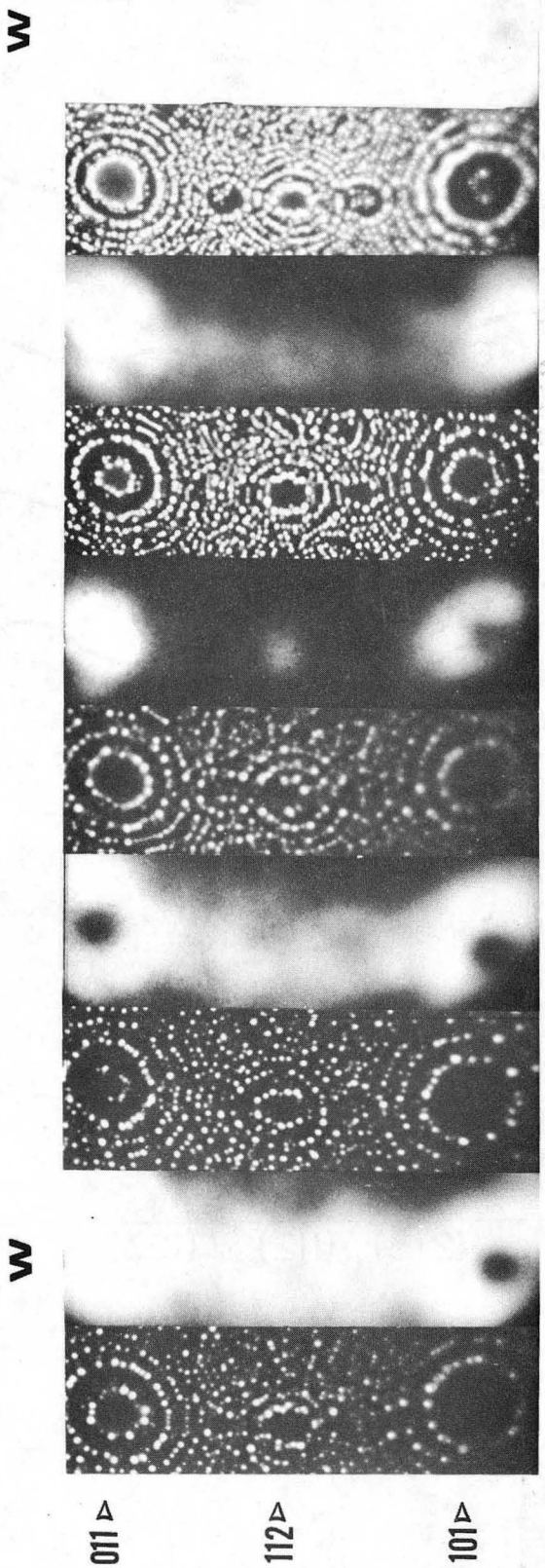

XBB 742-1151

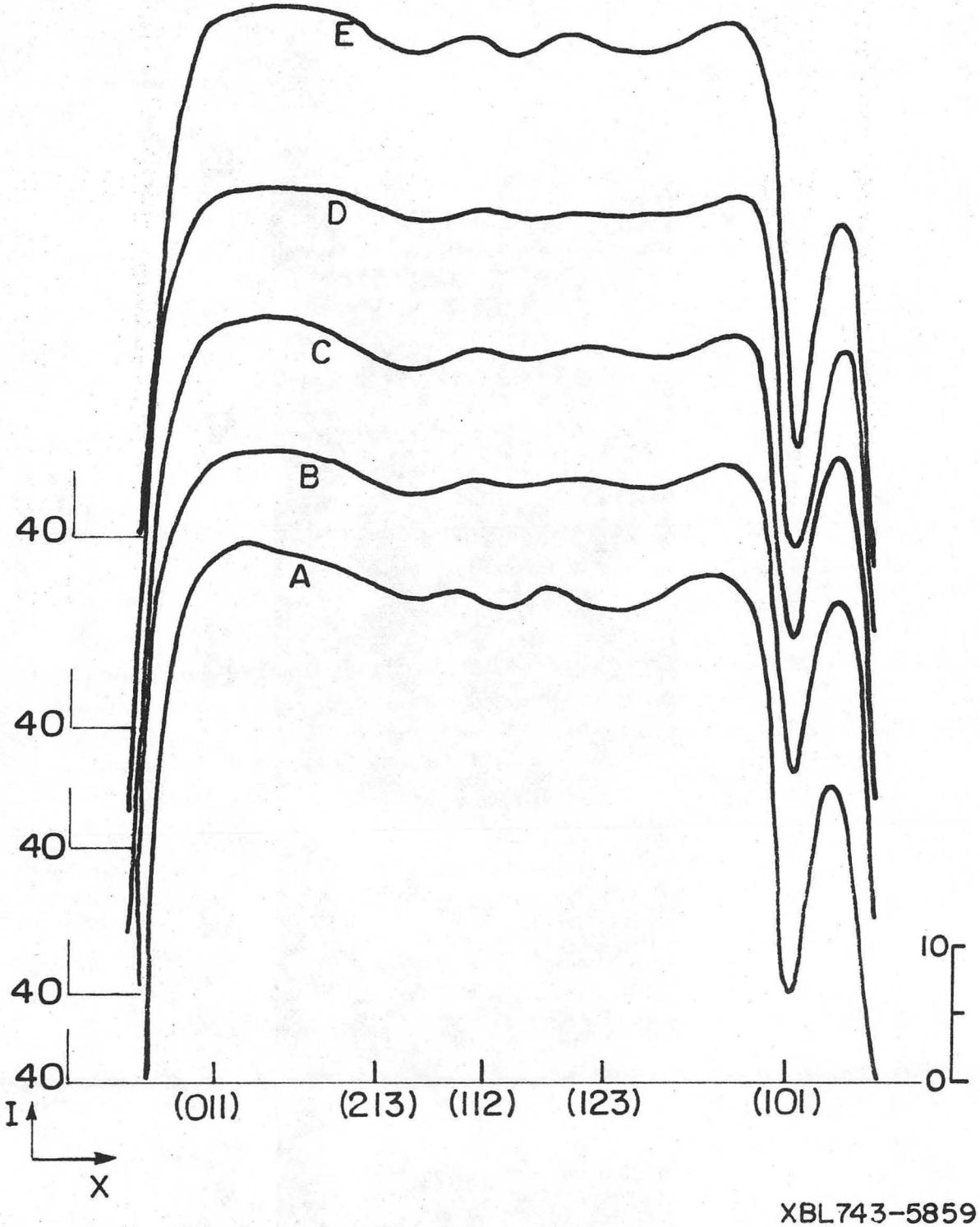

Fig. 25.

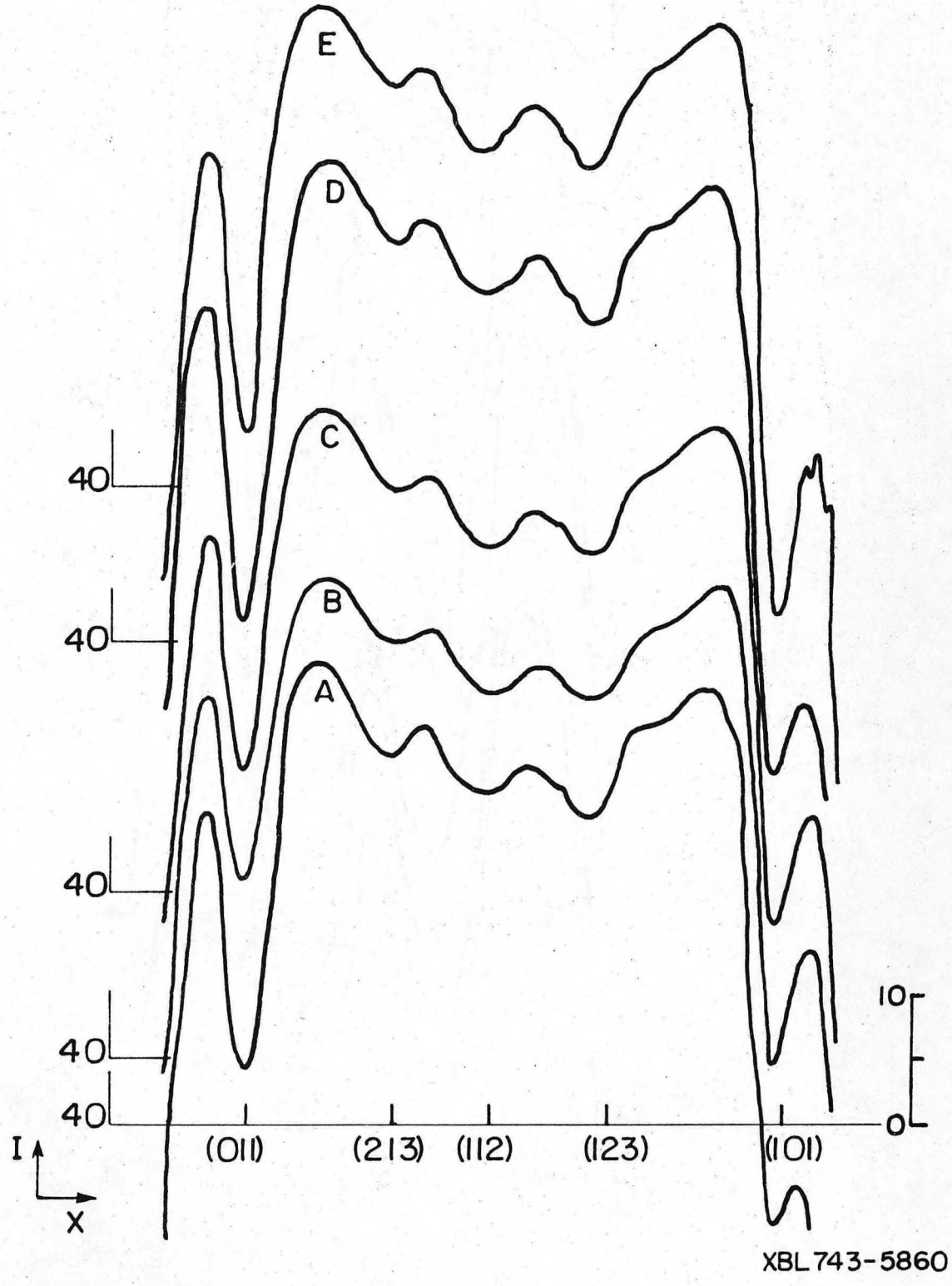

Fig. 26.

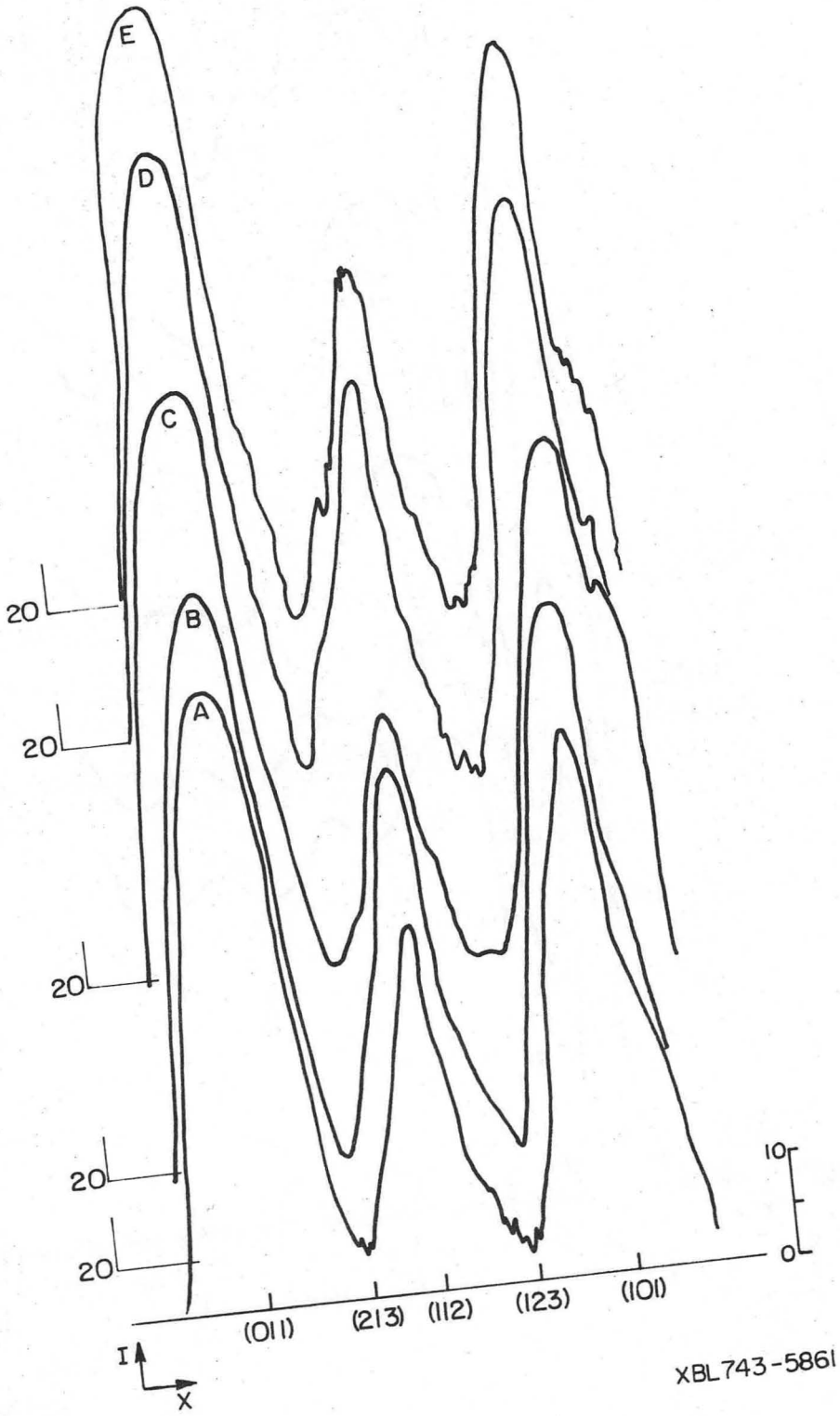

Fig. 27.

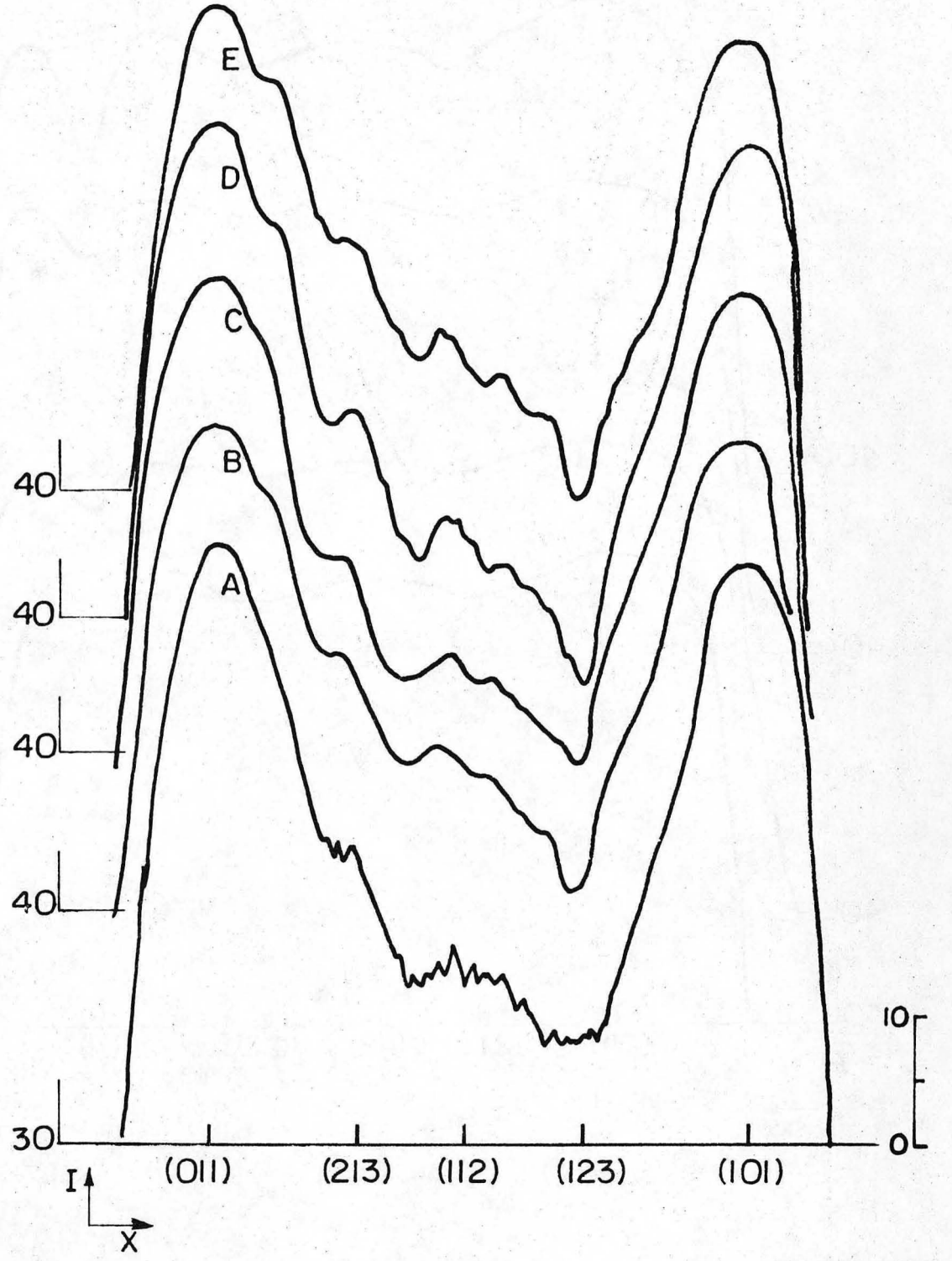

Fig. 28.

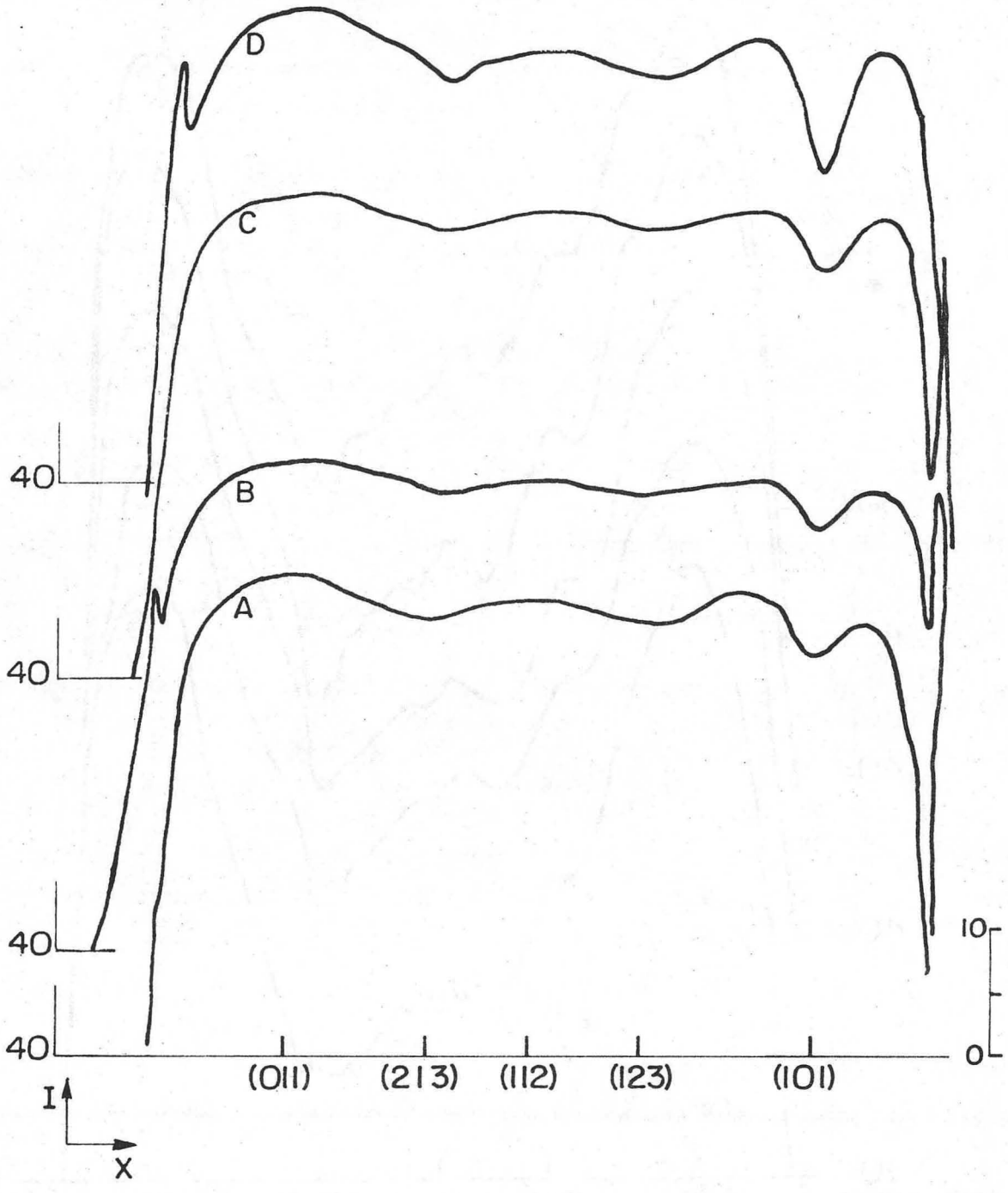

Fig. 29.

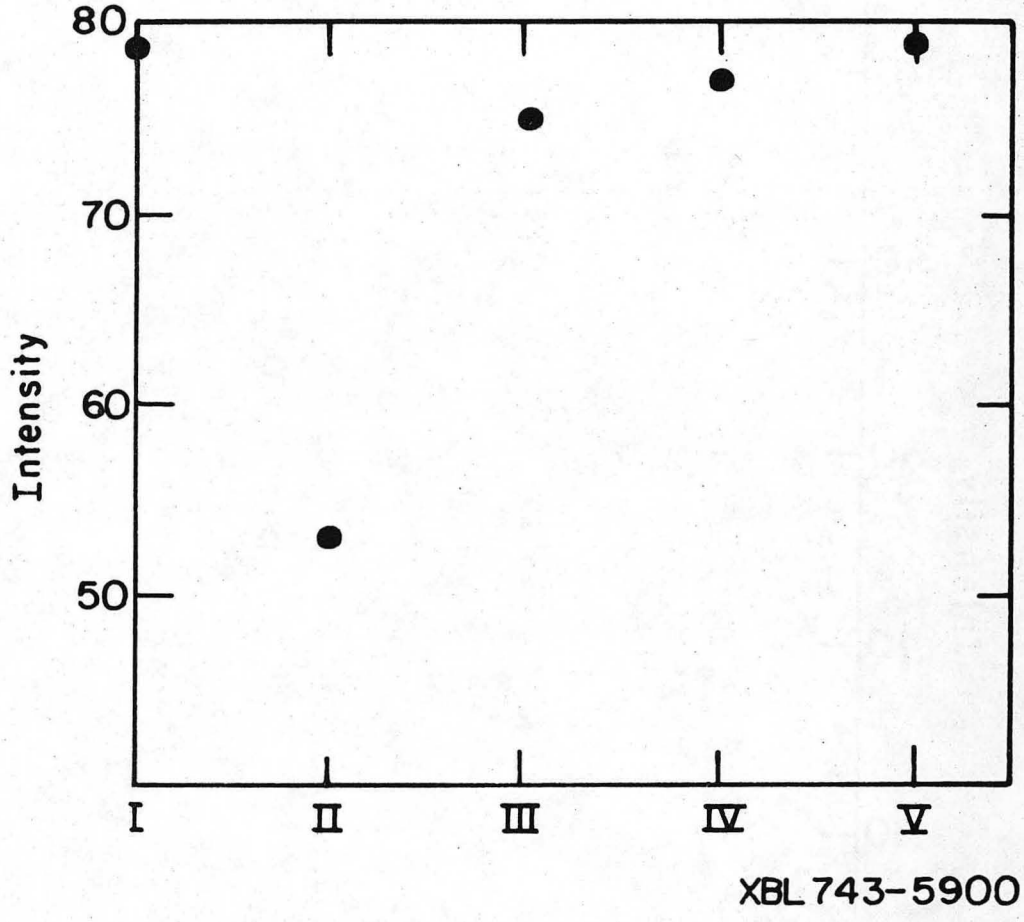

Fig. 30.

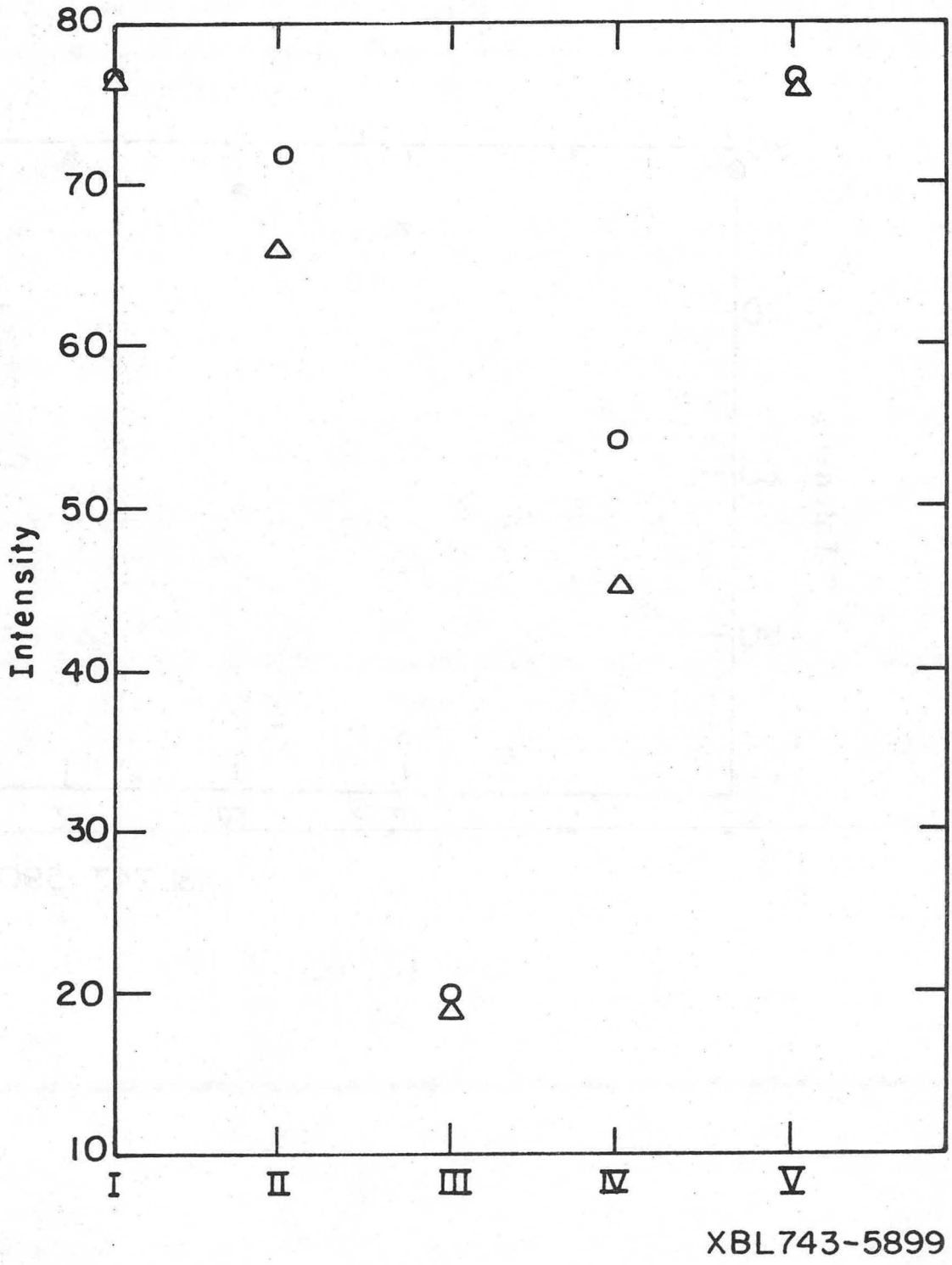

Fig. 31.

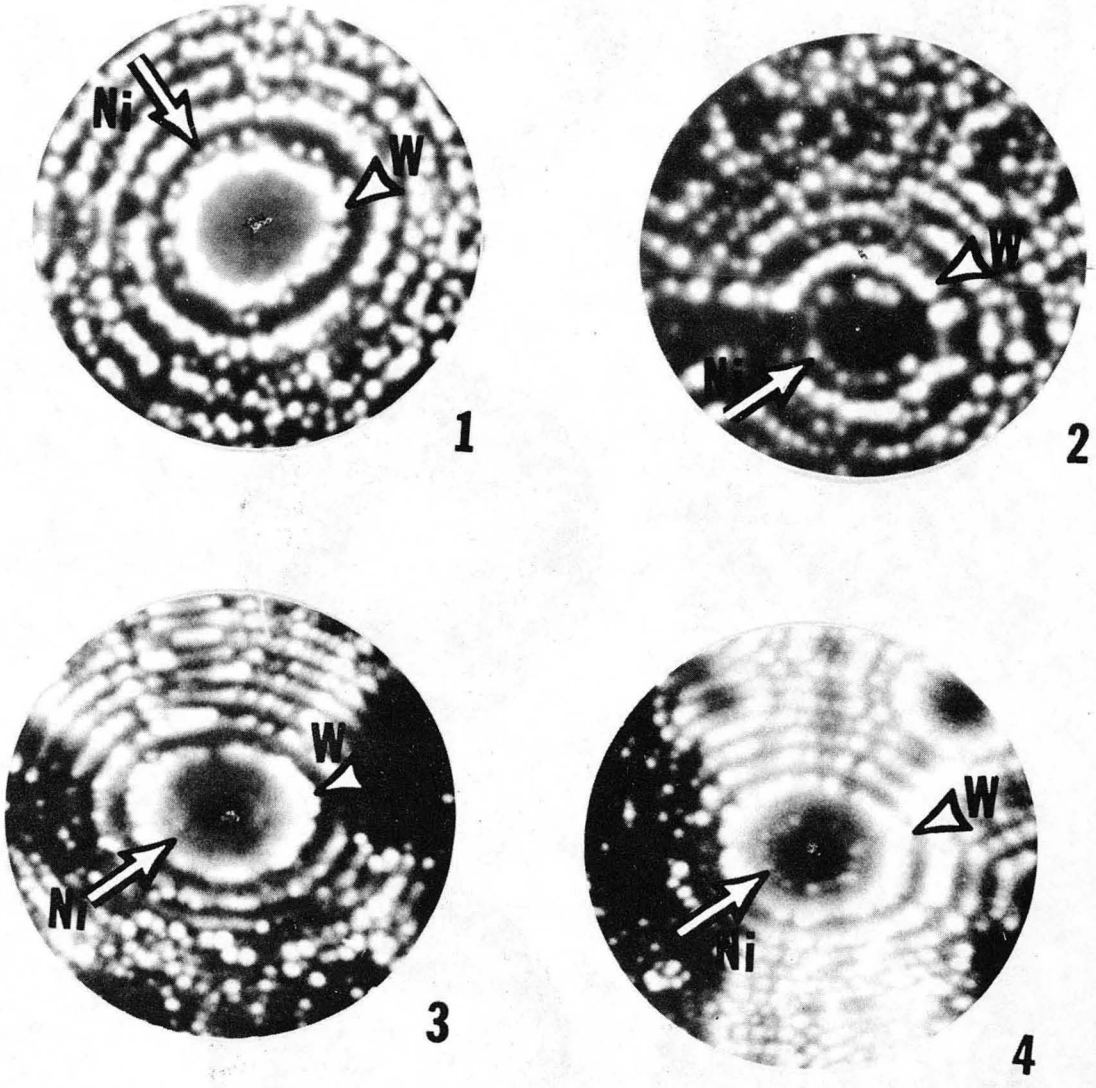

XBB 743-1601

Fig. 32.

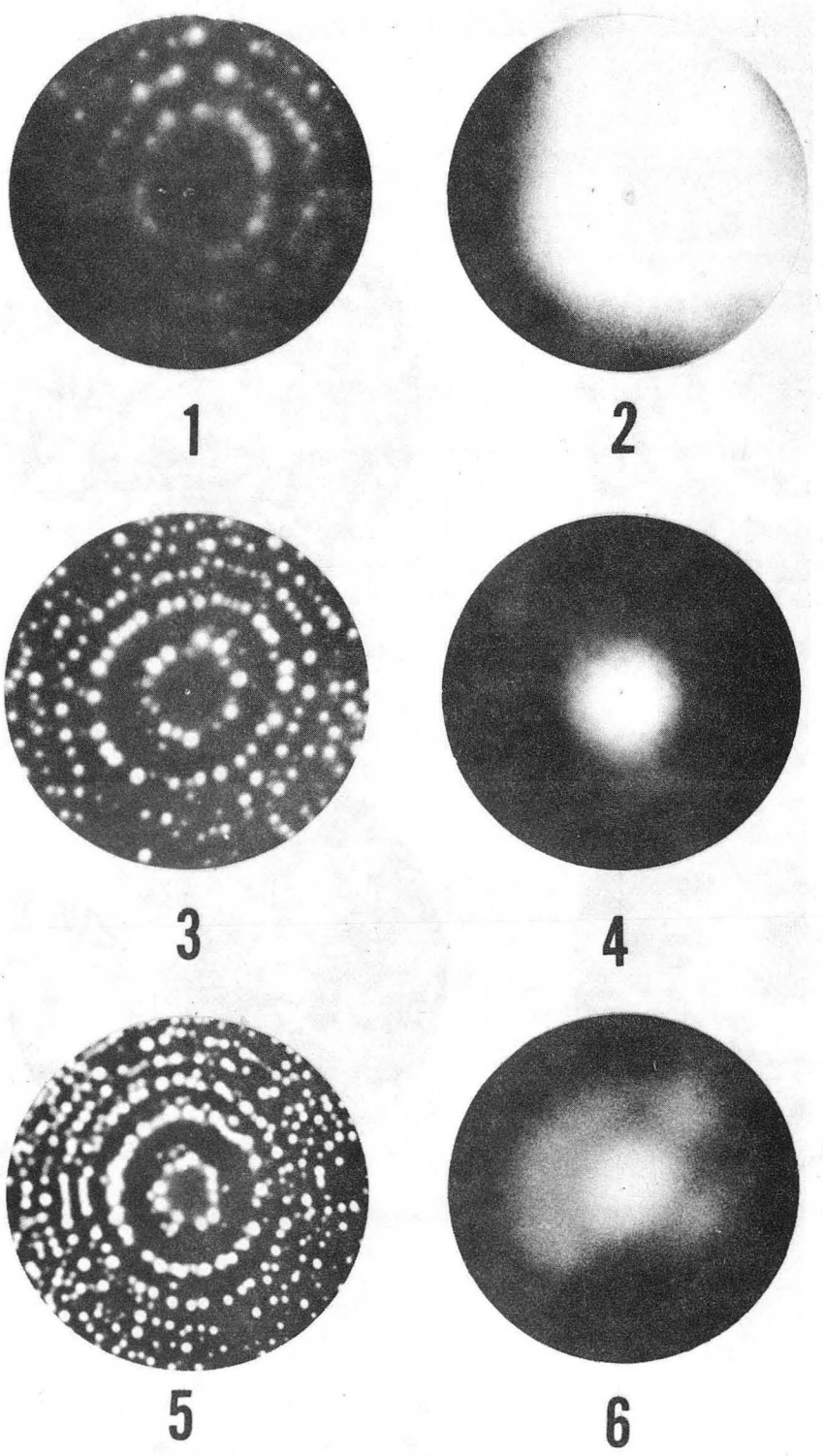

Fig. 33.

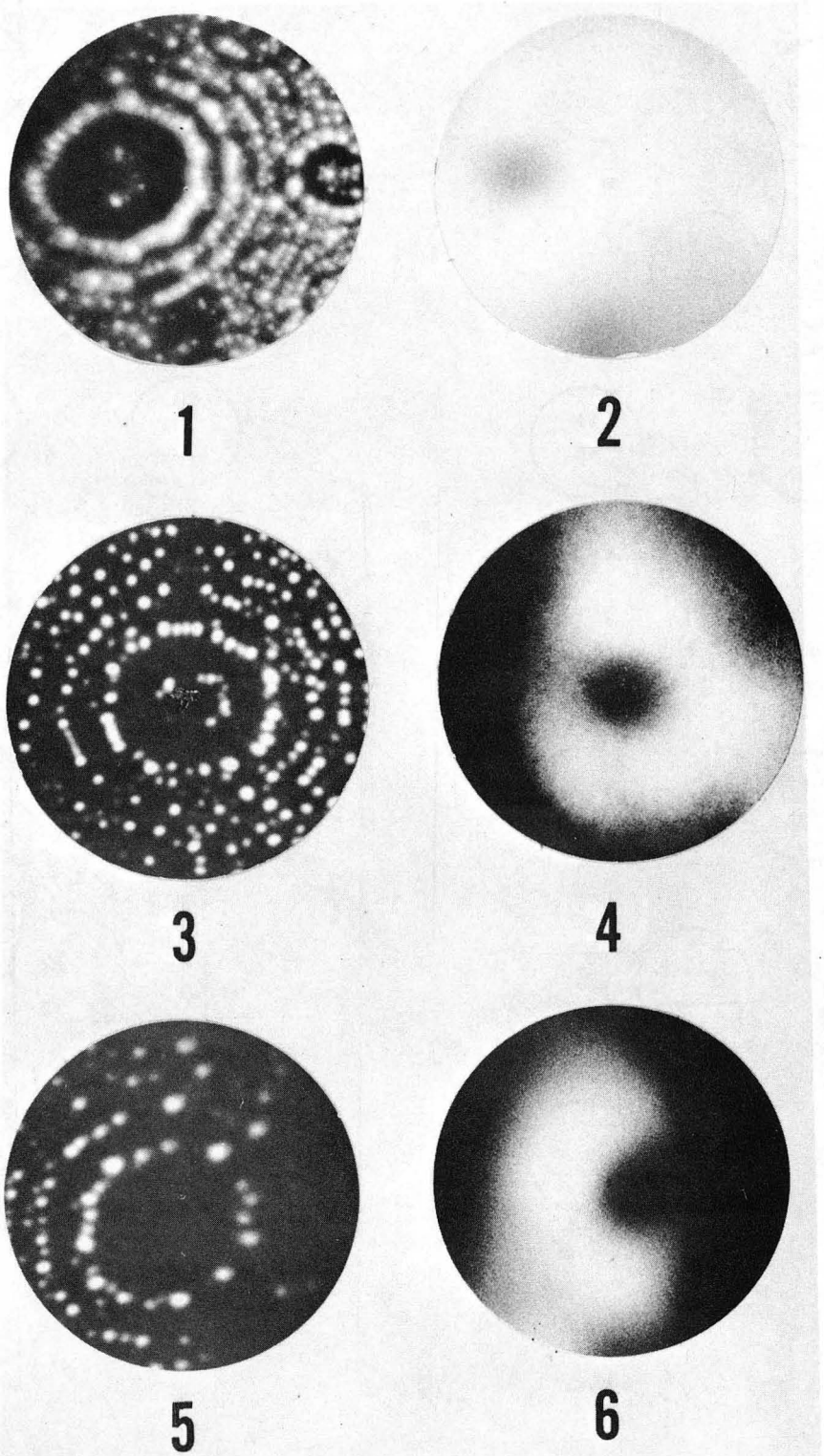

XBB 742-1153

Fig. 34.

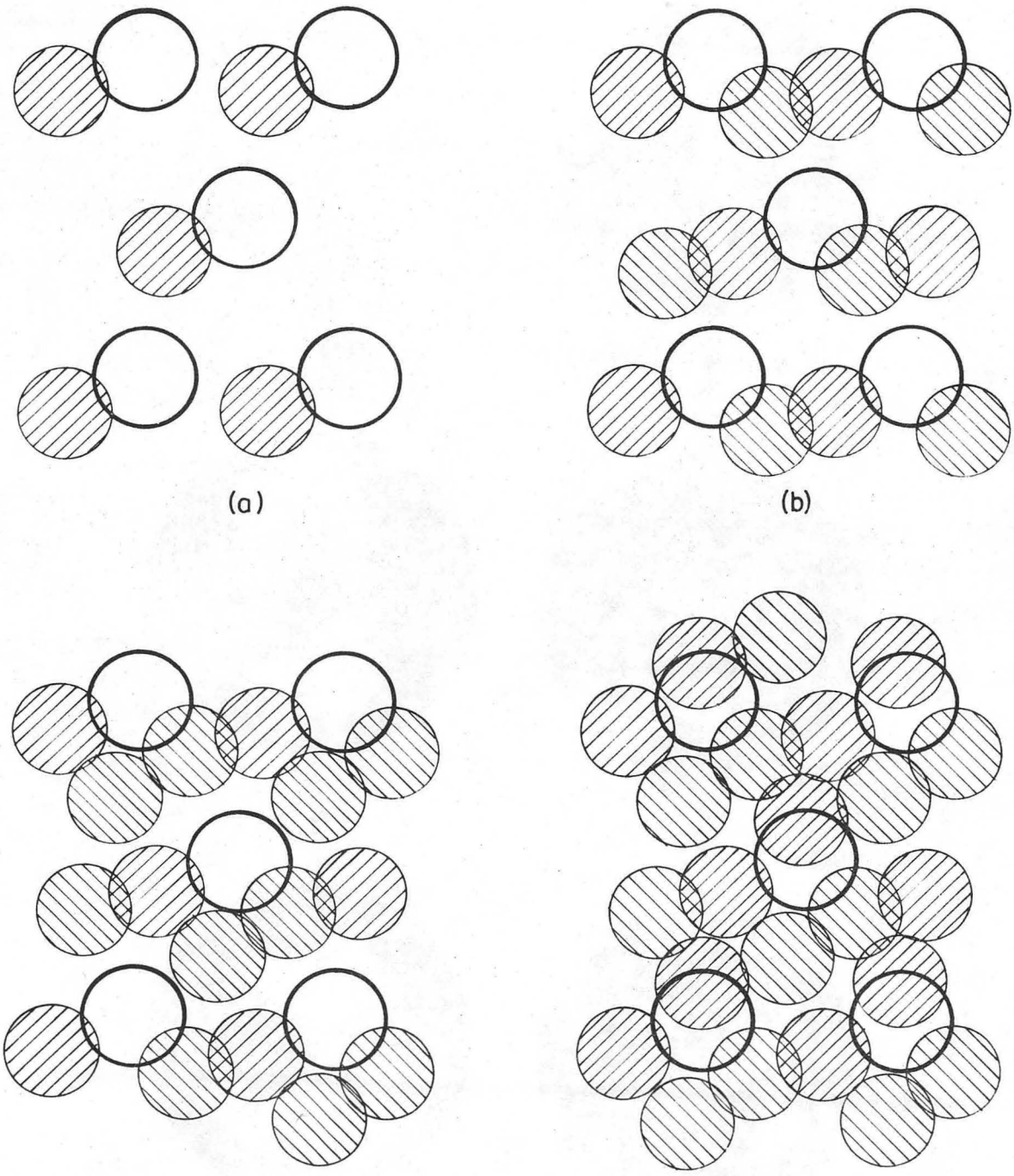

Fig. 35.

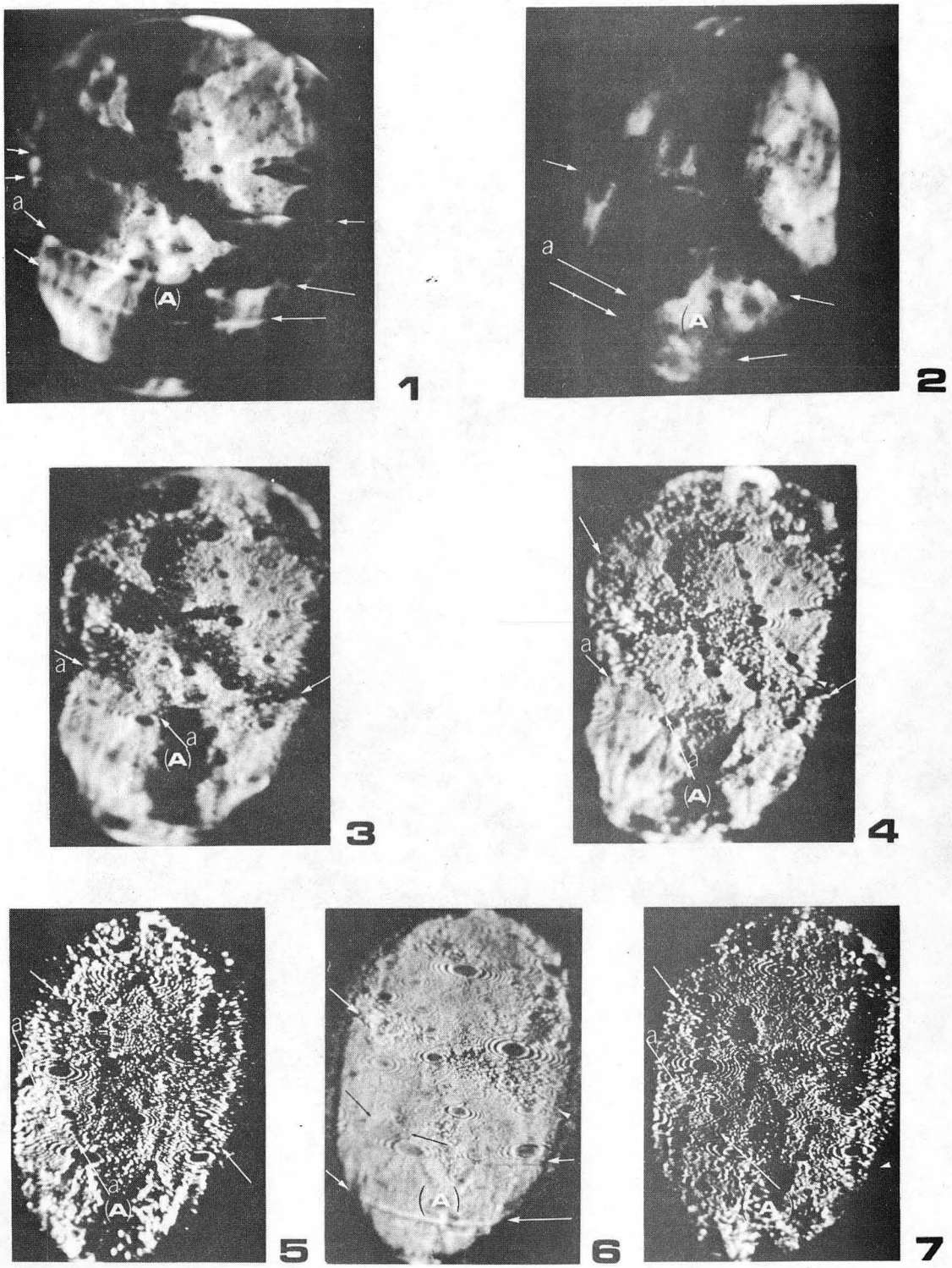

XBB 742-1156

Fig. 36.

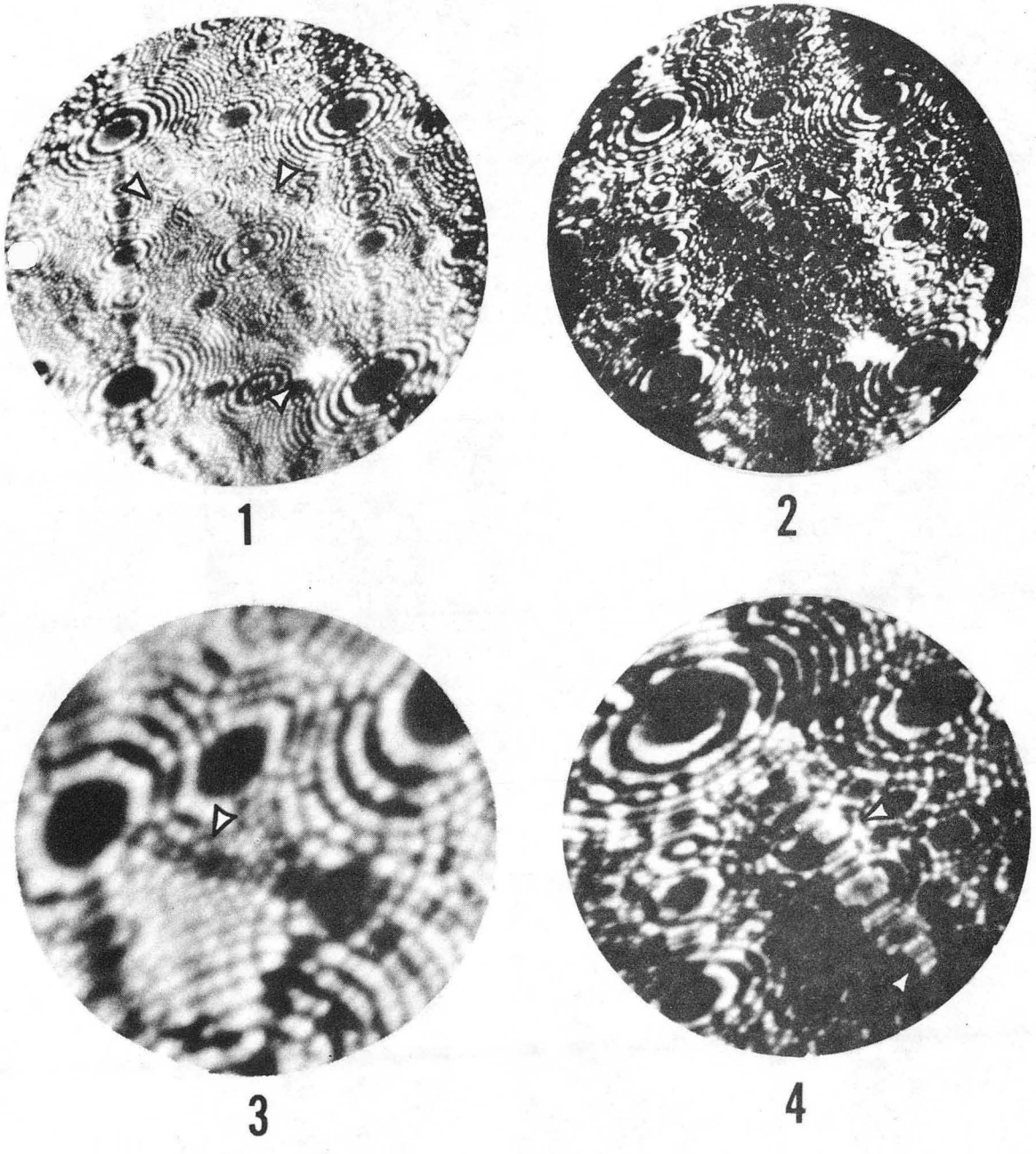

Fig. 37.

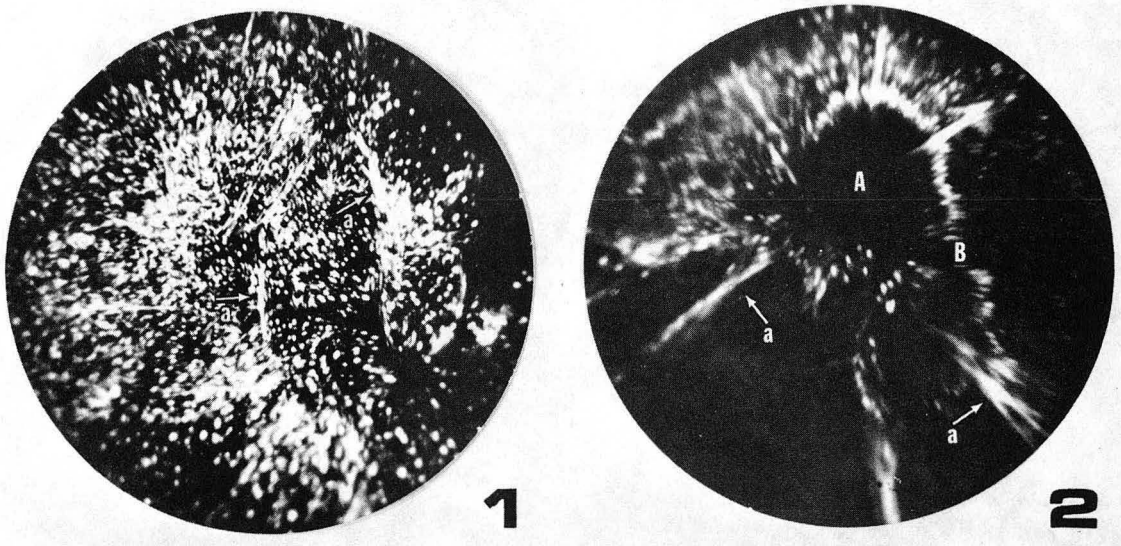

XBB 743-1717

Fig. 38.

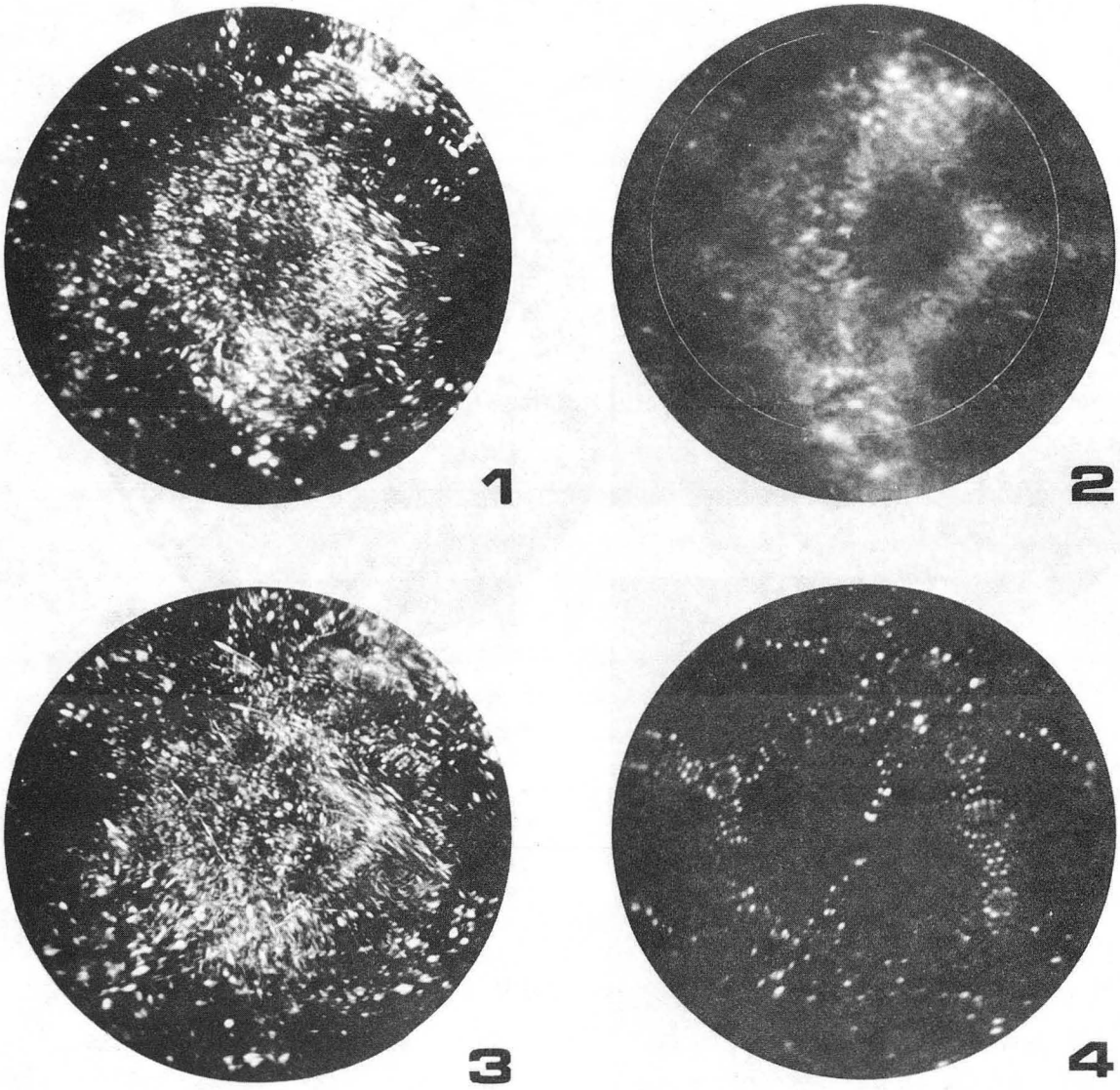

XBB 742-1155

Fig. 39.

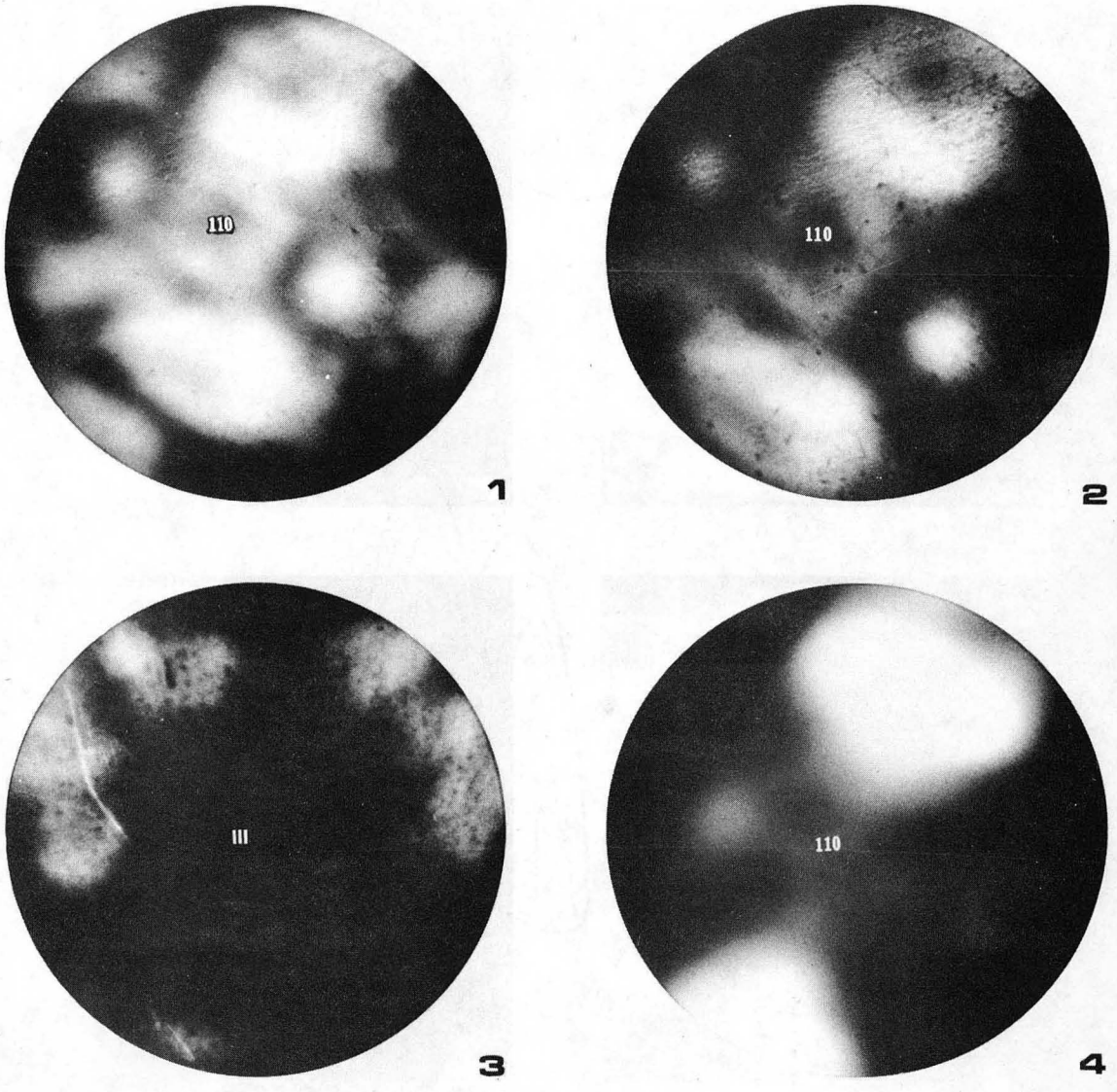

XBB 742-1157

Fig. 40.

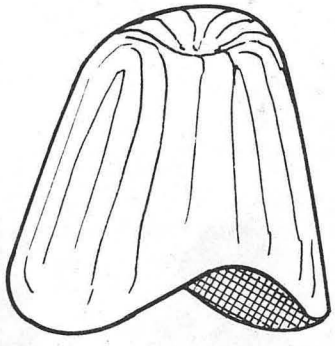

(a)

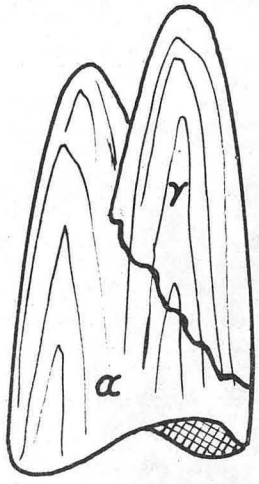

(b)

XBL 743-5846

Fig. 41.

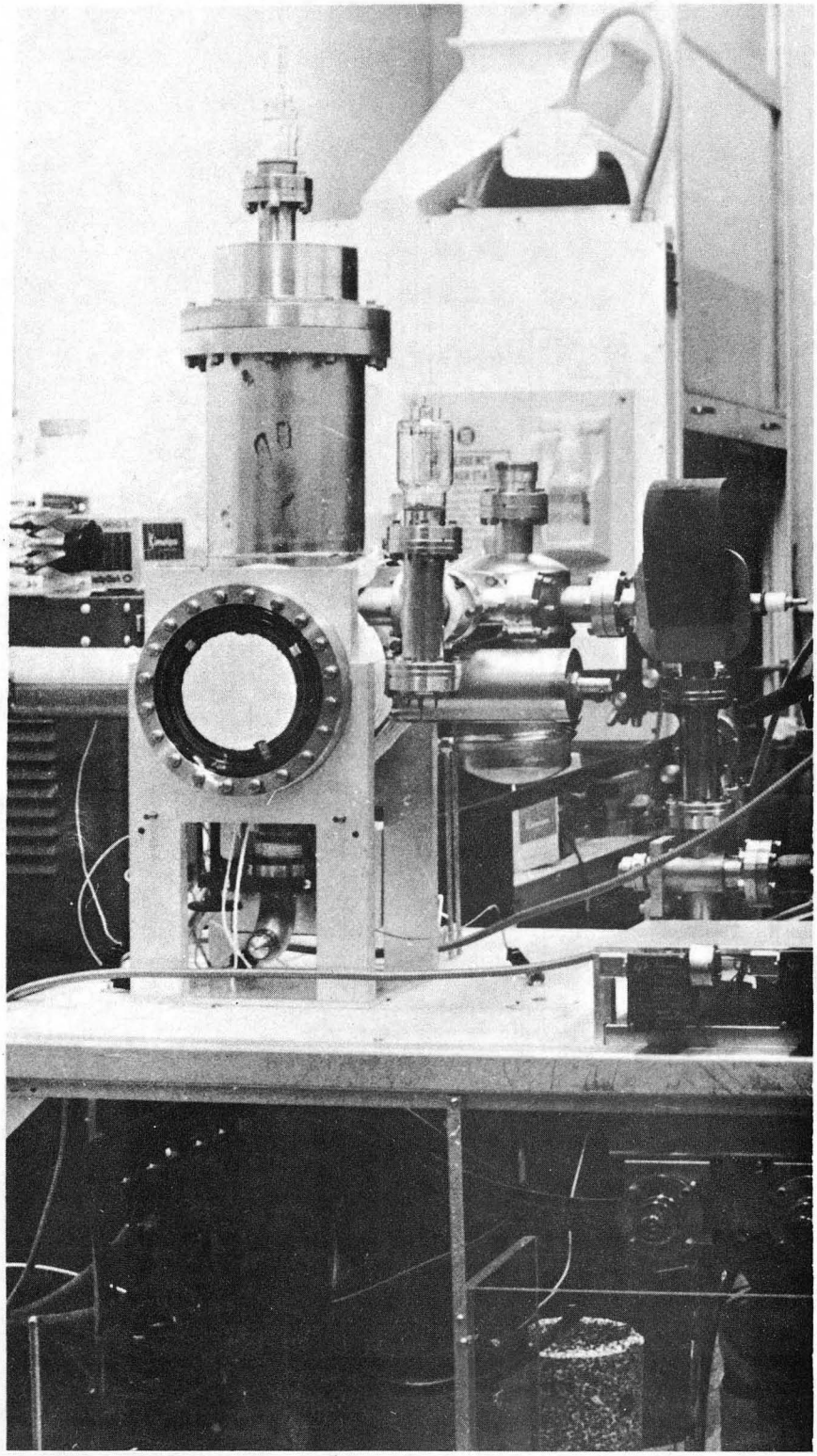

Fig. 42.

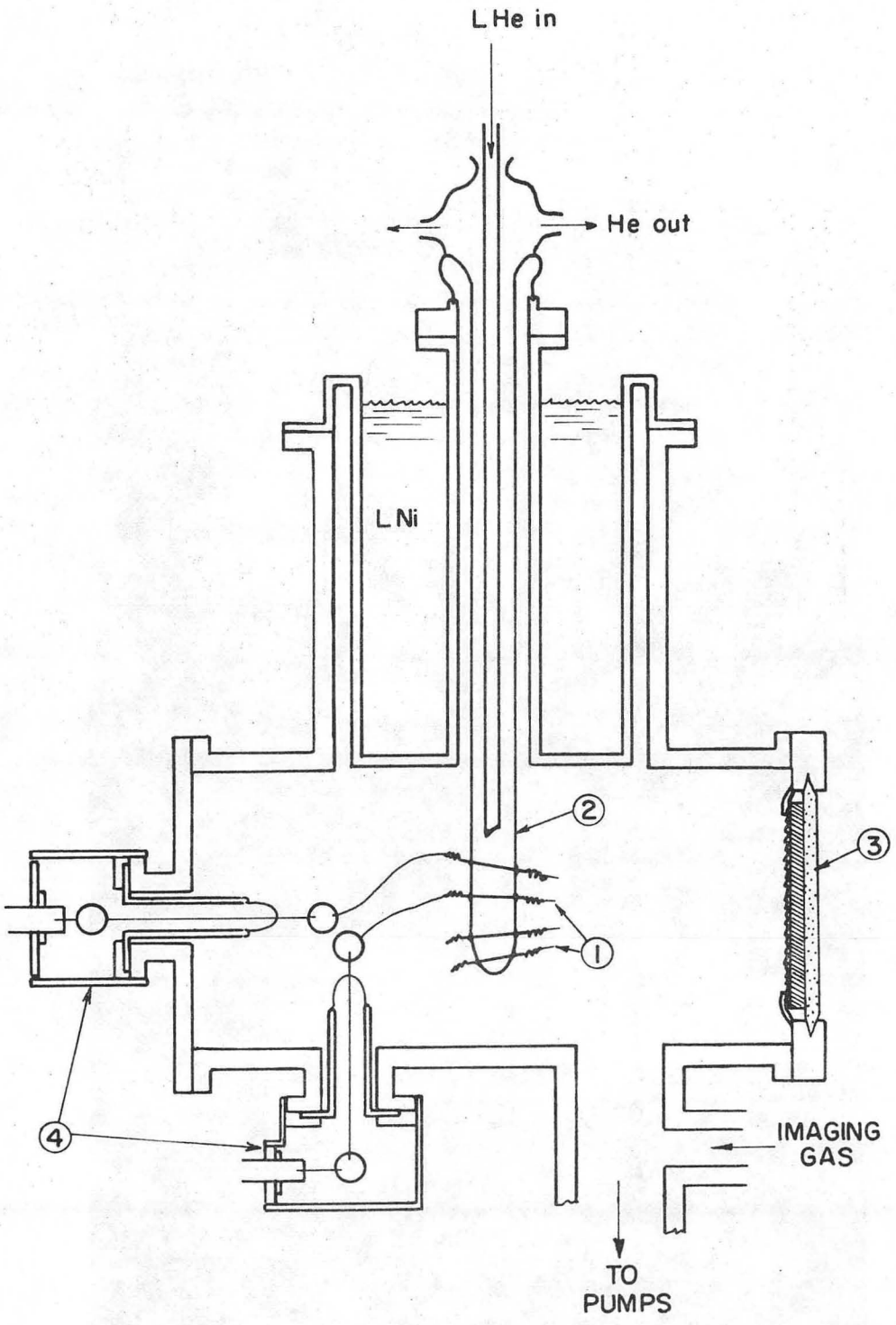

Fig. 43.

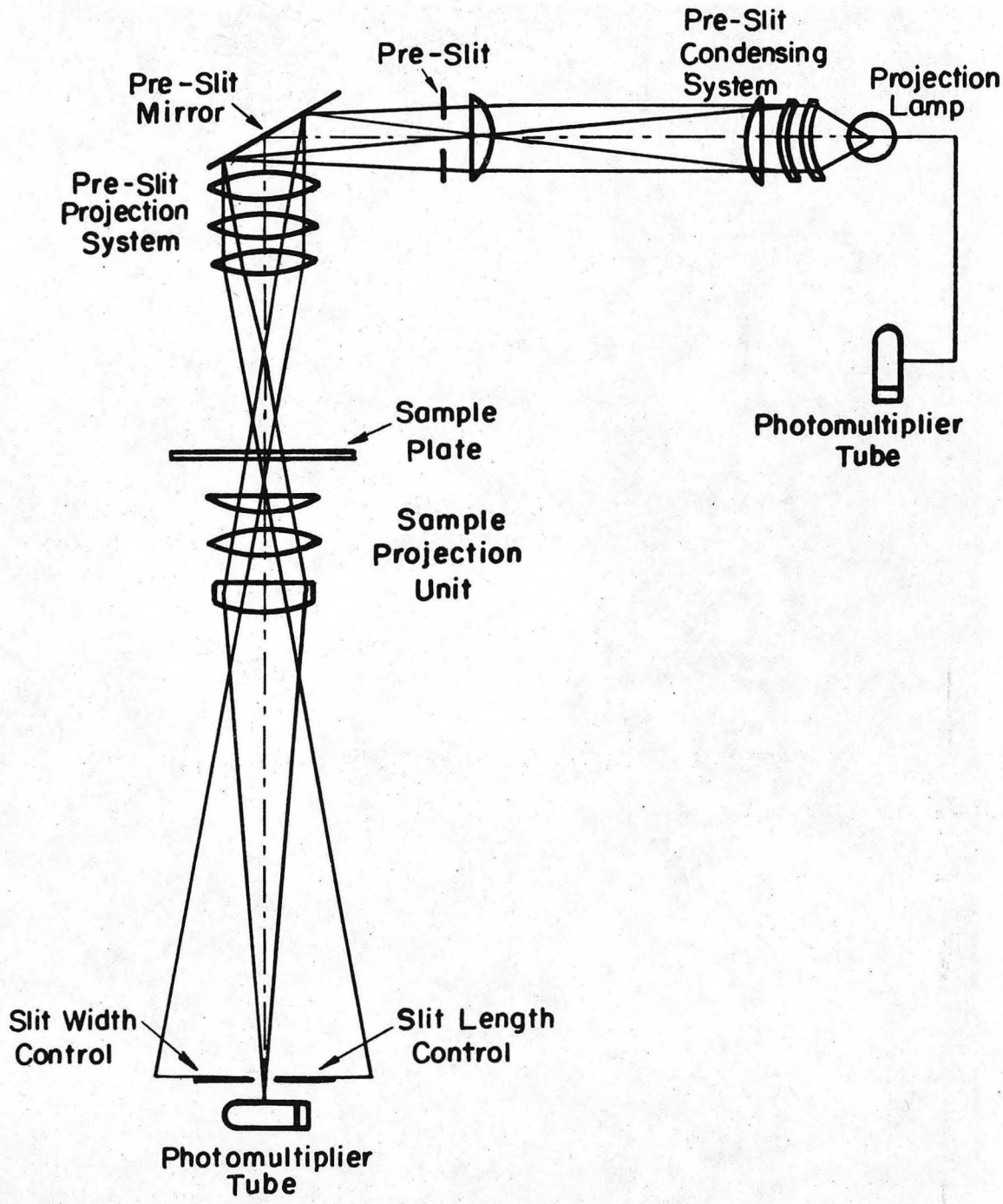

MICROPHOTOMETER OPTICAL SYSTEM

XBL743-5851

Fig. 44.

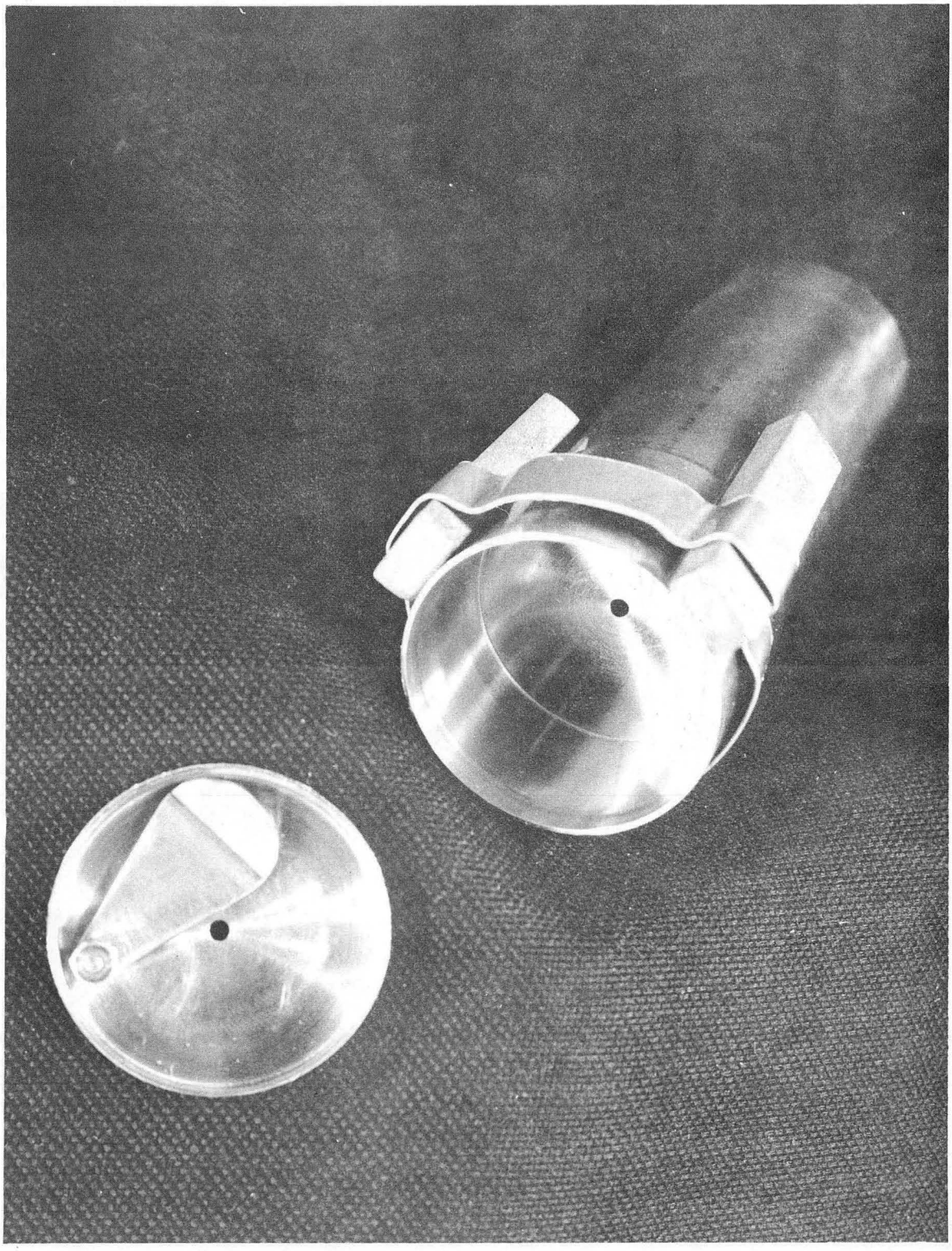

Fig. 45.

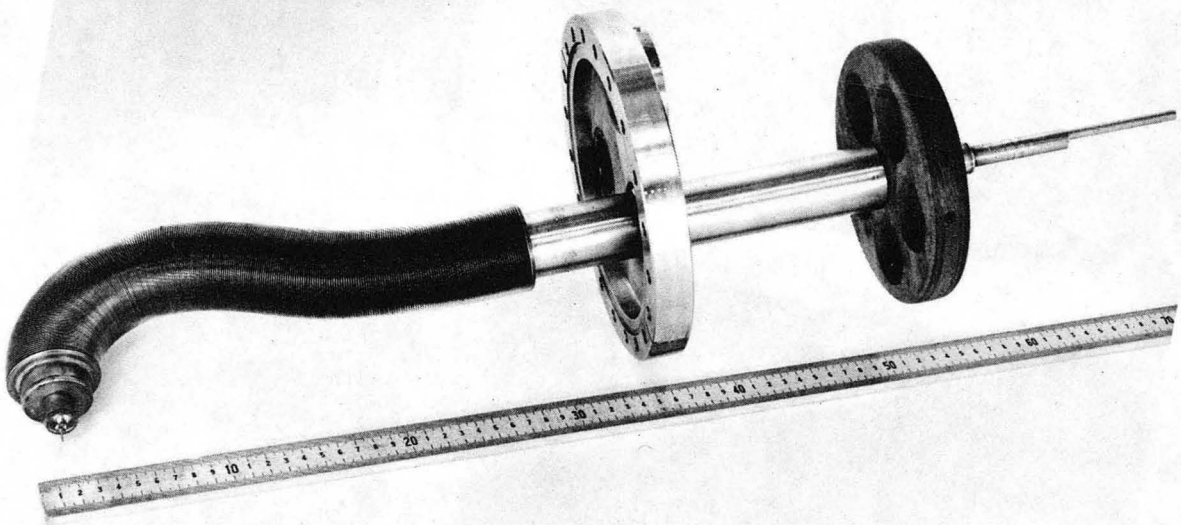

XBB 743-2060

Fig. 46.

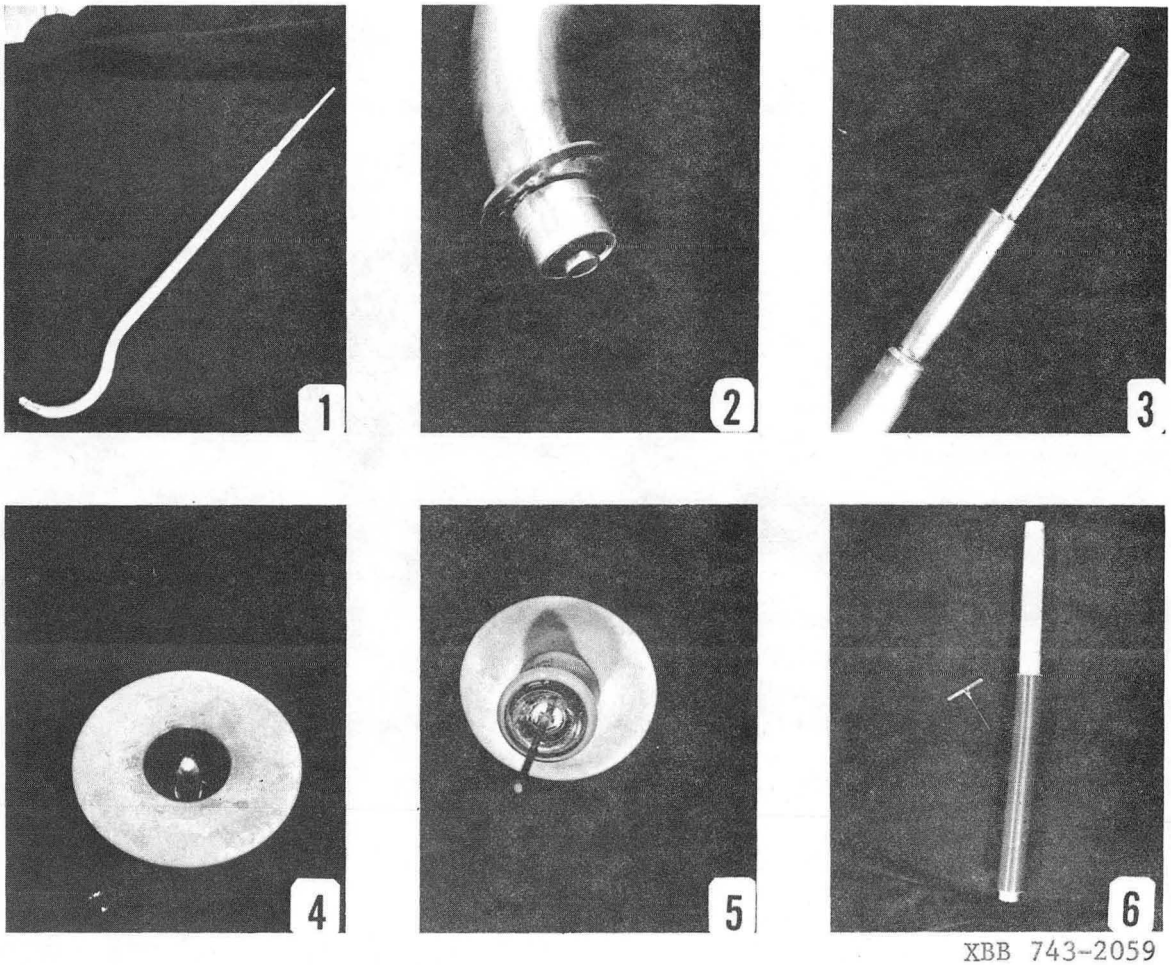

XBB 743-2059

Fig. 47.

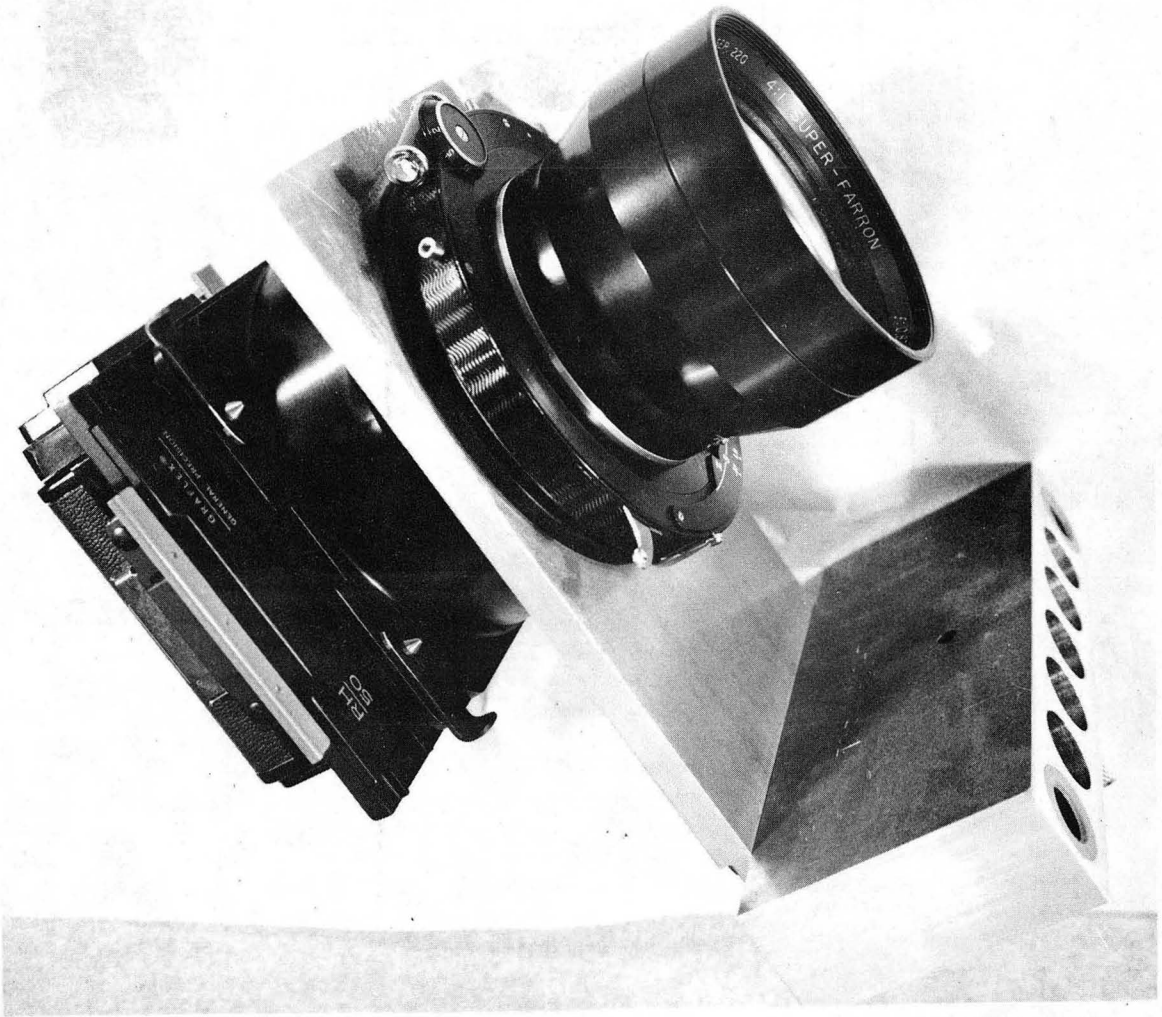

XBB 743-1857

Fig. 48.

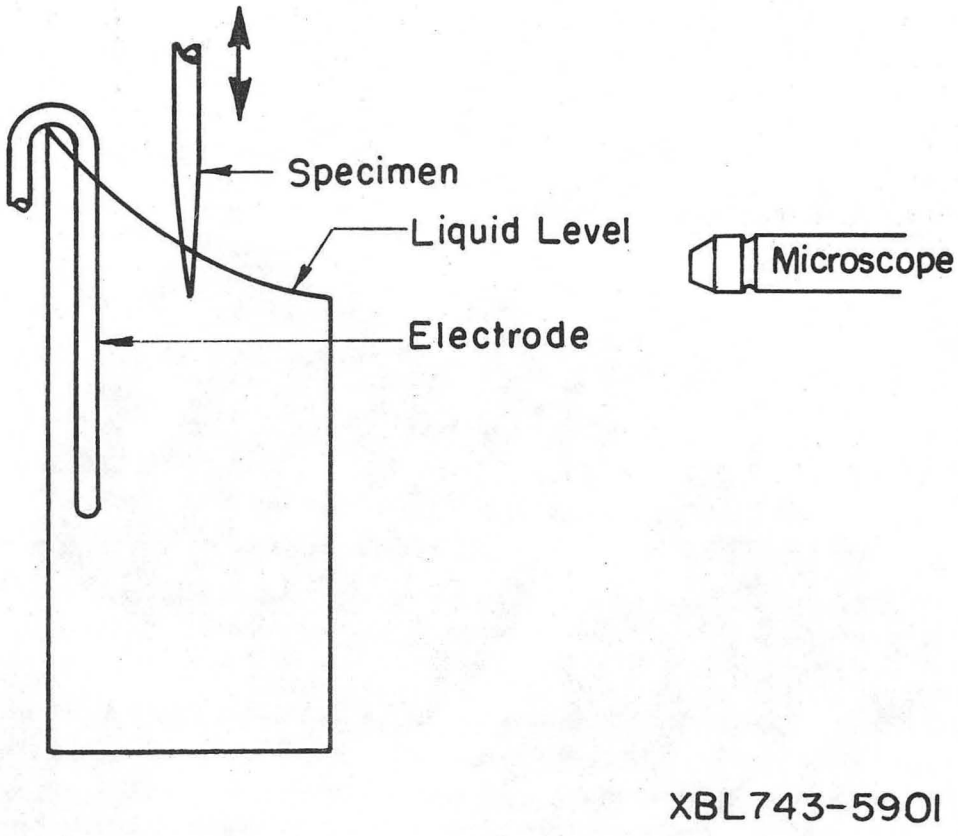

Fig. 49.

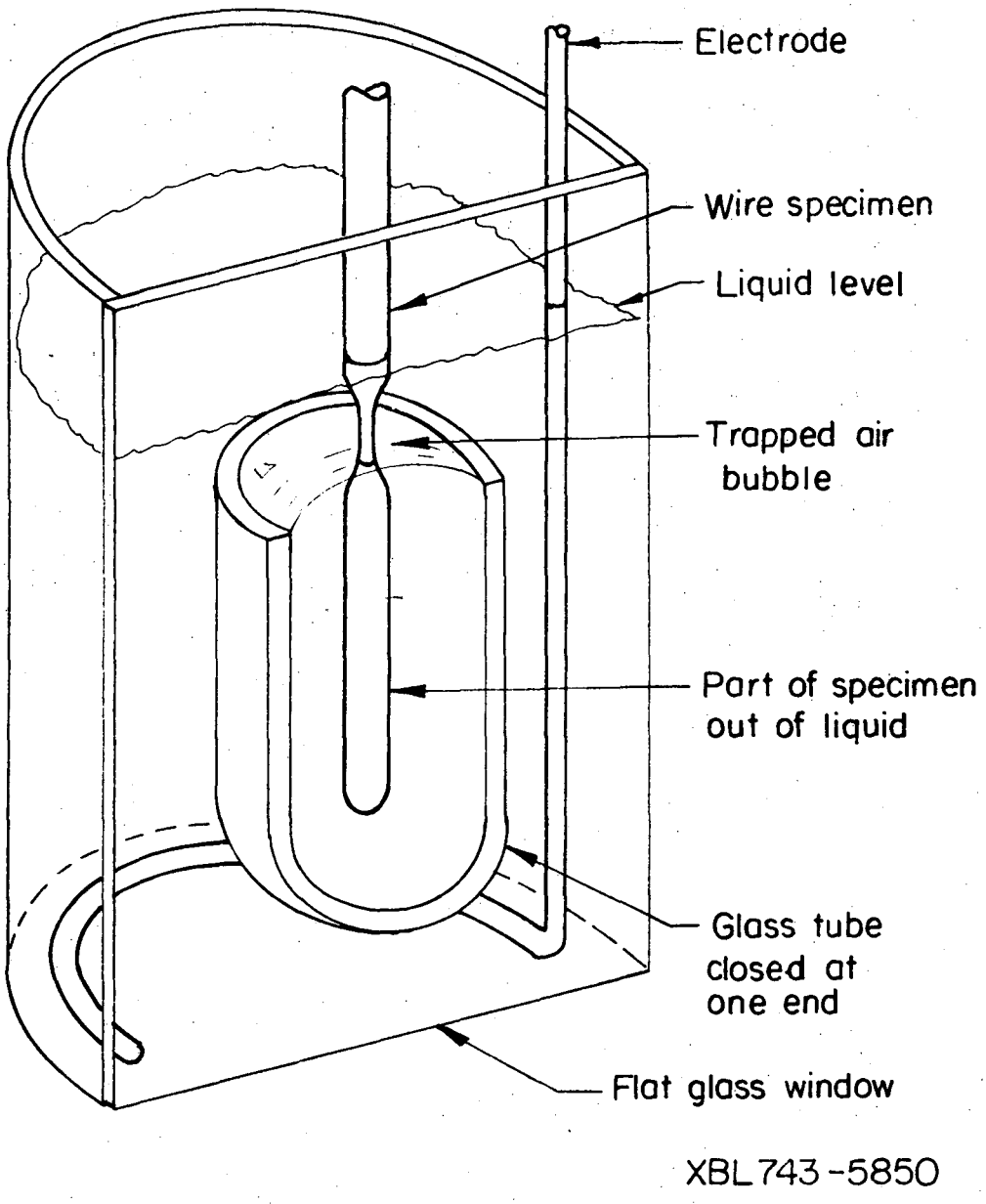
Electrode
Wire specimen
Liquid level
Trapped air bubble
Part of specimen out of liquid
Glass tube closed at one end
Flat glass window
XBL743-5850

Fig. 50.

TECHNICAL INFORMATION DIVISION
LAWRENCE BERKELEY LABORATORY
UNIVERSITY OF CALIFORNIA
BERKELEY, CALIFORNIA 94720